First Year Report: Modelling Clouds in the Infrared

Jane Hurley

August 25, 2006

Contents

List of Figures

List of Tables

Chapter 1

Motivation

From a human perspective, the influence of clouds on human life is pervasive. They are a source of inspiration, giving us beautiful sunrises and sunsets, terrific shows of lightning and rain, and of comfort, providing cooling shade on a hot day and life-sustaining water. They are also the sources or symptoms of nearly all hazardous weather – tornadoes, lightning, hail, heavy rains, damaging winds, freezing rain, blizzards and dense fogs. In recent times, clouds have become a source of interest since they have been increasingly recognized for their influence on the radiative balance of the Earth and the implications that they have on possible climate change, as well as in other unpleasant phenomena such as air pollution and acid-rain production.

The impact of clouds on the atmosphere is obvious. Latent heat is released upon their formation and absorbed when they evaporate away. Vertical transport of energy in the atmosphere is affected by the circulation systems associated with clouds. The surface and planetary radiation balances are modified by cloud scattering, absorption and emission of solar and infrared radiation and these factors introduce key feedbacks that influence climate sensitivity. Furthermore, some clouds act to warm the planet while others act to cool it. Clouds with low tops tend to cool the planet because they increase the overall reflectivity without decreasing substantially the amount of infrared radiation emitted to space. Conversely, cloud with high tops tend to warm the Earth because they are typically thinner and less reflective, but much cooler and thus re-emit much less absorbed infrared energy back out to space. The net effect of clouds, then, is due to the relation of cloud types and their frequency of occurrence. Satellite measurements indicate that clouds over the whole Earth on average have a cooling effect of about 17 W/m^2, which corresponds to several times the radiative forcing that would occur if carbon dioxide were doubled. Thus, how cloud radiative forcing responds to changing climate is one of the great unsolved puzzles of climatology and one that must be solved before reliable long-range predictions can be made.

Cirrus clouds are frequently observed at all latitudes and, at any one time, 60% of the Earth's surface is covered by cirrus. Cirrus clouds are interesting because they are high enough to act to warm the Earth; however this mechanism is not well understood in terms of the relation of micro- and macro-physical properties. Because they are so wide-spread and permanent, in the realm of global warming and climate sensitivity it is important to

understand how these clouds affect the climate. This can be achieved by relating the retrieved cloud parameters to global distributions, occurrences and radiative properties.

There have been many studies on clouds over the years and many climatologies of clouds in general and cirrus in particular; however few have dealt with cirrus cloud coverage. In 1957, London compiled the first extensive cloud climatology to include cirrus by assembling a large number of surface cloud observations of the Northern Hemisphere from the 1930's and 1940's. More recently, climatologies were compiled by Barton (1983), Warren (1985), Woodbury and McCormick (1986), Prabhakara et al (1988), Wylie and Menzel (1989), Wylie et al (1993) but these were all limited by a lack of global coverage. Currently, the Stratospheric Aerosol and Gas Experiment (SAGE), High Resolution Infrared Radiation Sounder (HIRS) instrument, International Satellite Cloud Climatology Project (ISCCP) and GRAPE project are actively compiling cloud climatologies. SAGE uses a slope or slope-intercept method which works by comparing the extinction measured by two out of the three available channels. HIRS uses a technique called "CO_2" slicing which takes advantage of a partial CO_2 absorption from $13-15$ microns, providing a means of detecting semi-transparent clouds. ISCCP applies space- and time-contrast tests, which use the infrared channel to pick out the maximum temperature registered in a pixel and threshold it in comparison with a local mean temperature.

The aim of this work is to accurately and reliably retrieve cloud parameters from MIPAS spectra to produce a cirrus climatology which includes global cirrus frequency of occurrence, cloud cover, parameter distribution, and radiative properties.

Chapter 2

Clouds: Microphysics, Macrophysics and Influence

A cloud, as defined by the World Meteorological Organization in 1975, is a visible aggregate of minute suspended particles of water or ice (a "hydrometeor") in the Atmosphere above the Earth's surface. (WMO, 1975)

2.1 Formation

Clouds form when the content of water vapour found locally in a region of the atmosphere exceeds the capacity of the air in that region to hold moisture. When this occurs, the water vapour condenses to form either water droplets or ice crystals, which are basic cloud particles. Logically then, cloud-causing processes are those which either increase the water-vapour content of the atmosphere or that decrease the air's capability to hold water-vapour. Since the capacity of air to hold water-vapour is highly temperature dependent (capacity roughly doubles for a 10°C increase in temperature), processes that cool the air dominate the production of clouds. Ascent (expansion of air at decreasing pressures), radiative cooling (by emission of infrared radiation), and conduction (warm air overlies a cold surface) are dominant cooling processes, and of these, ascent is the most prevalent, to the extent that formation of clouds can be unambigiously described as a result of cooling of air below its condensation or deposition point as it rises upwards in the atmosphere. (Ewen, 2005)

In addition to cooling processes, cloud condensation nuclei (CCN) are usually required for cloud formation, and in any case, expedite the formation process — in fact, without CCN, water vapour could be supercooled as low as −40°C before condensing. Cloud condensation nuclei are submicron to micron sized particles upon which the processes of condensation and deposition occur. There are many different types of CCN, ranging from ocean salts to combustion products; however the most effective CCN are those which are hygroscopic (water-absorbing), and these are quite concentrated in the Earth's atmosphere, with 100 to 1000 per cubic centimetre. CCN allow condensation of water vapour to start at relative humidities as low as 75%, forming haze droplets which are defined by the American Meteorological Society as small unactivated liquid droplets of sub-micron diameter. Cooling

processes then increase the relative humidity and the haze droplets grow. Once a haze droplet has reached a certain critical size (critical supersaturation) it becomes a cloud droplet. A cloud droplet is a spherical particle of liquid water with a diameter of 1 - 50 μm, which has been activated by condensing on a cloud condensation nucleus.

Ice clouds form in much the same way as described above for water clouds, but in a slightly different manner. Ice particles form in the atmosphere through glaciation (when water vapour sublimes or water droplets freeze).

Taking cirrus clouds as an example, at cirrus temperatures ($-30°$C – $-80°$C) nucleation of ice particles can occur in two ways:

- **Homogeneous Nucleation**: The spontaneous freezing of pure water or spontaneous ice-embryo formation within soluble aerosol particles in various states of dilution.
- **Heterogeneous Nucleation**: A supercooled liquid freezes around an ice nucleus (IN) or vapour is deposited on a deposition nucleus.

Heterogeneous nucleation allows ice nucleation to initiate at warmer temperatures and lower relative humidities than is possible by homogeneous nucleation, in the same manner as CCN's accelerate and expediate the formation of water droplets. IN's differ from CCN's in the sense that they are far less abundant (10^{-3} per cm^3), and are frequently clay particles such as kaolinite. Because of the extremely low concentration of the IN in the atmosphere, homogeneous nucleation is the dominant mechanism of ice formation (Heymsfield and Miloshevich 1993), but it has recently been reported that heterogeneous nucleation is more important in polluted areas (such as the Northern Hemisphere as opposed to the Southern Hemisphere).

2.2 Classification

It is logical that different initial conditions and formation processes will cause different types of clouds to form. However, from a purely observational perpsective, it is quite difficult to objectively classify clouds due to the large range of shapes and sizes that occur. This task was first undertaken in 1803 by the English pharmacist Luke Howard, who noted that there were three basic cloud types: "cirrus" (high, thin and wispy ice clouds), "stratus" (laminar layer-like low clouds) and "cumulus" (puffy, piled clouds). He also termed precipitating clouds "nimbus". By 1880, the classification system still accepted for use today had evolved to include ten cloud types: cirrus, cirrostratus, cirrocumulus, altostratus, altocumulus, nimbostratus, stratocumulus, stratus, cumulus and cumulonimbus. These ten cloud types are conventionally grouped into three cloud-base height regimes in the troposphere (high-, mid-, and low-level). Table 1.1 summarizes the characteristics of the cloud types and Fig. 2.1 pictorially represents the cloud types.

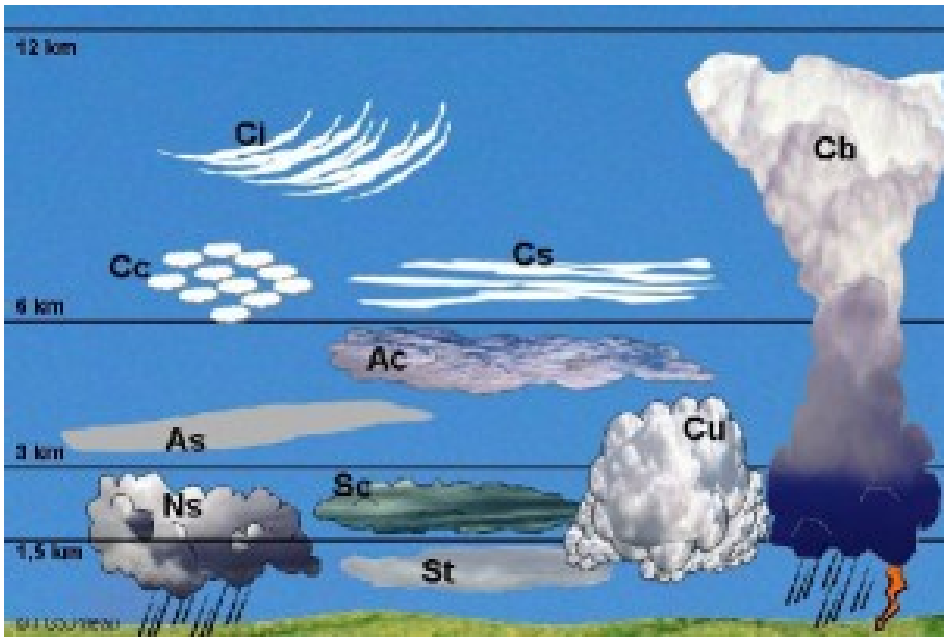

Figure 2.1: Schematic representation of the ten cloud types. (Gordeau, 2004)

Height Group	*Cloud Type*	*Base Height [km]*	*Base Temperature [C]*	*Cloud Depth [km]*	*Optical Thickness [km^{-1}]*	*Particle Phase*
High	Cirrus (Ci)	5-15	-70:-30	0.5-2	< 3.6	ice
	Cirrostratus (Cs)	5-15	-40:-25	1-2	3.6-23	ice
	Cirrocumulus (Cc)	5-12	-40:-25	0.1-0.3	–	liquid or mixed
Mid	Altostratus (As)	3-8	-30:-10	1-3	3.6-23	ice or mixed
	Altocumulus (Ac)	2-8	-30:10	0.1-1	< 3.6	liquid or mixed
	Nimbostratus (Ns)	0.5-2	-10:20	2-10	23-379	ice or mixed
Low	Cumulonimbus (Cb)	1-4	-5:25	2-20	–	mixed
	Cumulus (Cu)	1-4	-5:25	0.5-4	< 3.6	liquid
	Stratocumulus (Sc)	0-2	-10:20	0.1-2	3.6-23	liquid or mixed
	Stratus (St)	0-2	-10:20	0.1-0.5	23-379	liquid

Table 2.1: Characteristics of the ten cloud types.

Property	*Value*
Size	range $1 - 8000\mu$m mean $250\mu m$
Shape	non-spherical: hexagonal columns or plates, aggregates of columns or bullets
IWC	range $10^{-4} - 1.2$ g/m^3 mean 0.025 g/m^3

Table 2.2: Microphysical properties of cirrus, as reported by Lynch, (1996).

As previously noted, the macrophysical properties that we observe easily (as well as the microphysical properties that we can measure with some difficulty) are a result of the formation process through which a cloud is produced. For instance, cirrus is typically formed by advancing warm fronts or by mechanical lifting, although it can also be a result of anthropogenic activities such as contrail formation from the rapid cooling of jet engine exhaust. Cirrostratus is a result of large-scale lifting, while cirrocumulus is formed when there is large-scale lifting in a weakly stable formation layer. The convective clouds, cumulonimbus and cumulus, form when the atmosphere is conditionally stable – that is, when the atmospheric temperature decreases sufficiently rapidly with altitude that an air parcel that is saturated with water is warmer than its environment and therefore rises. They thus form on the windward side of mountains and in regions of low-level convergence. Altostratus, nimbostratus, stratocumulus and stratus are formed when the atmosphere is not conditionally stable and thus are frequently formed over cool surfaces.

2.3 Microphysics

Microphysical properties refer to the size and shape of particles and to their volume distribution. Often volume distribution is expressed as ice water content (IWC), which is defined as the mass of ice per unit volume. Volume distribution can also be described by number density, n, which is equivalent to the number of particles per unit volume. The optical depth, albedo, emissivity, and transmissivity of clouds are determined partly by the microphysical properties of the cloud.

Most of our knowledge of the microphysical properties of clouds come from in-situ measurements, predominantly by aircraft-mounted instruments. Again take cirrus as a typical example. Measurement campaigns include Weickmann (1947) over Germany, FIRE I and II over Wisonsin and Kansas (1992), SUCCESS over Oklahoma and Kansas (1996), CEPEX (1997), EUCREX over the Atlantic Ocean and mid-latitudes in Europe (2000), and CRYSTAL-FACE over Florida (2002). From these campaigns, the accepted microphysical properties of cirrus are given in Table 1.2.

Growth of a crystal begins with diffusion and deposition in a supersaturated and super-

cooled environment. Dependent upon the location of the crystal with respect to the edge of the cloud and the intervening optical thickness, a generalized growth equation is

$$\frac{dm}{dt} = 4\pi CD(\rho_s - \rho_e) \tag{2.1}$$

for particle mass m, environment diffusivity D, vapour concentration at equilibrium with the crystal surface ρ_s, vapour concentration at equilibrium with the environment ρ_e, and shape and size parameter C (for sphere, $C = radius$). Further growth can occur by accretion or aggregation. Accretion is the capture of supercooled droplets by an ice phase precipitation particle and aggregation is when ice particles stick together as they grow and collide (Rodgers and Yau, 1989).

2.3.1 Shapes and Sizes

The size and shape of a cloud particle is referred to as the particle habit. Usually, cirrus clouds are composed of several different particle habits and frequently the distribution of particle habits is dependent upon the vertical height within the cloud (as shown in Fig. 2.2 and Fig. 2.3). As well, particle habit is dependent upon formation mechanism and temperature, which usually are the result of the geographic location. It is important to determine the shape and size distribution of particle habits because it has been shown that small crystals are responsible for most of the visible reflection and infrared absorption associated with clouds.

2.3.2 Ice Water Content

IWC is measured by :

- Direct measurement of the amount of water in solid form (hygrometer separates ice particles from water vapour and heats within an inlet).
- Integrating the measured size distribution.

Obviously, the IWC is dependent upon the particle habit.

2.4 Global Influence

Although only a mere 0.0012% of the total water on Earth is in the atmosphere, mostly as water vapour, 90% of this water resides in the bottom 5 km of the atmosphere. In fact, the relative volume of the water vapour can reach 4% in warm, humid air like that near the tropics. This global distribution of water vapour and conditions that spark cloud formation implies the global ramifications of cloud production. In fact, the average cloud cover for the

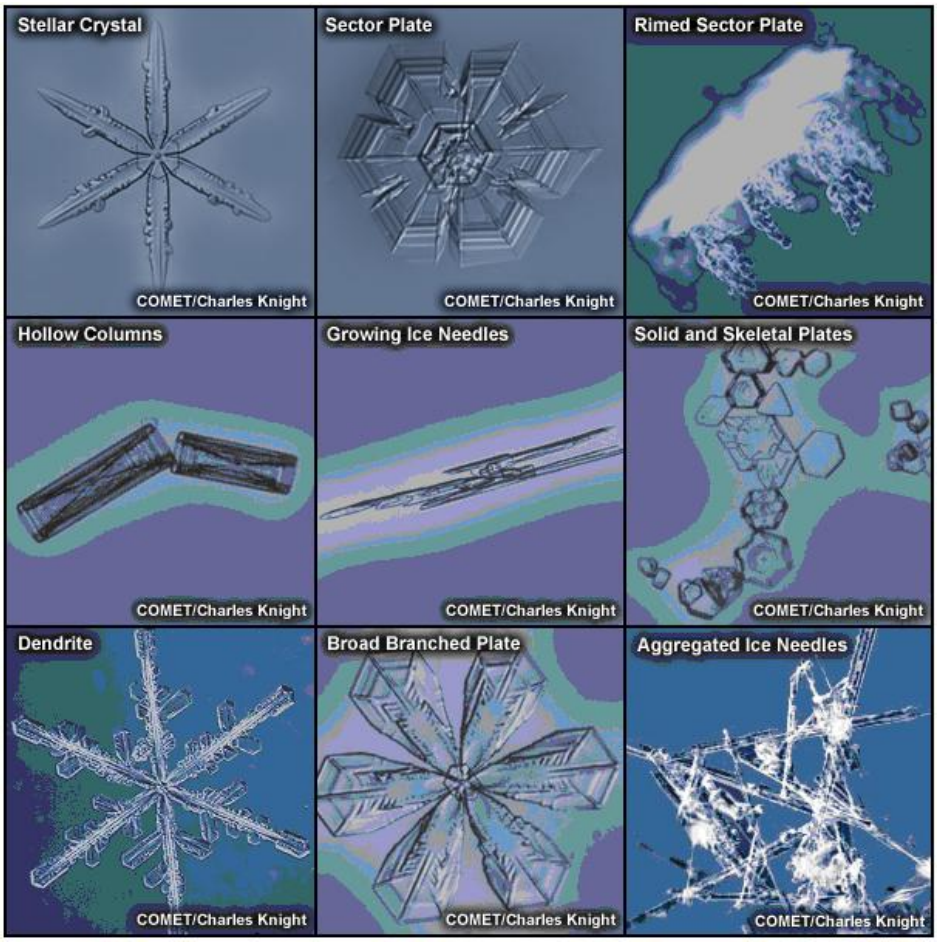

Figure 2.2: Particle habits associated with cirrus clouds.(MetEd, 2005)

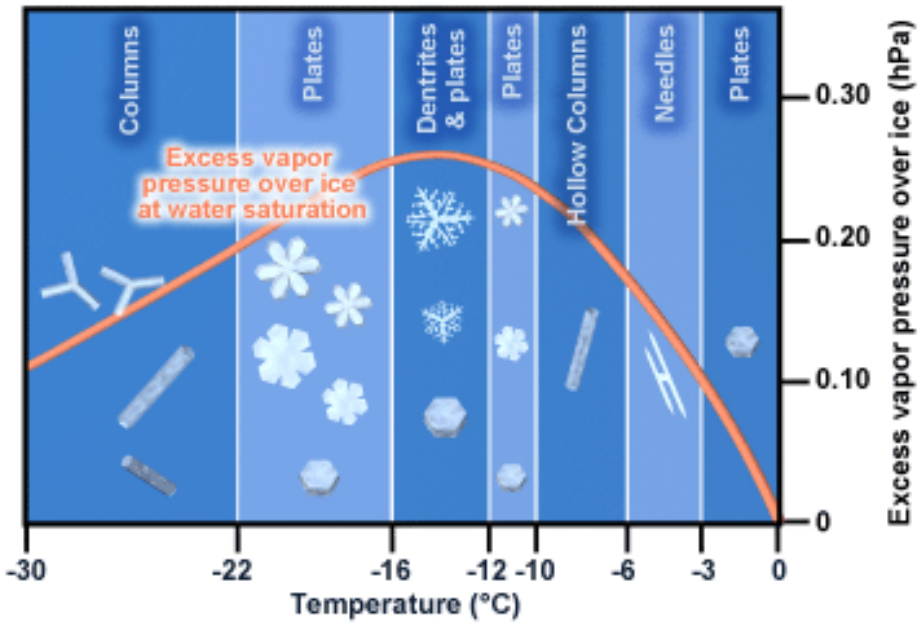

Figure 2.3: Dependence of particle habit upon temperature, and hence upon geography and location within the cloud. (MetEd, 2005)

entire Earth is about 61%, with a slightly greater cloud cover over the Southern Hemisphere than in the Northern Hemisphere, and over oceans as opposed to land masses.

The International Satellite Cloud Climatology Project (ISCCP) was established in 1982 as part of the World Climate Research Programme (WCRP) to collect and analyze satellite radiance measurements to infer properties, distributions and variations of clouds. Data collection began on 1 July 1983 and is currently planned to continue through to 30 June 2010. The resulting datasets and analysis products are used to improve understanding and modelling of the role of clouds in climate. Fig. 2.4 shows a map of percent cloud cover averaged over the period of 1 July 1982 to 2001 from ISCCP data.

Clouds and the processes affecting them influence components of Earth's system in a variety of ways. They affect the atmosphere, hydrosphere, biosphere, and geosphere through a plethora of different mechanisms, while having a very direct impact on the heat and moisture budget of the Earth as well as on trace gases and aerosols present. Clouds and climate are intimately related, each affecting the other in a complicated feedback system which is not well understood.

Clouds influence the climate in three ways:

- **Precipitation**: Clouds may precipitate liquid water and ice water, which are the principal forms of water transport to land surfaces.
- **Release and Transport of Heat/Moisture**: Without clouds, the atmospheric tem-

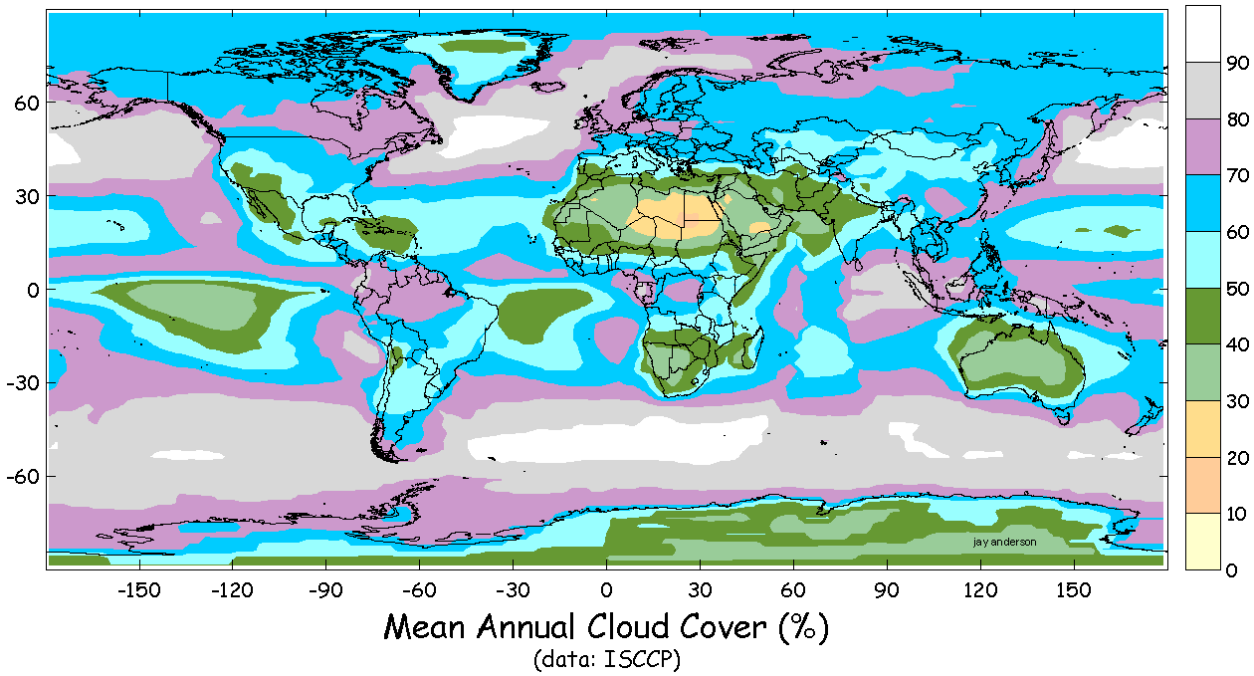

Figure 2.4: Global distribution of mean cloud cover (courtesy of Jay Anderson) constructed using ISCCP data from 1 July 1982 through 2001. The data has been analysed on a 2.5° latitude-longitude grid.

perature profile in the troposphere would, in most places, decrease at the dry adiabatic lapse rate of 9.8°C/km. However, with clouds, the temperature decreases more slowly with height due to the release of latent heat of condensation when rising parcels of water-vapour laden air condense to form clouds. The clouds essentially maintain the temperature lapse rate near the moist adiabatic lapse rate, which implies that the surface is thermally coupled with the troposphere in the sense that both respond together to external radiative forcing. So, processes that warm the troposphere will warm the surface while cooling processes will act to cool both the troposphere and surface – the troposphere and surface respond together to processes which influence the energy balance at the top of the troposphere. Concurrently with the condensation of the water vapour to form clouds, heat and moisture from the surface are transported upwards because the ascending cloud cores are usually warmer than the drier air outside of the cloud.

- **Planetary Radiation Budget**: Clouds scatter/reflect incident solar radiation and absorb/emit infrared radiation back toward space and toward the Earth's surface. Reflection of solar radiation has a net cooling effect since less radiation reaches the Earth's surface, while absorption of infrared radiation has a net warming effect since the radiation cannot escape to space. It is accepted that the net effect of clouds is to cool the planet, because the cloud field is generally more efficient at reflecting solar radiation than it is at trapping infrared (thermal) radiation. The Earth Radiation

Budget Experiment (ERBE) shows that, averaged over the planet, -47 W/m^2 are reflected back to space by clouds, whereas 30 W/m^2 of thermal radiation is trapped by the clouds, resulting in a net loss of 17 W/m^2. This net cooling of the atmosphere implies that if the negative cloud forcing were not present, the surface temperature would be $10-15$°C higher.

Cloud Radiative Forcing (CRF) measures the impact of clouds on the planetary radiation budget in terms of the difference between the net downward radiative flux with clouds and that without clouds, such that

$$CRF = R - R_{clear}. \tag{2.2}$$

Furthermore, because of the different reaction of clouds to different types of radiation, it is useful to study the CRF in two wavelength ranges: shortwave (solar) radiation with wavelengths between 0.2 μm and 4 μm , and longwave (infrared) radiation with wavelengths between 4 μm and 100 μm. The solar CRF (SCRF) is almost universally negative, since the reflective properites of clouds tend to reflect a high proportion of incident solar radiation back outwards to space. Conversely, the infrared CRF (ICRF) is almost always positive since clouds tend to insulate the Earth from losing heat. However, each cloud is unique, with radiative properties that are determined by its distinct combination of micro- and macro-physical properties, as well as the geographic region in which it is located. Thus, the total CRF is the sum of SCRF and ICRF, so that the total CRF can be negative or positive depending upon the relative strengths of the solar and infrared CRFs. Fig. 2.5 shows the global distribution of the two contributions to CRF (DelGenio, 2003).

The SCRF is defined as

$$f_c \mu S[r_s - r_c - \frac{t_c r_s t_c}{1 - r_s r_c}], \tag{2.3}$$

where f_c is the fractional cloud cover, μ is the cosine of the solar zenith angle, S is the solar constant, r_s is the surface reflectivity/albedo, r_c is the cloud reflectivity/albedo, and t_c is the cloud transmissivity. Thus, the first bracketed term corresponds to the scattering of sunlight to space by the clear sky and the Earth's surface while the second bracketed term represents the reflection by the cloud. The third and final bracketed term denotes the transmission through the cloud, multiple reflections between the surface and the cloud, and transmission back through the cloud. The global mean SCRF is -50 W/m^2, but ranges from -140 W/m^2 to 30 W/m^2. Although the net global SCRF is negative, there are localized geographical areas which are characterized by positive SCRF, namely those having high surface albedo, such as over deserts or ice fields.

The ICRF is defined as

$$f_c[\epsilon \sigma T_c^4 - a \sigma T_s^4], \tag{2.4}$$

where ϵ is the cloud emissivity, a is the cloud absorptivity, σ is the Stefan-Boltzmann constant, T_c is the cloud temperature and T_s is the surface temperature. The first term denotes the emission of infrared radiation by the cloud while the second term represents the absorption of infrared radiation by the cloud. However, at infrared wavelengths, $\epsilon \approx a$, and so the

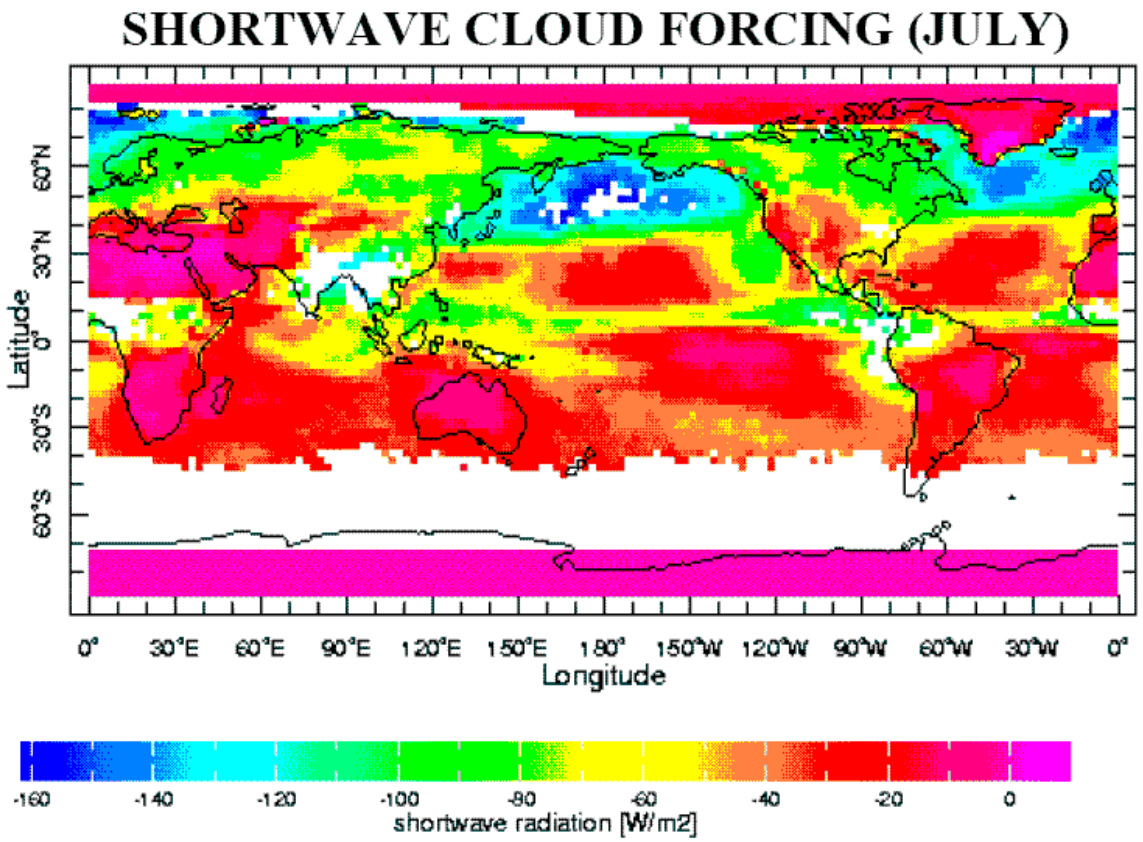

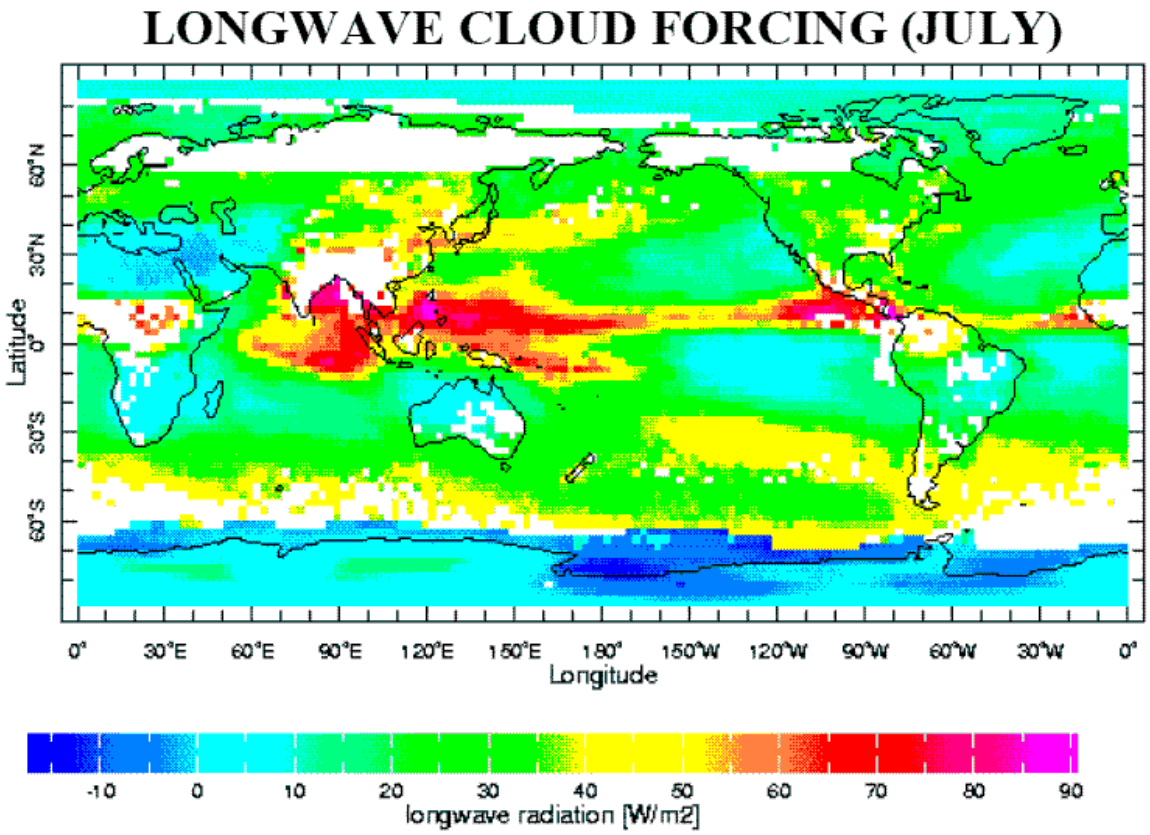

Figure 2.5: Global distribution of SCRF and ICRF. (DelGenio, 2003)

Height	*Cloud Type*	*Net Radiative Effect*	*Reasoning*
High	Cirrus (Ci)	*warming*	little reflection because of thinness $T_c << T_s$ since quite high
	Cirrostratus (Cs)	*warming*	low reflection
	Cirrocumulus (Cc)	-	-
Mid	Altostratus (As)	strong ICRF *cooling*	$T_c < T_s$ since fairly high
	Altocumulus (Ac)	emits much infrared, reflects much solar *marginally cooling*	high reflectivity $T_c < T_s$ since higher
	Nimbostratus (Ns)	emits much infrared, reflects much solar *marginal, depends on cloud*	high reflectivity $T_c < T_s$ since higher
Low	Cumulonimbus (Cb)	*marginally cooling*	high reflectivity $T_c < T_s$
	Cumulus (Cu)	emits less infrared, reflects more solar *cooling*	high reflectivity $T_c < T_s$ since higher
	Stratocumulus (Sc)	*marginally cooling*	high reflectivity $T_c \approx T_s$ since near surface
	Stratus (St)	*little effect*	$T_c \approx T_s$ since near surface

Table 2.3: General radiative properties of the ten cloud types.

ICRF truly depends more upon the fraction of cloud cover and the temperature difference between the cloud and the surface. Since clouds are almost universally colder than the surface below them, the ICRF is nearly always positive, having a global mean of 30 W/m^2 and ranging from 0 W/m^2 to 100 W/m^2.

Each cloud has its own radiative fingerprint, but a few generalizations can be made about which act to cool or warm the planet. For example, clouds that form during the day are more likely to cool, while clouds that form at night or in the dark of winter will warm. Marine boundary layer clouds usually cool. Clouds that form in a warmer climate generally are higher, brighter and better emitters and have a warming effect. Generalizations about the dominant radiative properties of the different cloud types are summarised in Table 2.3, and an example analysis (Krueger, 2005) of the CRF of real cloud measurements is given in Fig. 2.6.

A combination of micro- and macro-physical properties determines the radiative properties of clouds. On the macrophysical side, it is typically structural properties that are of interest, namely:

- **Cloud Height**: The cloud height determines the radiative temperature of the cloud, which affects the radiative capacity of the cloud as a blackbody-like entity.
- **Latitude**: Cloud height, insolation, solar input and surface temperature are all functions of latitude.

Cloud type	Surface			TOA			Atmosphere		
	SW	LW	TL	SW	LW	TL	SW	LW	TL
Cirrus	−3.6	1.1	−2.5	−4.2	5.5	1.3	−0.6	4.4	3.8
Cirrostratus	−7.2	1.7	−5.5	−7.9	5.5	−2.4	−0.7	3.8	3.1
Deep convective	−5.8	0.7	−5.1	−6.2	2.9	−3.3	−0.4	2.2	1.8
Altocumulus	−3.1	2.2	−0.9	−3.2	1.5	−1.7	−0.1	−0.7	−0.8
Altostratus	−8.2	3.6	−4.6	−8.3	2.0	−6.3	−0.1	−1.6	−1.7
Nimbostratus	−3.4	1.3	−2.1	−3.4	0.7	−2.7	0.0	−0.6	−0.6
Cumulus	−5.5	5.3	−0.2	−5.2	0.6	−4.6	0.3	−4.7	−4.4
Stratocumulus	−13.2	7.3	−5.9	−12.7	1.2	−11.5	0.5	−6.1	−5.6
Stratus	−2.6	1.2	−1.4	−2.4	0.2	−2.2	0.2	−1.0	−0.8
Sum (true)	−52.6	24.4	−28.2	−53.5	20.1	−33.4	−0.9	−4.3	−5.2

Figure 2.6: Global annual mean full sky cloud-induced radiative flux in W/m^2 at the surface, the top of the atmosphere (TOA) and in-atmosphere. The names of the three most abundant cloud types are shown in bold. (Krueger, 2005)

Microphysically, the radiative properties depend upon the optical properties of the cloud, which in turn are determined by

- Particle Composition
- Shape
- Size
- Number Density

The optical properties of interest are scattering, reflection and absorption at solar and infrared wavelengths. Reflection is proportional to the liquid water content of the cloud (which is dependent upon cloud depth (proportional), entrainment (inversely proportional) and precipitation (inversely proportional)) and inversely proportional to the droplet size. The overall ability of a cloud to reflect solar radiation is described by the cloud optical thickness.

Cloud microphysics are also closely related to CCN composition, concentration and distribution, since not only do the CCN have their own associated optical properties, but the particular CCN used in the formation of a cloud will affect the type of cloud produced. Hence reflection is also dependent upon the CCN used and thus upon aerosol concentrations and distributions.

It should be quite obvious that many parameters determine the radiative properties of a cloud, and hence its net radiative effect. In order to be confidently able to predict the net radiative effect of a single cloud, and indeed of global cloud distributions, it is necessary to have a firm grasp on the effect of these properties and to be able reliably to retrieve these parameters somehow. A complicating issue, however, is that the climatic conditions present at the formation and during the evolution of each cloud are dependent upon multiple factors, including the radiative properties of the self-same clouds.

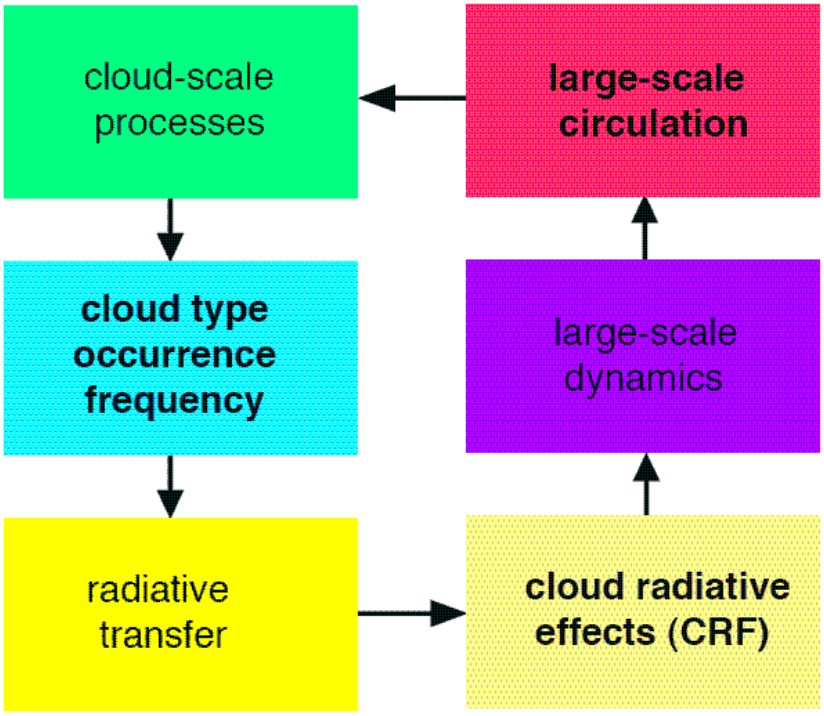

Figure 2.7: Schematic of cloud-climate interaction. (Krueger, 2005)

So, it is obvious that climate, in turn, influences clouds by producing conditions which affect the type of clouds that form, their composition and distribution, and their radiative and hydrological properties. Clearly, then, as highlighted in Fig. 2.7, climate and clouds are linked together in a complicated interaction of mutual influence and feedback.

As the radiative properties of clouds are affected by climate, and climate is affected by the radiative properties of clouds, the cloud-climate feedback influences the sensitivity of the climate system to external forcing, such as anthropogenic emissions or varying solar output. Denoting the external forcing as ΔR_{ext} and the response of the surface temperature as ΔT, define the sensitivity of the surface temperature to external forcing as

$$\lambda = \frac{\Delta T}{\Delta R_{ext}}. \tag{2.5}$$

If climatic equilibrium is assumed, the planetary response to the forcing (ΔR) exactly opposes the surface temperature response to the external forcing – that is,

$$\Delta R = -\Delta R_{ext}. \tag{2.6}$$

The sensitivity parameter can then be defined as

$$\lambda = -\frac{\Delta T}{\Delta R}. \tag{2.7}$$

Expressing

$$\Delta R = \Delta R_{clear} + \Delta CRF \tag{2.8}$$

and

$$\lambda_{clear} = -\frac{\Delta T}{\Delta R_{clear}}, \tag{2.9}$$

the climate sensitivity can be expressed as

$$\lambda = \frac{\lambda_{clear}}{1 - \lambda_{clear}\frac{\Delta CRF}{\Delta T}}. \tag{2.10}$$

The term $\lambda_{clear}\frac{\Delta CRF}{\Delta T}$ is called the cloud-climate feedback. It can be either positive or negative, depending upon if the CRF increases or decreases with surface temperature – a positive cloud-climate feedback increases the climate sensitivity above that of the clear-sky, while a negative feedback decreases the sensitivity to below that of the clear-sky. If the cloud-climate feedback is greater than unity, the planetary radiation balance cannot establish an equilibrium and the cloud-climate system is unstable. The clear-sky climate sensitivity is estimated to be about $0.5°\mathrm{C/Wm}^2$, but it is uncertain even as to the sign of the cloud-climate feedback. This uncertainty is a result of lack of knowledge about cloud distribution and the radiative properties of clouds. (Albrecht, 1992)

Chapter 3

MIPAS: Candidate Instrument for Cloud Studies

The Michelson Interferometer for Passive Atmospheric Sounding (MIPAS) was launched in March 2002 on the European Space Agency's Environmental Satellite (ENVISAT). The ENVISAT spacecraft is in an 800 km sun-synchronous polar orbit, with a nominal orbit having a repeat period of 35 days, an orbital period of 100.6 minutes and an inclination of 98.54°. The inclination of the orbit enables full global coverage pole-to-pole. (ESA, 2005)

In the nominal mode, MIPAS can either look in the anti-flight direction or perpendicular to the flight track, as shown in Fig. 3.1. It nominally measures at 17 altitude sweeps in a single profiling scan (6 km, 9 km, 12 km, ..., 36 km, 39 km, 42 km, 47 km, 52 km, 60 km, 68 km), taking 4.5 s at each sweep to acquire the measured spectrum. A complete scanning profile, then, takes about 80 s, resulting in over 1000 scans taken daily. There is nominally 330 km horizontally between the first (highest) and last (lowest) sweeps in a scan and the along-track distance between two measurements at the same altitude is about 500 km. The field-of-view is about 3 km vertically and 30 km horizontally.

If the Earth is viewed side-on, the atmosphere appears as a halo around it – this halo is known as the limb. MIPAS is an infrared limb sounding instrument which uses limb emission to measure (operating both day and night) high resolution (0.025 cm^{-1}) spectra in the near - to - mid - infrared from 685 cm^{-1} to 2410 cm^{-1} in five discrete bands, as described in Table 3.1.

Band	*Wavenumber Range* (cm^{-1})
A	$685 - 970$
AB	$1020 - 1170$
B	$1215 - 1500$
C	$1570 - 1750$
D	$1820 - 2410$

Table 3.1: Bands measured by MIPAS FTS.

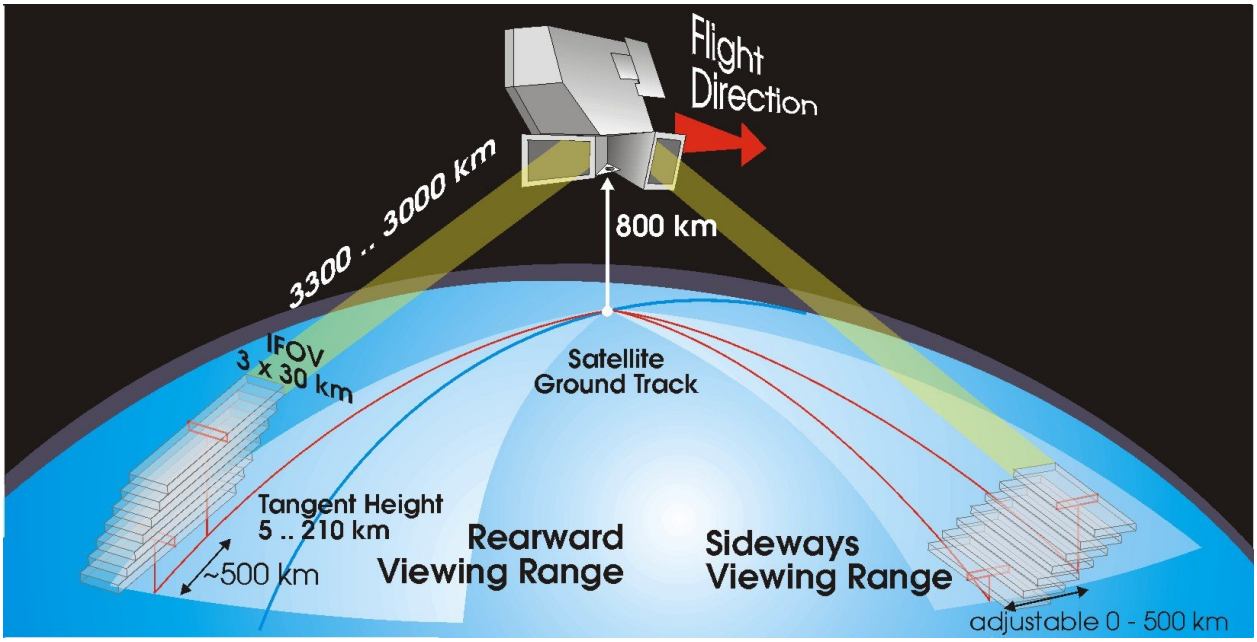

Figure 3.1: MIPAS viewing geometry. (ESA, 2005)

The limb emission technique consists of looking through the limb with cold space as a background and measuring the infrared radiation thermally emitted in the atmosphere along the line-of-sight, as shown in Fig. 3.2.

The limb radiometer receives radiation emitted by the atmosphere along a horizontal ray path which is identifiable by the tangent point, the point at which the limb ray path passes closest to the Earth's surface. Since the majority of the emission originates from the few kilometers of atmosphere immediately above the tangent point (because of the exponential decrease of density and pressure with height), the tangent height at the centre of the field-of-view is thought of as the altitude of the atmosphere nominally viewed by the limb sounder. Inherently, limb sounders have good vertical resolution. However, since the horizontal limb path is quite long, giving more substantial areas over which to sample trace gases, this long path gives a very poor horizontal resolution ($\approx$ 500km).

MIPAS is a Fourier Transform Spectrometer (FTS) designed for monitoring trace gases by measuring high resolution gas emission spectra of trace gases such as O_3, H_2O, HNO_3, CH_4 and N_2O. A Michelson interferometer, shown in Fig. 3.3, has a light source, a beamsplitter, two mirrors and a detector. A collimated beam from the light source is split in two by the beamsplitter (typically a half-silvered mirror inclined at 45° to the incident beam) and passed to the two mirrors which then reflect the split beams back along the same paths to the beamsplitter, where they interfere. If the optical path difference between the two beams is a multiple of the wavelength (i.e. $n\lambda$, $n\epsilon\mathbb{Z}$), there is constructive interference and a bright spot appears. Conversely, if the path difference is $\frac{2n+1}{2}\lambda$, $n\epsilon\mathbb{Z}$ the intereference is destructive

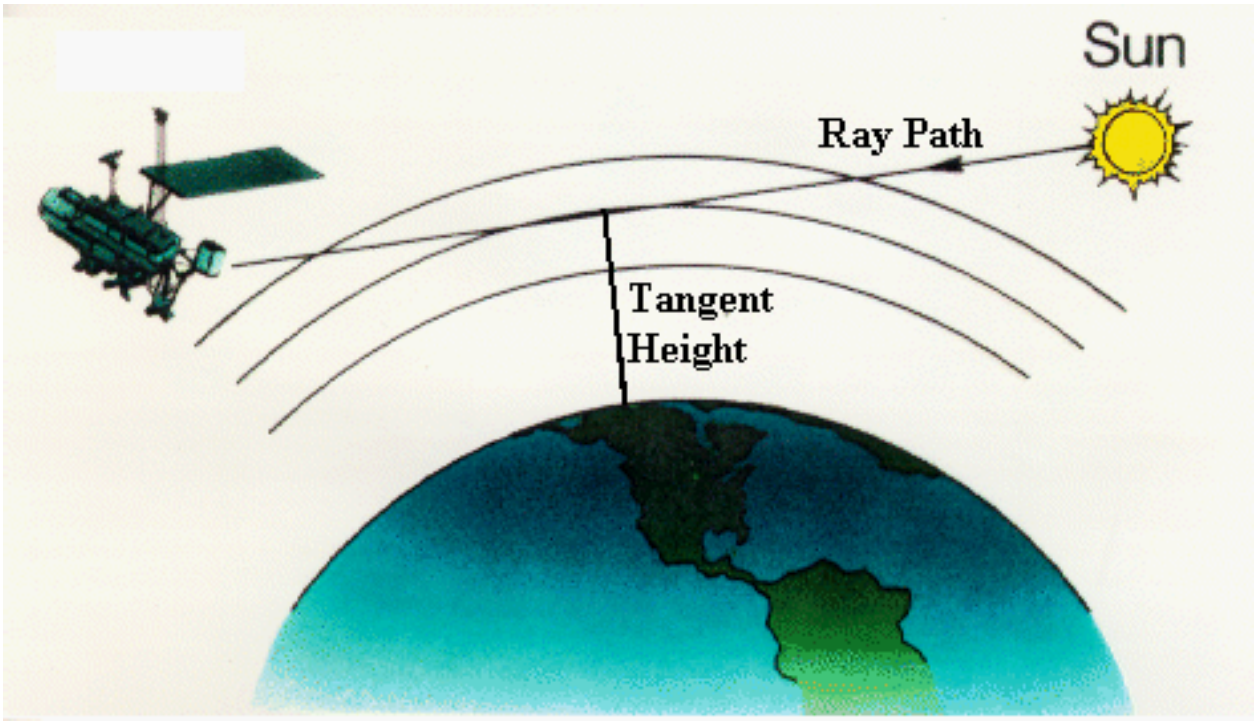

Figure 3.2: Satellite limb viewing geometry. (NASA, 2006)

and there is a dark spot instead.

In the FTS adaptation, one or both of the mirrors are movable, allowing the path difference to be altered. The movable mirror is scanned parallel to the light beam, causing the output to alternate between bright and dark fringes. A monochromatic light source causes the recorded signal to be modulated by a cosine wave. A non-monochromatic source will result in an output signal which is the Fourier transform of the spectrum of the input signal and is called the interferogram.

In MIPAS, radiation from the limb enters the instrument through the aperture in the front-end optics. The front-end optics have two scanning mirrors which are used to select the target line-of-sight. The elevation scan mirror points at various altitudes and corrects for variations in orbital altitude and in the geoid. The azimuth scan mirror is used to point at different angles to the side or rear of ENVISAT and also at the internal calibration blackbody. Next, the input radiation travels to the telescope and collimator, where first the telescope uses an internal field stop to select the instrument field-of-view (FOV), and then is collimated. The collimated beam of radiation then enters the interferometer. The interferometer has two retro-reflecting mirrors which move over a 100 nm path at a constant velocity of 0.25 mm/s. The output beams are then directed to a series of eight detectors which are cooled by a pair of synchronized Stirling-cycle coolers. The modulated output is then sampled at very frequent and regular optical path differences ($\approx$ 30 nm), and the detectors record the interferograms which will later be processed to obtain the limb spectral

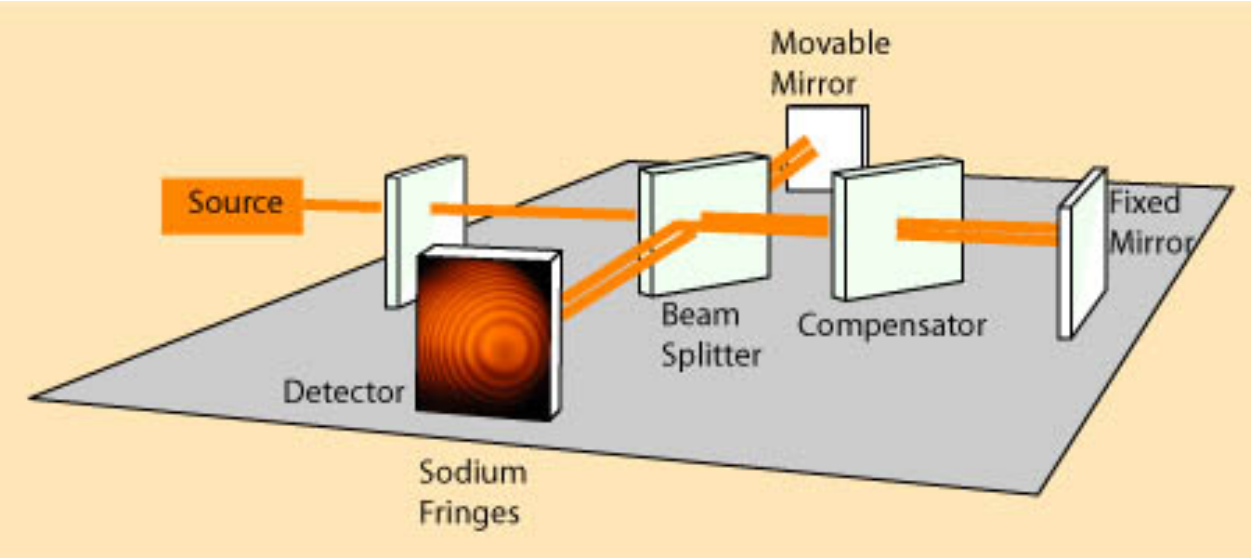

Figure 3.3: Three dimensional view of a standard Michelson Interferometer. (Hyperphysics, 2006)

radiance spectrum. Fig. 3.4 schematically represents the path and processes undertaken by a beam of light entering MIPAS.

Clouds, of course, are an issue for MIPAS. Clouds in the line-of-sight can act as grey-bodies with significant opacity which alter the measured radiation, and introduce serious problems in sensing atmospheric temperatures and gas profiles below the cloud level. Essentially, clouds introduce a multi-scattering effect which implies that the instrument measures radiance from below the tangent height. The presence of clouds (such as the bothersome cirrus) wreaks havoc with regular constituent retrievals by introducing a sharp transition from optically thin to optically thick limb transmittance at the cloud top which cannot be represented by the continuum retrieval. However, by studying these cloud-infected spectra, information about the cloud itself may be retrieved.

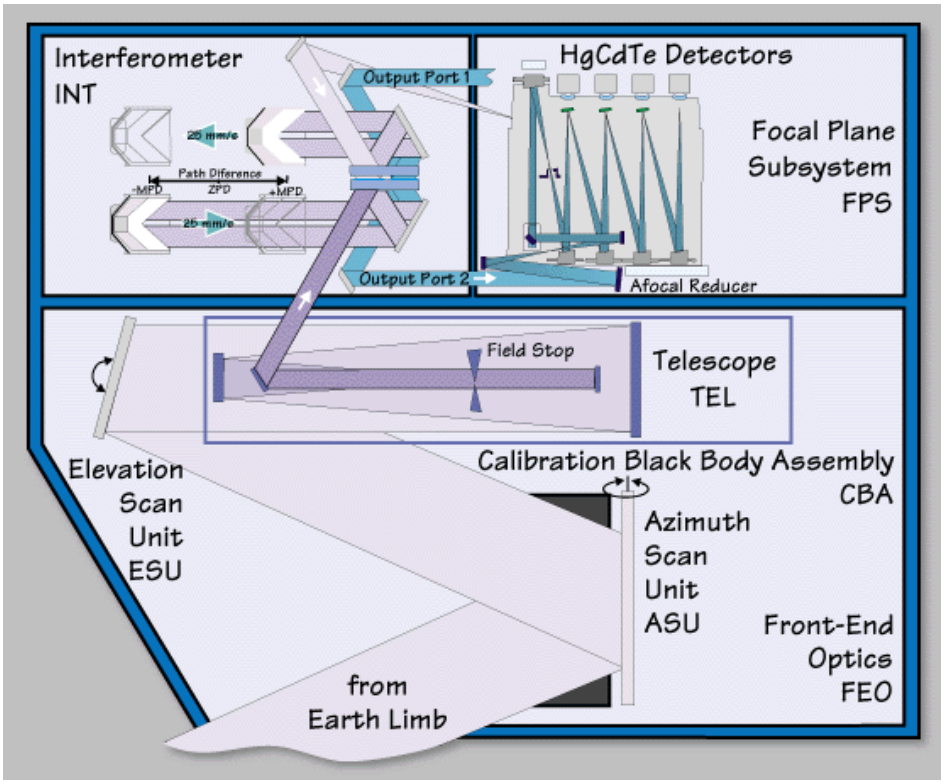

Figure 3.4: Schematic of path and processes undertaken by a beam of light in the measurement of spectra by MIPAS. (ESA, 2005)

Chapter 4

Detection and Retrieval of Clouds

The presence of cloud particles in the field-of-view of infrared remote sounding instruments influences observations and measurements registered, due to extraneous absorption, emission and scattering features in a large range of wavelengths. While typical retrievals of pressure, temperature and the like from high spectral resolution instruments can cope with small amounts of cloud by fitting a continuum term for each microwindow in parallel with the retrieval of the target species, it is nevertheless important to recognize and to be able reliably to identify the presence of clouds in such measurements before analysis is carried out upon such datasets. (Ewen, 2005; Spang, 2004)

4.1 Detection Methods

4.1.1 Instrument-Dependent Methods

There are a couple of common and simple techniques used to identify the presence of cloud in the field-of-view of a spectrometer working in the infrared such as the Michelson Interferometer for Passive Atmospheric Sounding (MIPAS), most of which involve thresholding of radiance values or of a ratio of radiance values. A selection of present day instruments detect cloud in the following manner:

- High Resolution Infrared Radiation Sounder (HIRS), involving a threshold on the partial CO_2 absorption at 13-15 μm.
- International Satellite Cloud Climatology Project (ISCCP), involving a thresholding of a local maximum temperature with comparison to a local mean temperature.
- Advanced Along Track Scanning Radiometer (AATSR), involving the difference between the temperature/shortwave reflectance between clouds and other surfaces.
- Scanning Imagin Absorption Spectrometer for Atmospheric Chartography (SCIAMACHY), involving thresholding of scene colour from polarisation measurement devices.
- Advanced Very High Resolution Radiometer (AVHRR), involving a fixed reflectance of brightness temperature threshold.

- Moderate-Resolution Imaging Spectrometer (MODIS), involving a threshold test on 13 separate spectral channels.
- Atmospheric Infrared Sounder (AIRS), involving a "cloud threshold" in brightness temperature.
- Halogen Occultation Experiment (HALOE), involving a thresholding of vertical extinction gradient.
- CloudSat, involving a threshold on transmission.
- Global Ozone Monitoring Experiment (GOME), involving polarisation measurement device identification by thresholding reflectance.
- Stratospheric Aerosol and Gas Experiment (SAGE), involving a comparison of extinction in different channels.
- Michelson Interferometer for Passive Atmospheric Sounding (MIPAS), involving ratio of radiances with Colour Indices.
- Cryogenic Infrared Spectrometers and Telescopes for the Atmosphere (CRISTA), involving ratio of radiances with Colour Indices.

4.1.2 Radiance Thresholding and Colour Indices

A very basic method is the Simple Radiance Threshold test which simply uses a statistically gathered threshold upon radiance to detect cloud by assuming that clouds have a warmer brightness temperature than a clear limb view. For MIPAS, in the region around 960.7 cm^{-1}, in order to detect a cloud having an extinction coefficient of 10^{-4}, a threshold of 100 $\mathrm{nW/cm^2\ sr\ cm^{-1}}$ must be chosen at a tangent height of 9 km (higher threshold for lower tangent heights and for higher extinction values).

A second generation detection method is Colour Index Thresholding, which improves consistent and reliable detection by reducing the influence of variations in pressure and temperature. Colour indices work on the principle of radiance ratios between two different regions (called microwindows, and denoted MW1 and MW2) of the spectrum which respond differently to cloud. The microwindows are chosen such that the first microwindow MW1 responds very little to the presence of clouds whereas the second microwindow MW2 shows a large reaction. (Spang, 2004)

The colour index is defined to be the ratio of the mean radiances of the two microwindows:

$$CI = \bar{L}_{MW1}/\bar{L}_{MW2}. \tag{4.1}$$

It would have been better perhaps if the Colour Index had been defined as $\bar{L}_{MW2}/\bar{L}_{MW1}$ since at high altitudes $\bar{L}_{MW2}$ will tend to zero before $\bar{L}_{MW1}$, so $\bar{L}_{MW2}/\bar{L}_{MW1}$ is more stable than $\bar{L}_{MW1}/\bar{L}_{MW2}$.

Colour Index	*MW1 (cm^{-1})*	*MW2(cm^{-1})*	*Threshold*
CI-A	$788.0 - 796.0$	$832.0 - 834.0$	1.8
CI-B	$1246.3 - 1249.1$	$1232.3 - 1234.4$	1.2
CI-D	$1929.0 - 1935.0$	$1973.0 - 1983.0$	1.8

Table 4.1: Definition of microwindows and thresholds used in the calculation of colour indices for the A, B and D bands of MIPAS. (Spang, 2004)

When the colour index is large ($CI > 4$, for conventionally chosen microwindows), cloud-free conditions exist and when the colour index is approximately unity optically thick clouds are present. The range of colour indices represents the range of optical thickness of clouds present, with thicker clouds appearing blackbody-like with $CI \approx 1$ and thinner, tenous clouds registering increasingly larger colour indices.

The presence of cloud is then determined by setting a threshold for the colour index of interest below which it is said that cloud occurs and above which, cloud is said to not occur. In the interest of only conservatively discarding data which are truly contaminated by thick cloud, a low threshold is frequently chosen, below which it is certain that cloud occurs and above which cloud is said to not occur, even though it is well known that above this threshold cloud can indeed occur, either as an optically thin cloud or by only partially filling the instrument field-of-view. (Ewen, 2005; Spang, 2004)

For MIPAS, there are colour indices defined for bands A (685.0-970.0 cm^{-1}), B (1215.0-1500.0 cm^{-1}), and D (1820.0-2410.0 cm^{-1}). Table 1.4 defines the quantities important in the calculation of the indices (the microwindows' spectral locations, and the usual threshold value) for these bands.

It should be noted that the definition of colour index breaks down above about 30 km due to decreased signal-to-noise-ratio, particularly in the more transparent and intrinsically noisier (due to smaller signal) second microwindow. Cloud detection itself gives a measure of the cloud top height, but this is limited to the height resolution of the measurement scan pattern.

4.1.3 Principle Component Analysis

Ewen attempted to apply a method based upon Principle Component Analysis (PCA) to MIPAS Level 1 spectra in the hope of finding a componenet which captures the variability of limb spectra attributable to the presence of cloud in the limb path – and hence a new cloud detection method.

PCA is a standard statistical technique (Murtagh and Heck, 1987) used for finding patterns in high dimensional data and for summarizing this data. To this end, PCA transforms a number of potentially correlated variables into a smaller number of uncorrelated variables

called principle components. The first principle component accounts for as much of the variability in the data as possible, and then each successive principle component accounts for as much of the remaining variability as possible. Ewen's use of PCA is the first attempt of application of the technique to infrared limb emission spectra to try to detect cloud presence.

Consider a set of m repeated measurements (the limb scan spectra) of a physical object with n number of properties (the atmosphere) – the dataset is then m-points in n-dimensional space $\mathbb{R}^n$. In $\mathbb{R}^n$, PCA searches for the set of best-fitting orthogonal axes to replace the set of n axes given by the initial data – and the principle components can then be thought of as a set of basis vectors in $\mathbb{R}^n$ chosen so that the maximum object-to-object variation in the data belongs to a subspace formed by the least number of basis vectors.

Ewen has binned MIPAS Level 1 scans by latitude and tangent height, and has taken limb scans in the same latitude and tangent height bin to be repeated measurements (of which there are m). He has taken the radiance measurements from $750-970$ cm^{-1} to be the measured properties (of which there are n). In each latitude-altitude bin, then, PCA is carried out upon the mxn matrix of these values $\mathbf{R} = \{r_{ij}\}$ (where r_{ij} refers to the measurement taken at the ith limb scan and the jth spectral point) by solving the eigenvalue/vector problem for the corresponding correlation matrix $\mathbf{Y} = \{y_{jk}\}$. The correlation matrix elements y_{jk} are defined as

$$y_{jk} = \frac{1}{n}\sum_{i=1}^{m}\frac{(r_{ij}-\bar{r}_j),(r_{ik}-\bar{r}_k)}{\sigma_j\sigma_k} \tag{4.2}$$

where

$$\sigma_{ij}^2 = \frac{1}{n}\sum_{i=1}^{m}(r_{ij}-\bar{r}_j)^2 \tag{4.3}$$

for

$$\bar{r}_j = \sum_{i=1}^{m}(r_{ij}. \tag{4.4}$$

Each correlation coefficient y_{jk} gives the correlation between the jth and kth variables. Then the set of p ($p < m$) principle components $\mathbf{u}$ of length n can be found simply by solving the eigenvalue/vector problem of $\mathbf{Yu} = \lambda\mathbf{u}$, for p eigenvalues λ. The eigenvalues are ordered in decreasing order of magnitude such that $\lambda_1 < \lambda_2 < \lambda_3 < \cdots < \lambda_p$ so that the ith principle component accounts for P_{var}(i) percent of the variance of the m spectra in the given bin for

$$P_{var}(i) = \frac{\lambda_i}{\sum_{j=1}^{p}\lambda_j}x100\%. \tag{4.5}$$

Ewen found that the first three principle components captured the majority of the variance while the higher order principle components accounted for the spectral noise. As well, it appeared that the total percentage of variance captured by the first three principle componenets is strongly correlated to the cloud frequency, and of these, the first principle component seems the strongest candidate to capture a spectral cloud signature.

The contribution coefficient corresponding to the ith principle component is

$$c_i = \sum_{j=1}^{n} \frac{(r_{ij} - \bar{r}_j)}{\sigma_j} u_{ij}, \tag{4.6}$$

and effectively scales the principle component. Ewen found that the contribution coefficient corresponding to the first principle component c_1 is strongly related to the A Band Colour Index, such that $c_1 << 0$ corresponds to $CI \approx 1$ (thick cloud) and that c_1 levels off to a large positive value for $CI > 4$ (clear sky). However, it is necessary to set a threshold for cloud detection in a manner dependent upon latitude and altitude - the thresholds thus determined can be found in Ewen (2005).

Ewen proposed a Principle Component Cloud Test:

1. Determine contribution coefficient c_1 for appropriate latitude-altitude bin;
2. Determine average spectral value of first spectral component $\bar{u}_1$ for appropriate latitude-altitude bin, such that $\bar{u}_i = \frac{1}{n}\sum_{j=1}^{n} u_{1j}$;
3. Determine the threshold on c_1 from Ewen's tabulated limits for appropriate latitude-altitude bin;
4. Threshold: if $\bar{u}_i < 0$ and $c_1 > c_{1thresh}$, or if $\bar{u}_i > 0$ and $c_1 < c_{1thresh}$, then cloud occurs.

4.2 Cloud Parameter Retrieval Methods

In order to determine cloud properties from measurements, the first requirement is a radiative transfer model to simulate the scattering of atmospheric thermal radiation by clouds. The Monte Carlo Cloud Scattering Forward Model (McCloudsFM) was developed by Graham Ewen (Ewen et al., 2005) to accurately model infrared limb emission measurements of cirrus clouds, and take into account multiple scattering, spherical geometry, and cloud ice particle scattering properties. McCloudsFM should be able to reproduce limb measurements to within 5% of the continuum baseline level and spectral average. (Ewen, 2005)

McCloudsFM breaks the radiative transfer problem into two steps: first computing the radiative transfer through the atmosphere and secondly, modulating the radiance to take into account the effects of the observing instrument. Obviously, in cloudy atmospheres, the scattering and molecular absorptions involved make the radiative transfer very complex. To deal with this complexity, the model splits the radiative transfer into two regimes and treats the two separately:

- **Non-Scattering Domain**: the clear sky. A line-by-line radiative transfer (Reference Forward Model RFM, Dudhia, 2004) is used to calculate the emission and transmission along the ray paths.

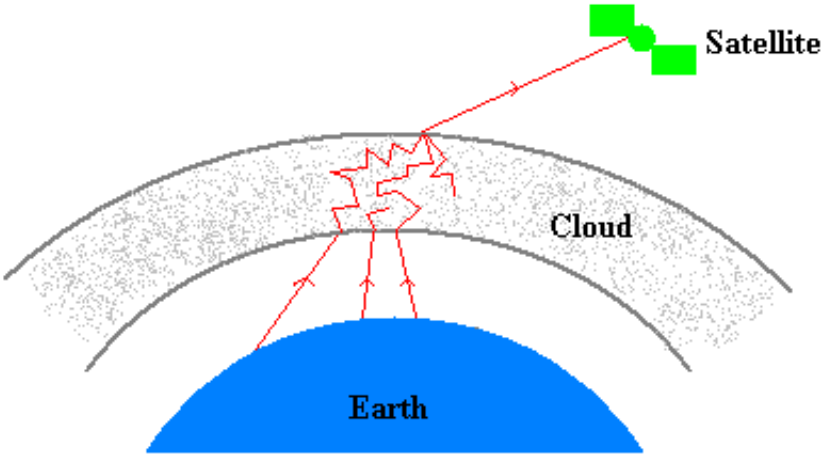

Figure 4.1: Schematic representing the reverse Monte Carlo radiative transfer method.

- **Scattering Domain**: the cloud volume. A Monte Carlo reverse scattering model is used to simulate photon trajectories from a pencil beam leaving the detector (on the satellite) and arriving at the cloud.

Effectively, McCloudsFM uses Monte Carlo radiative transfer to trace all photon paths backwards from the satellite and then calculates the corresponding radiative transfer along each path to determine the total radiance arriving at the detector, as shown in Fig. 4.1.

Due to the complexity of the problem, McCloudsFM makes several key assumptions. It assumes that

- There exists a **size distribution** that represents the whole volume of the cloud. McCloudsFM uses size distributions and scattering properties as calculated for hexagonal columns by (Baran and Francis, 2004). The size distribution is described by effective radius

$$r_e = \frac{3}{4}\frac{IWC}{\rho \sum_j n_j A_j}, \tag{4.7}$$

(n_j is the crystal concentration in the jth size bin, A_j is the mean cross-sectional area of jth bin, and ρ is the reference density of 1 g/cm^3) and number density

$$N = \int_0^\infty n(L)dL \approx \sum_j n_j. \tag{4.8}$$

- The cloud is composed of a **single non-spherical crystal habit**. This limits the degrees of freedom for the retrieved solution, and reduces complexity and computation time of the scattering calculations. This is a valid assumption as cirrus having small mean particle sizes ($< 150\mu$m), is frequently observed to have a dominant crystal

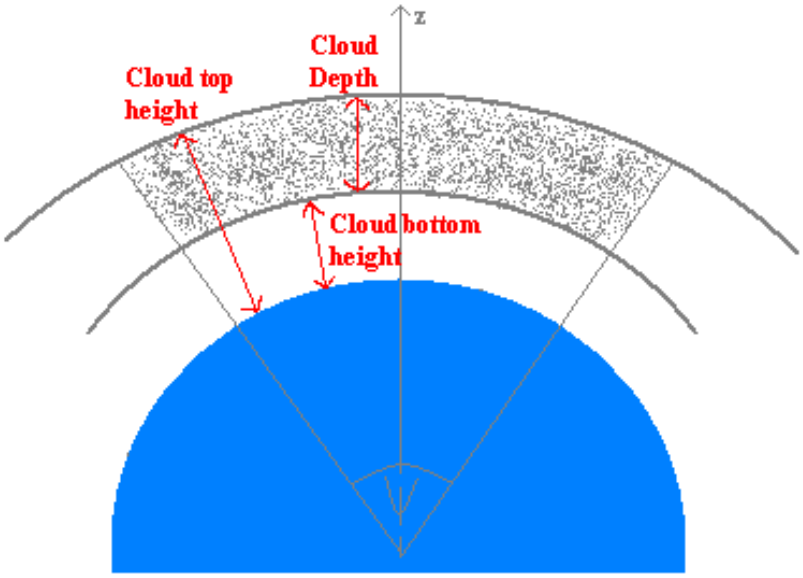

Figure 4.2: Schematic of cloud geometry assumed. The cloud is spherically symmetric about the z-axis.

habit (Heymsfield and McFarquhar, 2002). McCloudsFM is configured to use any non-spherical crystal shape as long as the single-scattering properties are accurately calculated.

- The cloud is **spatially contiguous**. Cloud is approximated as a uniform depth spherical shell layer in the atmosphere of finite extent as shown in Fig. 4.2 and, for simplicity, the detector limb view path is taken to intersect the centre of the cloud top. A contiguous cloud layer is assumed in order to simplify the calculation so that it does not have to deal with an infinite number of permutations of broken cloud in the FOV of the instrument. This assumption is valid as cirrus cloud fields are observed to have large (> 200 km) unbroken horizontal extents (Dowling and Radke, 1990).

Using these assumptions the forward model $\mathbf{F}$ is developed to accomodate a four-parameter state vector

$$\hat{\mathbf{x}_c} = [r_e, N, C_{top}, C_{depth}], \tag{4.9}$$

where r_e is the effective radius, N is the number density of the single crystal habit, and C_{top} and C_{depth} are the cloud top height and cloud depth accordingly. In accordance with standard retrieval theory then,

$$\mathbf{y} = \mathbf{F}\hat{\mathbf{x}_c} \tag{4.10}$$

for a set of measurements $\mathbf{y}$.

In the forward model, the radiative transfer process in the cloud is considered to be a stationary Markov chain whose states are photon interactions with cloud particles. When simulating a pencil beam (backwards to the detector), every photon in the beam enters the

cloud at the same angle (as defined by the viewing geometry of the tangent height), and upon entry, each photon is traced through the cloud by determining the distance between interactions (of which the outcome is either absorption and hence termination of the photon path, or scattering and hence a new travel direction for the photon) and the direction after scattering.

To reverse the trajectories thus simulated, the calculated photon exit angles from the base of the cloud are taken to be the entry angles of the photons entering the cloud and successfully being scattered through the cloud into the line-of-sight, and the terminal locations of the photons absorbed within the cloud are taken to be the initial locations of photons emitted from the cloud. Thus, there exist four possible sources of radiation entering the line-of-sight from the cloud: the non-scattered radiation coming from the limb path, the radiation scattered into the line-of-sight from below the cloud, the radiation scattered into the line-of-sight from above the cloud, and finally the radiation emitted within the cloud and scattered into the line-of-sight.

So, the radiance arriving at the satellite is

$$R_{sat}(\nu) = f_o(\nu)R_{limb}(t_h) + (1 - f_o(\nu))[R_{exit}(\nu)T_{cld-sat}(C_{top}, \phi_{exit}, \nu) + R_{cld-sat}(C_{top}, \phi_{exit}, \nu)], \tag{4.11}$$

where $f_o(\nu)$ is the fraction of the total photons in the pencil beam arriving at the satellite which have been neither scattered nor absorbed in the cloud, $R_{limb}(t_h)$ is the radiance from emission along the limb viewing ray path with tangent height t_h (calculated by RFM), $R_{exit}(\nu)$ is the radiance exiting from the cloud in the direction of the satellite, $T_{cld-sat}(C_{top}, \phi_{exit}, \nu)$ and $R_{cld-sat}(C_{top}, \phi_{exit}, \nu)$ are the (RFM calculated) transmission and emission from the exit point from the cloud to the satellite for exit angle ϕ_{exit}.

Here R_{exit} has been defined as

$$R_{exit} = f_{bot}(\nu)R_{bot}(\nu) + f_{top}(\nu)R_{top}(\nu) + f_{cloud}(\nu)R_{cloud}(\nu), \tag{4.12}$$

where $f_{bot(top)}(\nu)$ is the fraction if photons entering the cloud from its bottom (top) and scattered into the line-of-sight, $f_{cloud}(\nu)$ is the fraction of photons emitted from the cloud entering the line-of-sight such that

$$f_{bot}(\nu) + f_{top}(\nu) + f_{cloud}(\nu) = 1, \tag{4.13}$$

$R_{bot(top)}(\nu)$ is the up(down)welling radiance from below (above) the cloud redirected into the field-of-view and R_{cloud} is the radiance emitted within the cloud directed into the field-of-view. Consult Ewen et al. (2005) for further details.

Ewen uses this described forward model in the inverse problem: the optimal estimation retrieval McCloudsRT is used to determine the cloud state vector $\hat{\mathbf{x}}$ which is the most-likely estimate fitting the measurements $\mathbf{y}$ for a given a priori $\hat{\mathbf{x_a}}$ and covariance $\mathbf{S}_a$. Since McCloudsFM is non-linear, the inverse problem is non-linear as well and thus an iterative

method (Levenberg-Marquardt) is used to find a solution by minimising the cost function. Again, the details of the retrieval scheme can be found in Ewen et al. (2005).

In summary, it is possible to retrieve four cloud parameters (effective radius r_e, number density N, cloud top height C_{top} and cloud depth C_{depth}) from limb measurements of clouds; however, there are a few caveats in using this retrieval. Firstly, the computational time associated with the retrieval is prohibitively slow, taking up to 100 minutes per iteration on a 1.1 GHz CPU with 1 GB of RAM. Secondly, the scattering properties of the cloud particles have to be defined in advance and there is no guarantee that the correct type is chosen. Thirdly, due to the non-linearity of the problem and possibly the jaggedness of the optical properties chosen, the cost surface is not smooth, and often (80% of the time) has local minima into which the retrieval can fall. Given the appropriate a priori, McCloudsRT can successfully retrieve r_e to within 2μm, N to within 20%, C_{top} to within 0.2 km and C_{depth} to within 25%, but there is no guarantee that the retrieval will converge, or that when it does, that it converges to the correct values and not to those corresponding to local minima.

4.3 Room for Improvement

Taking MIPAS as the instrument of study, there exist methods (as discussed) for both the detection of clouds and the retrieval of cloud parameters. However, there are issues concerning further development of both the detection and retrieval mechanisms presently used.

A rigorous detection method is necessary not only to flag "contaminated" data for trace gas retrievals and so forth, but to make sure that all possible cloud is accounted for in the construction of climatologies. Kasprzyk (2002) showed that the tried-and-trusted Colour Index Method is fairly reliable over a range of altitudes and latitudes, however that the Colour Index Methods will usually only detect cloud when more than half of the field-of-view of the instruement is cloud-filled. For MIPAS, a natural progression of detection is to avail of the five spectral bands and use, say, the Colour Index Method in each to provide a more reliable detection mechanism. The Colour Index Method has been for quite some time with good success in the A band; however, it has been suggested that the D band is a suitable candidate to supplement the A band results. Chapter 5 presents a study of the unsuitability of this suggestion.

Furthermore, while McCloudsFM and McCloudsRT are state-of-the-art cloud parameter forward models and retrievals, the complexity of the the system lead to crippling caveats, as previously discussed. In fact, the assumption taken by the McCloudsFM forward model that the MIPAS field-of-view is completely and homogeneously cloud filled is not necessarily true. There exist four possible states of the field-of-view that are frequently all encountered: completely-and-homogeneously-cloud-filled, partially-but-homogeneously-cloud-filled, inhomogeneously-cloud-filled and empty, as shown in Fig. 4.3. Inhomogeneous field-of-views are nearly impossible to retrieve without prior knowledge of either the macrophysics or the microphysics of the system. However, partially-but-homogeneously-cloud-filled field-of-views

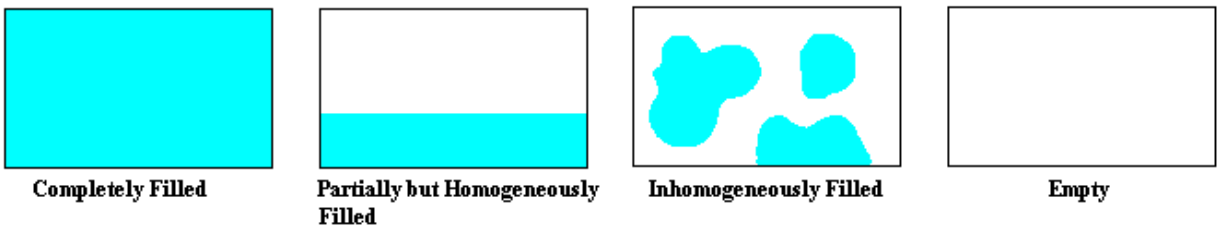

Figure 4.3: Schematic of possible cloud filled MIPAS field-of-views.

may indeed represent a more accurate model of the measured cloud radiance.

Using Kasprzyk's (2002) result of the Colour Index corresponding to various fractional fillings of the field-of-view, as shown in Fig. 4.4, a one day period of MIPAS Level1B data was used to estimate the relative frequency of occurrence of each state of the field-of-view. Considering only sweeps in which cloud is likely to occur (6 km - 18 km), a filter was applied to the profiles such that a field-of-view was consered to be fully-cloud-filled if CI < 1.2, to be partially-cloud-filled if $1.2 <$ CI < 3, and to be empty and fully clear if CI > 3. The results of this filtering are shown in Fig. 4.5 - clearly the partially-filled field-of-view is the predominant state. However, it must be noted that the inhomogeneously cloudly field-of-views are impossible to easily separate from this analysis and from Kasprzyk's (2002) work one can confidently say that inhomogeneously-filled field-of-views which are completely filled by multiple cloud layers of varying optical thickness have been binned as "completely filled" whereas inhomogeneously-filled field-of-views which are dotted with cloud and clear sky have been binned with the partially-cloudy cases. Chapter 6 presents several methods which aim to simply model the radiance emerging from a partially-but-homogeneously-cloud-filled field-of-view.

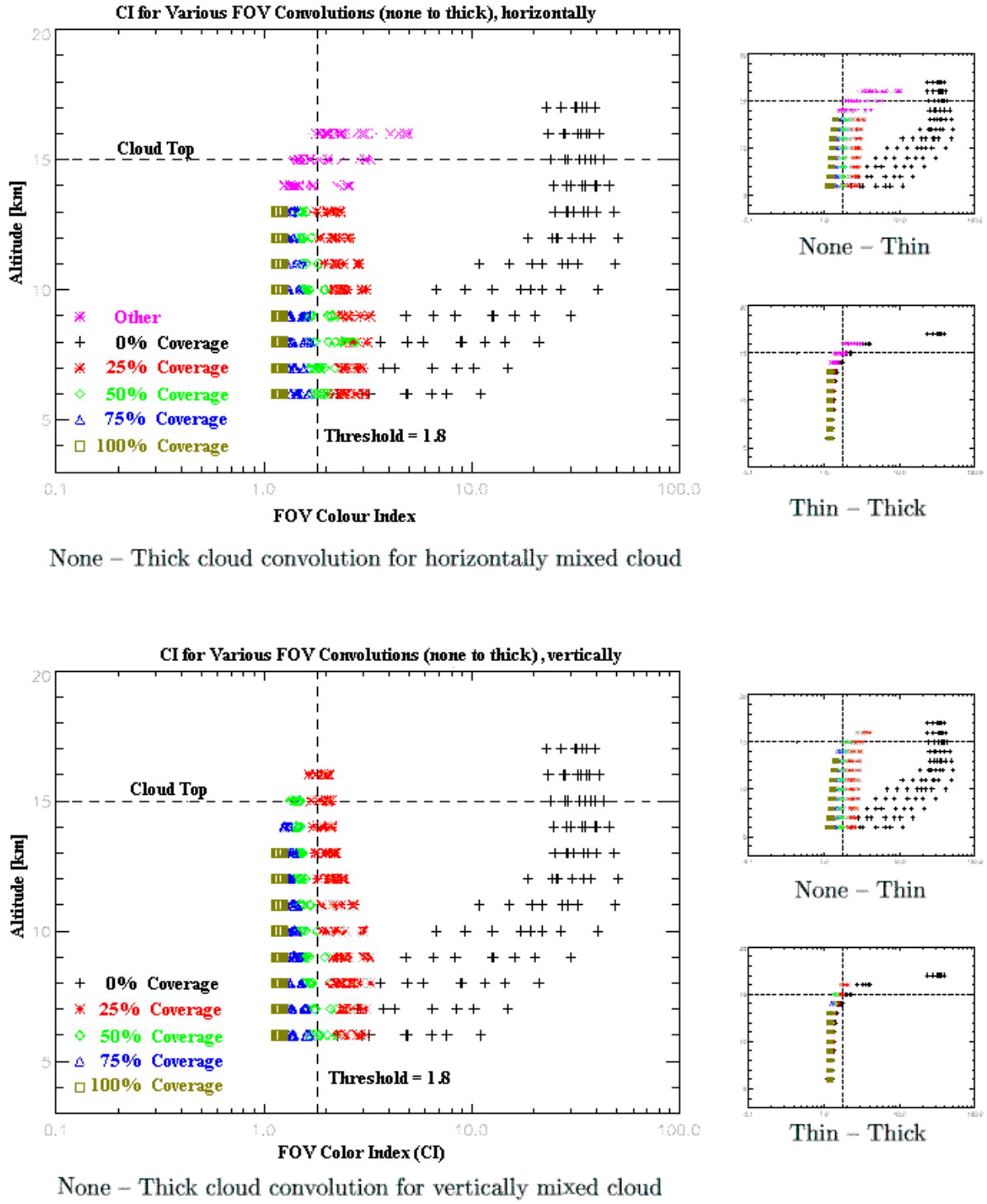

Figure 4.4: Colour Indices for various field-of-view filling convolutions, whereby a thick (thin) cloud covers increasingly higher percentages of the field-of-view. The case where there is an inhomogeneous field-of-view being filled by varying proportions of thick and thin cloud is also studied.

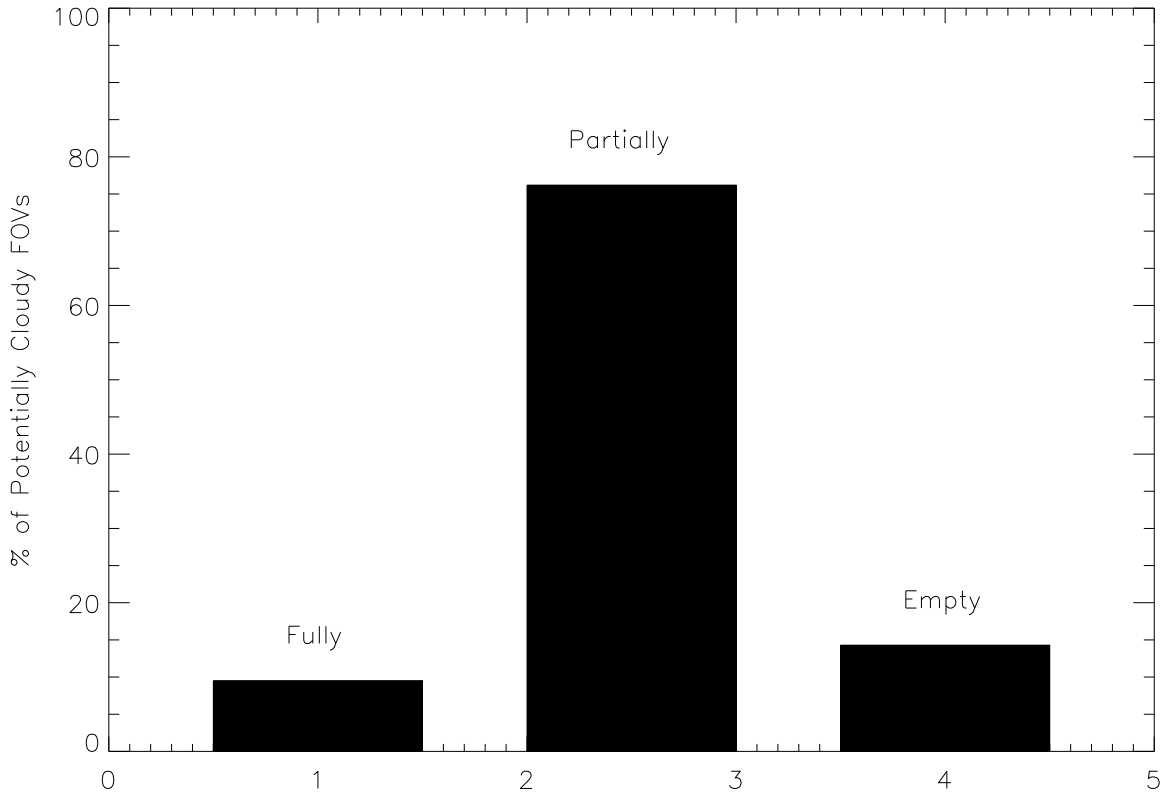

Figure 4.5: Relative predominance of fully-cloud-filled, partially-cloud-filled and empty field-of-views of MIPAS, considering only sweeps in which cloud is likely to occur (6 km - 18 km).

Chapter 5

D Band Cloud Flagging Anomaly

It is conventionally accepted to use the Colour Index (CI) Method to detect ("flag") cloud in satellite measurements. In the past, the A band has been confidently used to flag the presence of cloud in MIPAS measurements. It is a useful check to use the other bands available as a verification of cloud as well, and for the most part the colour indices calculated for the different spectral bands yield the same result. Generally, the A and B bands exhibit similar variability while the D band varies much more significantly.

As would be quite predictably expected, there are instances in which the cloud detection by way of calculated colour indices for the various MIPAS bands do not agree. However, quite frequently the D band flags cloud while the A band does not. This is an important observation since it may be possible that the D band may be better suited to detect certain cloud types than the tried-and-trusted A band, and hence occasions whereby the D band flags cloud while the A band does not are treated as flagging anomalies. There are also cases in which it is only a certain part of the spectrum which is affected by a particular cloud type – for instance, the C and D bands are strongly affected by solar scattering from polar stratospheric clouds (PSCs) so it has been suggested that stratospheric retrievals during winter days need to use the D band cloud flag rather than those of the other bands. As well, it has been suggested that there is a correlation between this flagging anomaly and unrealistically low water vapour volume mixing ratio retrieved values which, it was thought, may be due to such band-dependent cloud effects since water vapour is retrieved using the C band. Furthermore, there appears to be a day/night difference in the behaviour of the D band and indeed in terms of the frequency of cloud flagging. (Remedios, January 2005; Remedios, April 2005; Remedios, September 2005)

This work investigates the behaviour of such anomalous points of MIPAS data using the colour index method as the cloud detection technique, looks at the day/night difference in the D band, and addresses the association of the anomaly with very low water vapour volume mixing ratios.

5.1 General Behaviour of A and D Band Colour Indices

The ESA Level 1B spectra for the day of 15 August 2003 were used to calculate the colour indices for the D and A bands. The general rule of thumb is to threshold the indices CI-A and CI-D at 1.8, whereby below this value there is definitely cloud and above this value there is no optically thick cloud, although there has been speculation regarding lowering the D band threshold to 1.2 (Remedios, September 2005). It should be noted however that optically thin cloud or optically thick cloud partially filling the field-of-view can occur with colour indices up to 3 or 4. For comparative purposes, Fig. 5.1 shows the height distribution of the colour indices of all of the data points measured on 15 August 2003. The A band colour index behaves in a manner that is expected, detecting cloud (CI-A < 1.8) at lowish altitudes ($5 - 20$ km) and not detecting cloud in higher regions where there should not be cloud climatologically ($20 - 30$ km). Above 30 km, the definition of cloud index breaks down due to noise, so it is unimportant that the CI-A values reported for such higher altitudes have quite low values. The D band colour index is less convincing. It does indicate detection of clouds in the lower altitude range where clouds are indeed expected, however the D band exhibits positive detection of clouds in the higher altitude range where there should be no cloud registered. Clearly the A band seems to more reliably flag cloud, whereas the D band, by contrast, detects cloud where simply none should exist.

5.2 Low H_2O Volume Mixing Ratio and Flagging Anomaly

Previous work done (Remedios, January 2005; Remedios, April 2005; Remedios, September 2005) noted that in the Southern Hemisphere wintertime there was a correlation between the D band flagging but the A band not flagging cloud and unrealistically low values of water vapour volume mixing ratio (10^{-10} ppmv). These 10^{-10} ppmv values occur when the retrieval records negative values of water vapour volume mixing ratio and are placed simply as a marker of poor data retrieval. If a correlation does exist between the flagging anomaly and these low water vapour volume mixing ratios, occurrence of the anomaly could be used to predict and avoid bad water vapour retrievals. Fig. 5.2 shows the existence and altitude distribution of these low water vapour retrieval points for an arbitrary test day, 15 August 2003.

As a starting point, all of the ESA retrievals (version 4.61) for 15 August 2003 were filtered to locate the points having water vapour vmr of 10^{-10} ppmv. Fig. 5.3 shows the geolocation of these points for the day, highlighting whether or not they are day- or night-time points and the altitude range of the tangent height. It is obvious that there exists a fairly random distribution of these points, but that there does appear to be a higher concentration of these in the southern polar region, at fairly low altitudes (less than 20 km) and primarily at night, although this just reflects the fact that it is Antarctic night for latitudes greater than 71°S.

From the corresponding Level 1B data, colour indices for both the D and A bands were

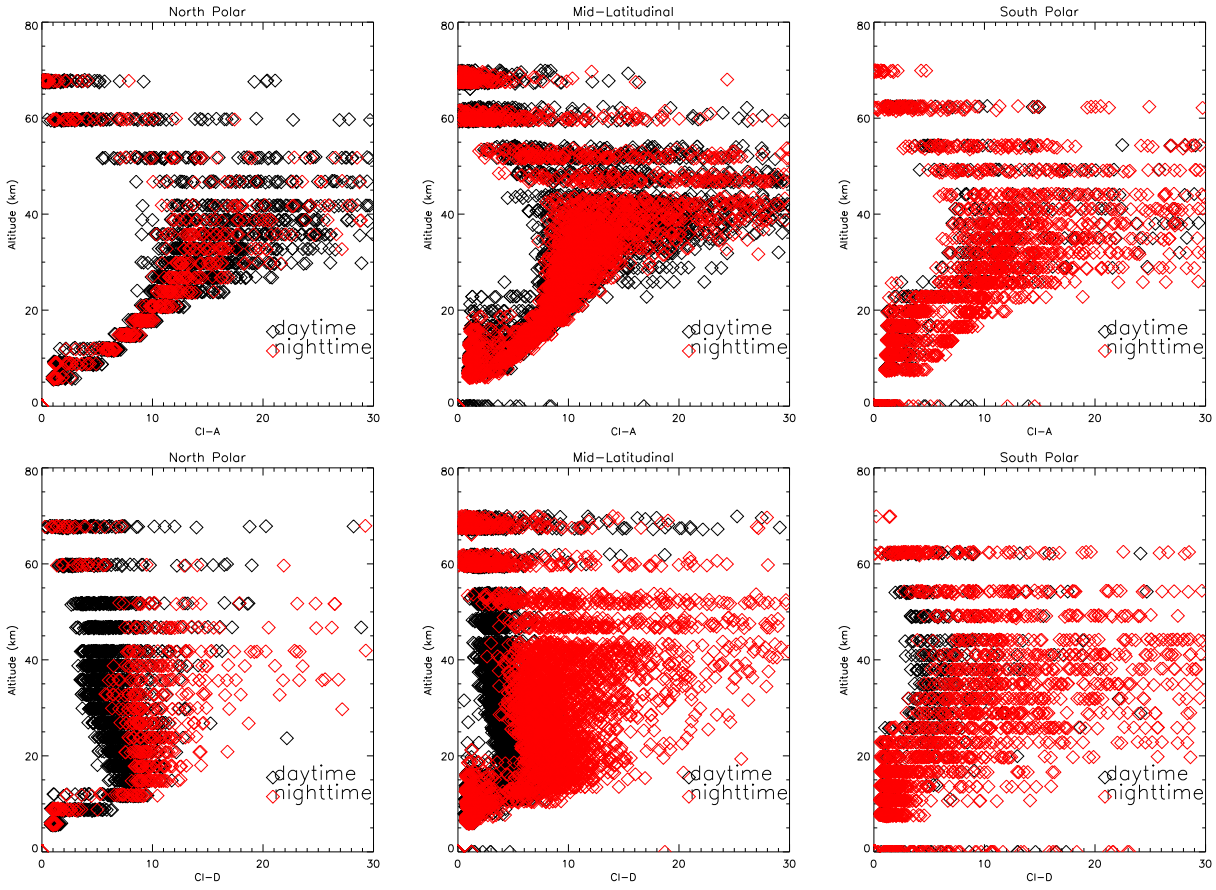

Figure 5.1: Height distribution of CI values for all data points taken on 15 August 2003, filtered into three latitude bins (north polar [60N, 90N], mid-latitudinal [60S, 60N] and south polar [60S, 90S]) and into day- and night-time measurements.

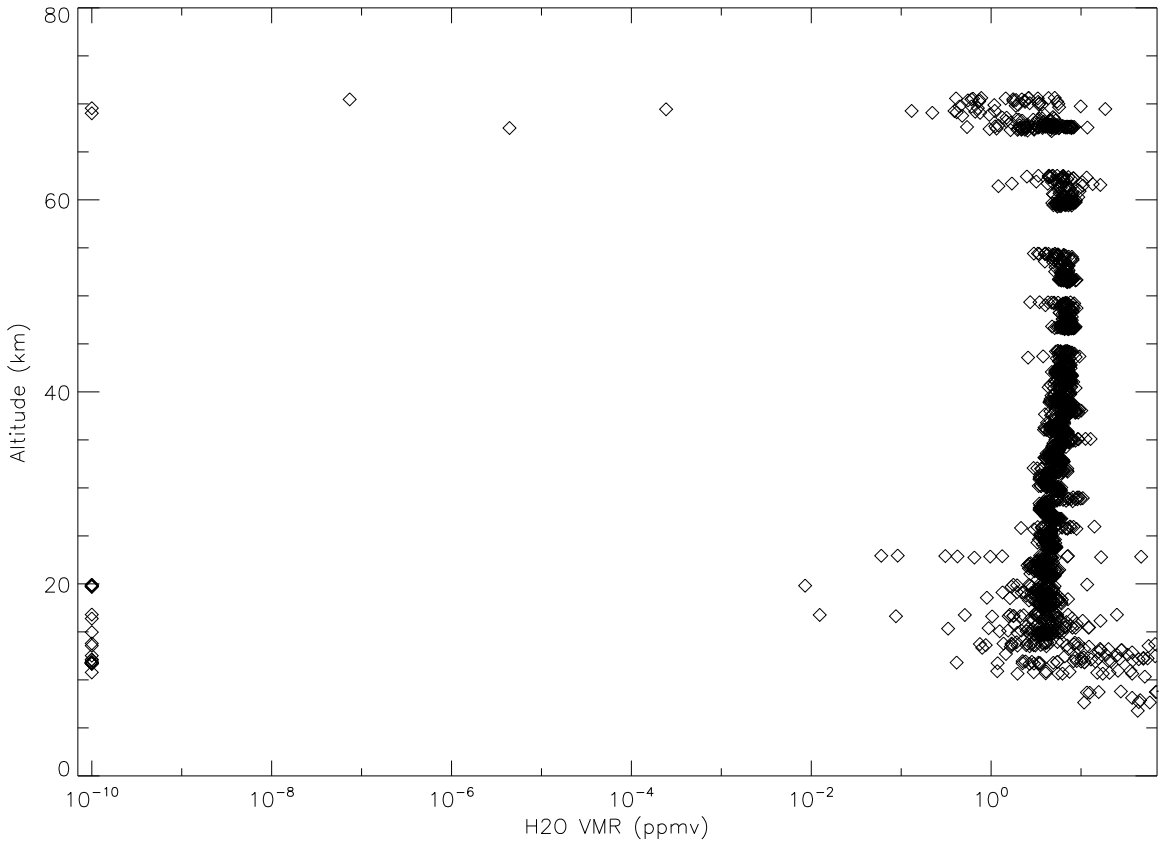

Figure 5.2: ESA retrieved water vapour profiles for 15 August 2003. Note the extremely low 10^{-10} ppmv values.

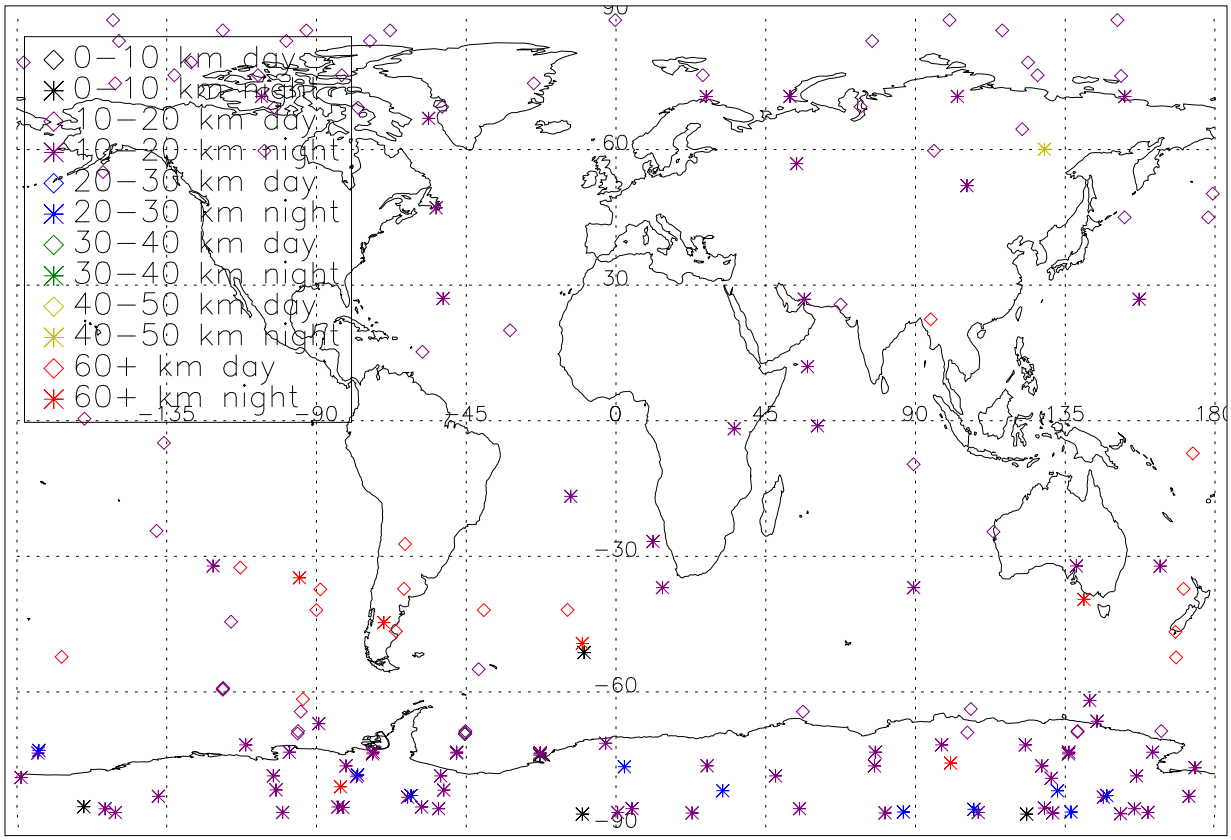

Figure 5.3: Points having extremely low (10^{-10} ppmv) water vapour volume mixing ratio values for 15 August 2003.

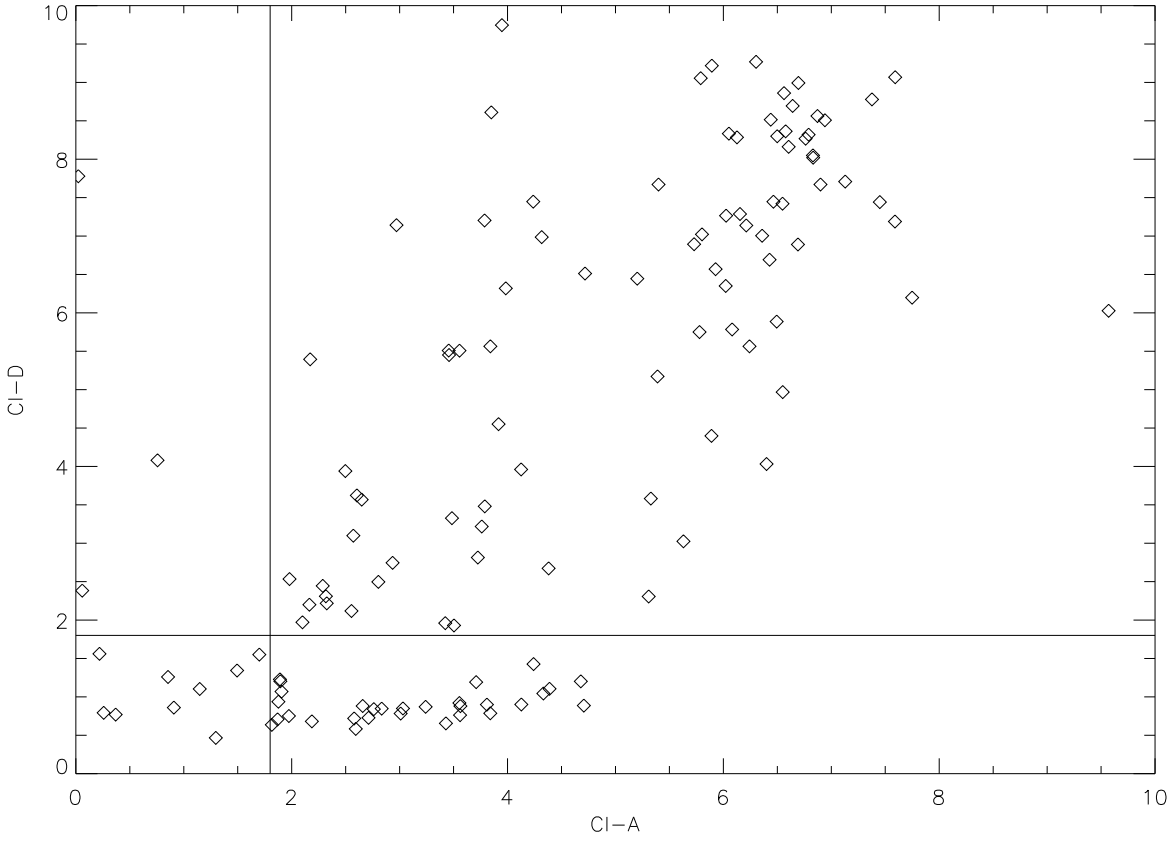

Figure 5.4: Colour indices for the D and A bands of points having extremely low (10^{-10} ppmv) water vapour volume mixing ratio values for 15 August 2003. Note the threshold value of cloudiness is 1.8 in both the A and D bands. For the remainder of this work, we will use a threshold of 1.8 for the D band.

calculated and, if for a given data point the D band flagged cloud but the A band did not flag cloud, an anomalous flagging event was said to occur. It was found that if a measurement had such a low water vapour volume mixing ratio, then 20% of the occurrences exhibited the flagging anomaly. Fig. 5.4 shows the corresponding colour indices for the A and D bands of the low water vapour volume mixing ratio values plotted against each other – clearly there exist quite a few instances of this anomaly.

Looking at the region of interest, where CI-D $\leq$ 1.8 but CI-A $\geq$ 1.8 (D flagged but A unflagged), Fig. 5.5 indicates that most of the instances occur in the southern polar region at daytime and hence can be, given the altitude registered, taken to be polar stratospheric clouds. It is important to note, however, that even though the A band technically does not flag the presence of these PSCs, CI-A is still sufficiently low in most of the cases that it would be assumed that cloud existed. The majority of the mid-latitude cases registered are noted to correspond to high altitudes (tangent heights of more than 45 km) and are disregarded

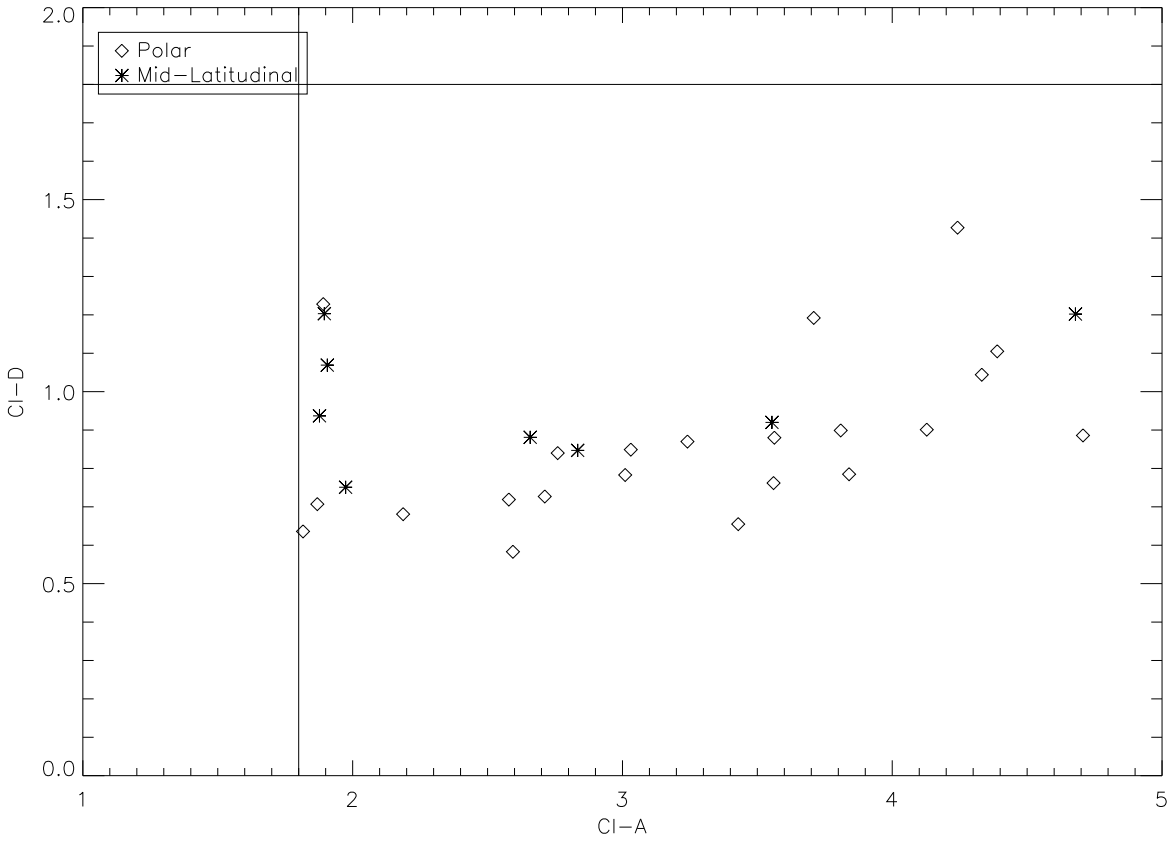

Figure 5.5: Colour indices for the D and A bands of points having extremely low(10^{-10} ppmv) water vapour volume mixing ratio values for 15 August 2003 within the region of interest where the D band is flagged as cloud but the A band remains unflagged.

since the definition of colour indices breaks down at about 30 km altitude due to increased noise levels.

Conversely, starting first with the Level 1B data and calculating the colour indices, the anomalous flagging situations were obtained. Using then the corresponding Level 2 retrievals, it was checked if for the given anomalous event the retrieval showed a low water vapour retrieval. It was found that 8% of the flagging anomalies had low water vapour volume mixing ratios and could thus be associated with bad water vapour retrievals.

The correlation between the flagging anomaly and the extremely low water vapour volume mixing ratio retrievals is thus weak at best, and hence occurrence of the anomaly cannot be used as a detection mechanism for bad water vapour retrievals. For instance, if one were to use the flagging anomaly as a filter for poor water vapour retrievals, in all probability over 90% of the discarded data would indeed have yielded good retrievals.

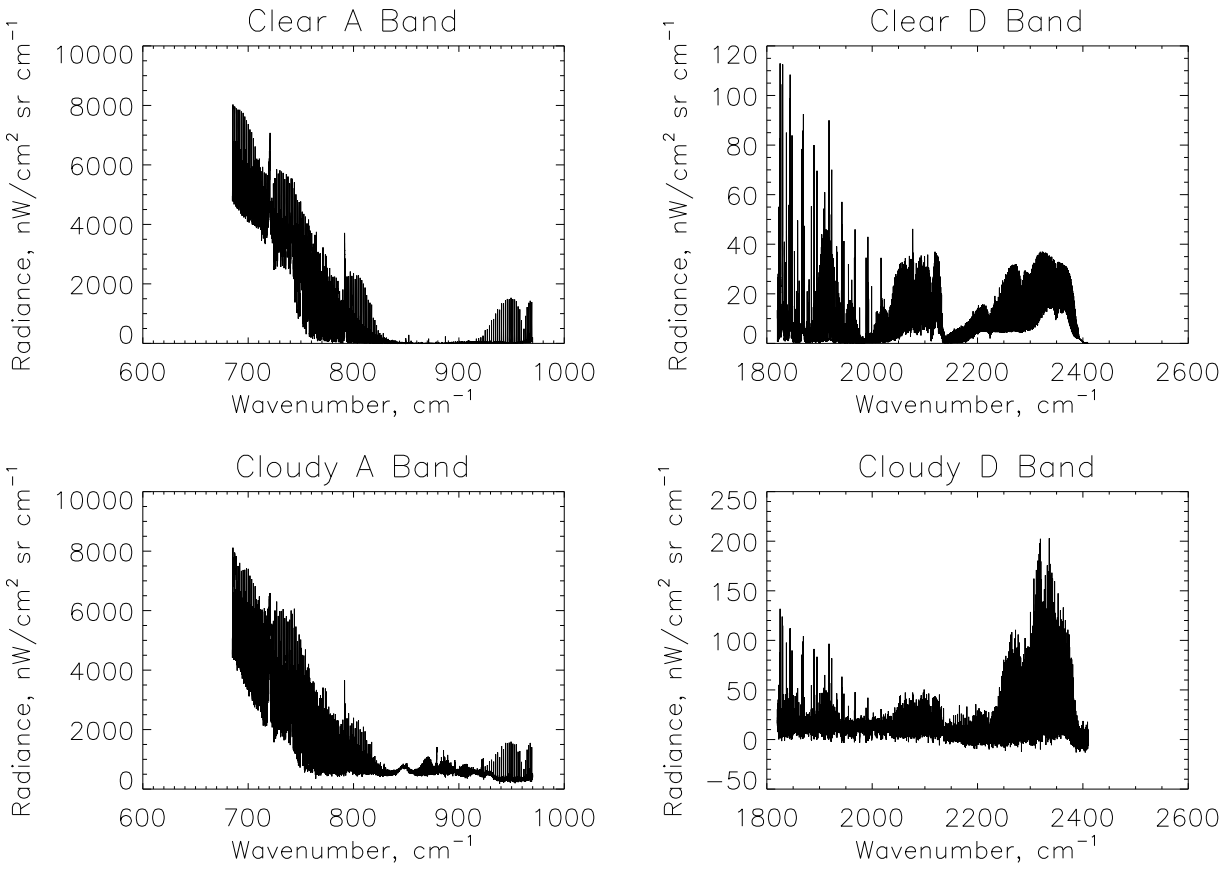

Figure 5.6: Standard clear sky and cloudy radiance spectra in the two bands of interest, A and D. These spectra are measured 16 km tangent height day-time spectra for which the clear case has been chosen to have CI-A >> 1.8 and the cloudy case has been chosen to have CI-A << 1.8. The day-time spectra are shown since they are representative of the night-time spectra as well, except in the case of a single non-LTE feature in the day-time D band spectra which is not present at night.

5.3 Radiance Spectra of Anomalous Points

Next, the radiance spectra of the lower-altitude mid-latitude instances were compared with standard spectra obtained from the RFM (including the ten most absorbing atmospheric species and non-LTE effects) and experimentally from Level 1B data. Fig. 5.6 exhibits the standard daytime clear sky and cloudy radiance spectra in the A and D bands.

It is worth noting that several definitive features of the standard spectra:

- A band clear: level zero-magnitude baseline; day/night spectra have same relative shape, as represented by the day-time spectrum shown in Fig. 5.6;
- A band cloudy: slanted above-zero baseline; day/night spectra have same relative shape, as represented by the day-time spectrum shown in Fig. 5.6;

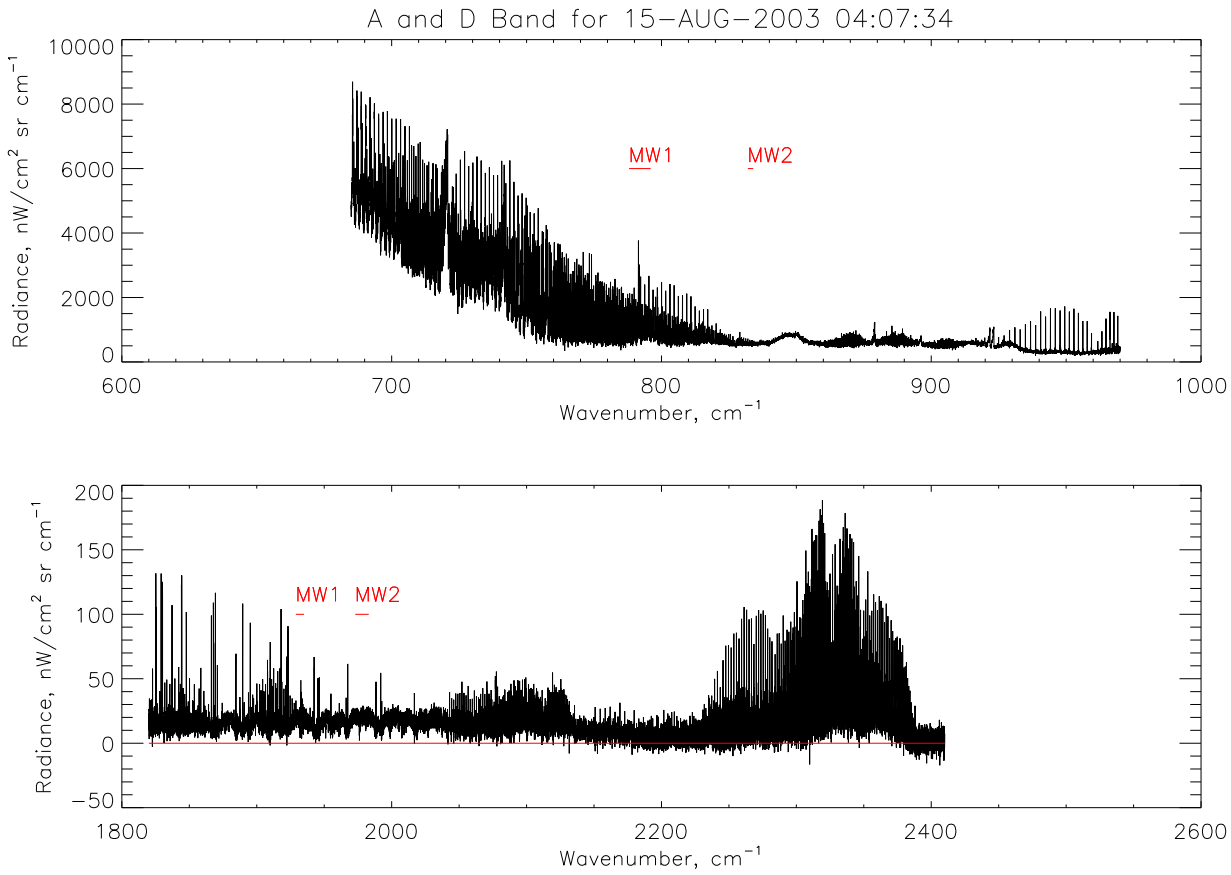

Figure 5.7: A low altitude, mid-latitude example where the D band flags cloudy and the A band does not flag. Here CI-D = 0.94, CI-A = 1.88, latitude = $-9.6°$, altitude = 16.4 km and it is daytime.

- D band clear: level zero-magnitude baseline; day/night spectra have same relative shape, as represented by the day-time spectrum shown in Fig. 5.6;
- D band cloudy: slanted above-zero baseline; daytime spectra exhibits large non-LTE feature at approximately 2350 cm^{-1} in the CO_2 band;

Comparing these standard spectra to the anomalous spectra (an example of which is shown in Fig. 5.7), it is obvious that, for most of the cases, the A band, though unflagged, does appear to have cloudy spectra. The D band appears to have a non-LTE feature at approximately 2350 cm^{-1} but "matches" the cloudy "day" standard spectrum.

In the hope of being able to eliminate cloud presence as a possible cause of these anomalies, a search was carried out for instances of low water vapour vmr having the D band flagged for cloud but the A band unflagged in an altitude range of $20 - 30$ km, where there should be no clouds in the mid-latitudes. For the test day, there were no such cases, so the search

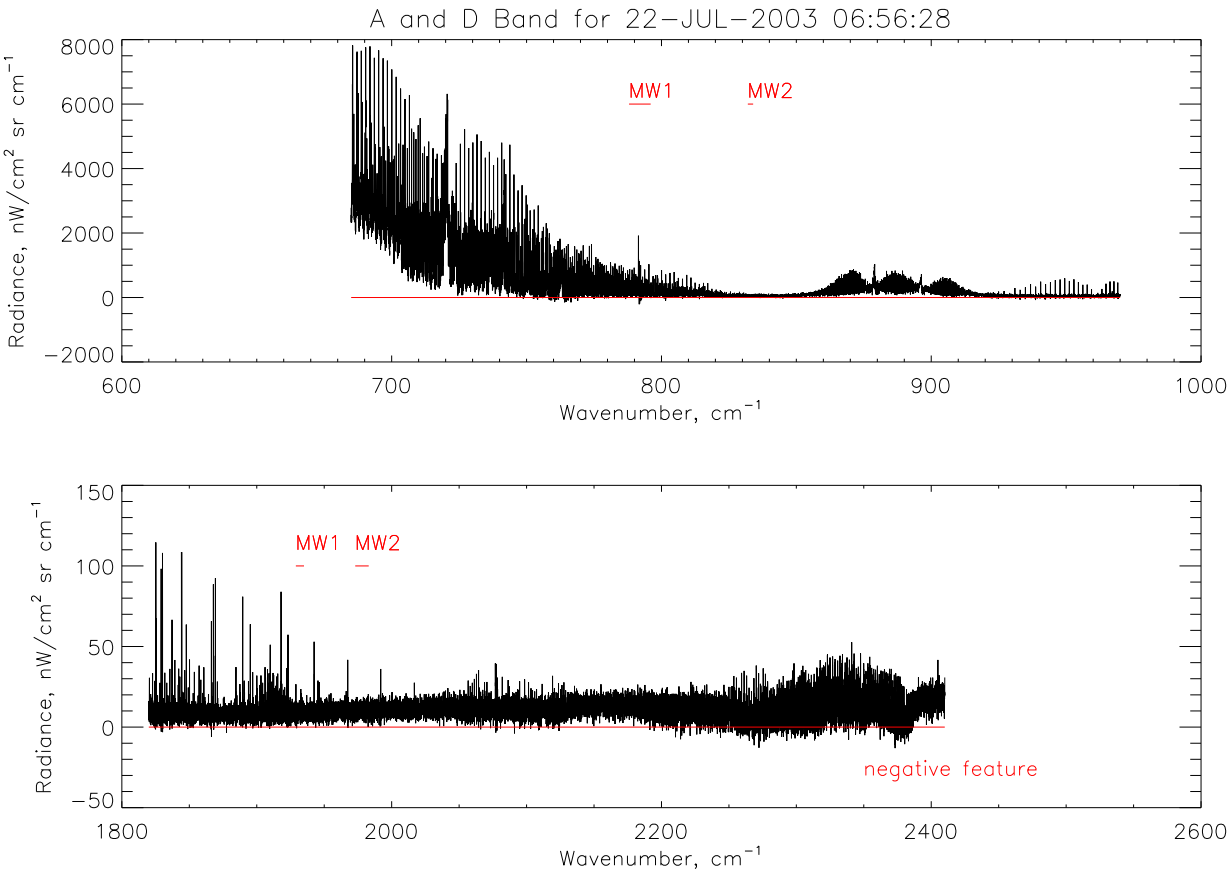

Figure 5.8: A higher altitude, mid-latitude example where the D band flags cloudy and the A band does not flag. Here CI-D= 0.95, CI-A = 3.55, latitude = −58°, altitude = 22.3 km and it is daytime.

was extended to a month's worth of data. For the month of 15 July 2003 to 15 August 2003, there were only four points showing extremely low water vapour vmr in the mid-latitudes in the desired altitude range and, of these, unsatisfyingly two registered as having flagged D bands but unflagged A bands and the other two points both registered resoundingly as having no clouds present with colour indices of greater than eleven. Hence, it can be neither confirmed nor denied that cloud presence could be causing the flagging anomaly.

Fig. 5.8 shows the spectrum of one of the two D band flagged spectra. The A band appears to have a clear spectrum, as supported by the relatively high CI-A value of 3.55; however the D band has a strange negative feature located approximately where the non-LTE feature was in the lower-latitude examples (approximately at 2350 cm^{-1}). This negative feature is a fairly strong argument for errors from some source in such spectra.

In fact, it may be that the D band may not be such a reliable candidate for cloud flagging. Since cloud spectra should essentially limit to the Planck blackbody function, it is

	190 K	*203 K*	*209 K*	*219 K*	*224 K*
CI-D	1.32	1.29	1.28	1.26	1.25
CI-A	1.17	1.15	1.14	1.13	1.12

Table 5.1: Colour indices calculated for the Planck blackbody function. Since the Planck function describes a blackbody (such as an optically thick cloud), all colour indices should be flagged as cloudy – ie. having values less than 1.8.

reasonable to expect that the Planck function should always register a positive cloud flag. Using typically height-varying temperatures, the colour indices for the Planck function were evaluated for the A and D bands. It was found that the Planck function for a blackbody (such as an optically thick cloud) at a temperature T_B is reliably flagged as a thick cloud in the tried-and-trusted A band and, while the D band does a fairly good job of detection here, the margin between the threshold and the colour index value is small at lower brightness temperatures. As well, since some suggest that the D band threshold should be lowered to 1.2, this result immediately indicates that for most atmospheric temperatures the D band colour index would not flag a blackbody. Table 2.1 highlights the colour indices for the Planck function evaluated at temperatures consistent with ECMWF results.

To further investigate this, the Reference Forward Model (RFM) was used to model clear and cloudy atmospheric conditions in mid-latitudinal, equatorial, summer polar and winter polar regions. The cloudy atmospheres have been defined by creating an optically thick region of aerosols which extend from the ground to one kilometer above the tangent height of the simulation, in a step-function fashion. Shown in Fig. 5.9, it is obvious that the D band colour index is quite unreliable as a cloud detection method, frequently indicating clear or cloudy conditions for the opposite input atmospheric state.

So, clearly, there is something fundamentally wrong with using the D band as a reliable cloud flagging candidate range.

5.4 Statistics

The phenomena studied occur quite rarely. Table 2.2 highlights statistics of occurrence for the low H_2O vmr for the test day of 15 August 2003.

Table 2.3 highlights statistics of occurrence for the flagging anomaly for the test day of 15 August 2003.

5.5 Conclusions and Recommendations

The correlation between the flagging anomaly and the extremely low water vapour volume mixing ratio retrievals is quite weak, with the flagging anomaly having an 8 % occurrence rate for low water vapour volume mixing ratio and conversely with the low volume mixing

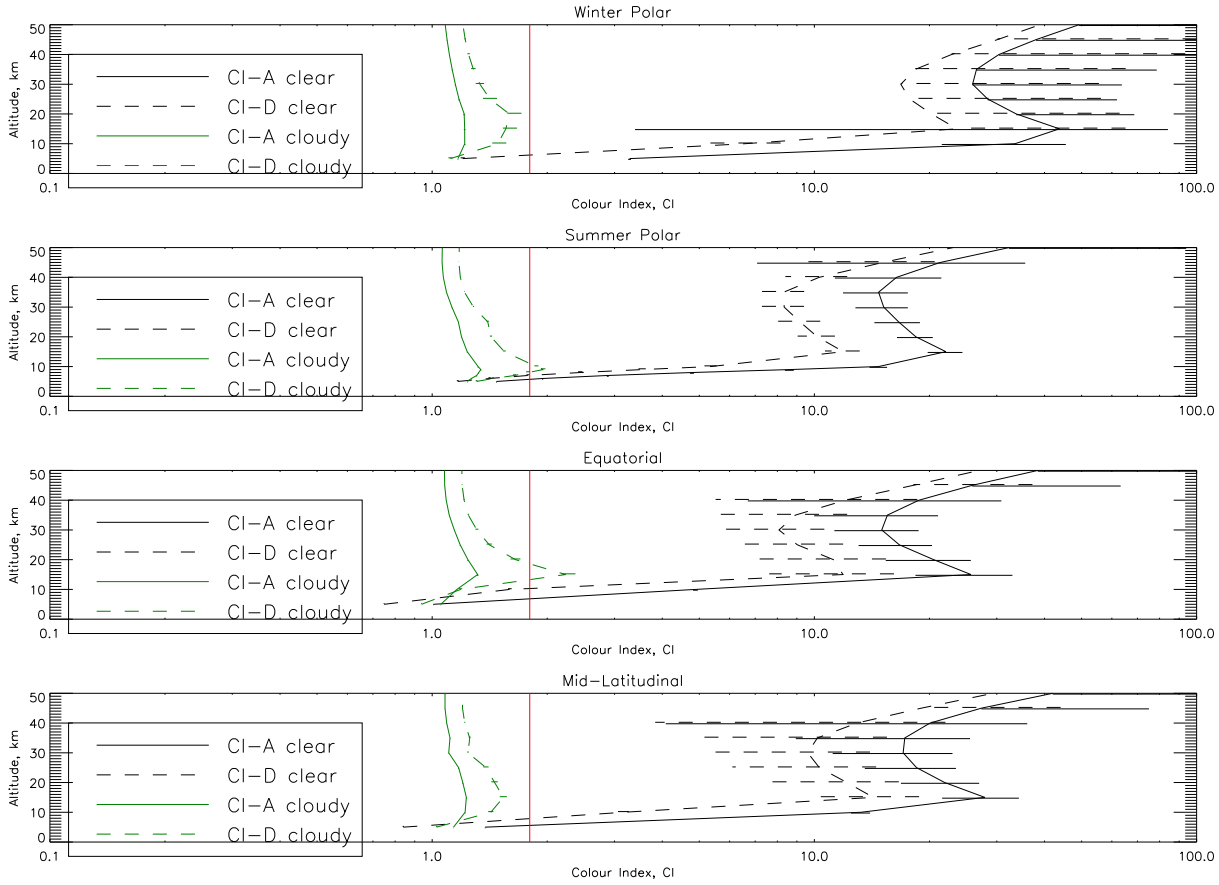

Figure 5.9: Colour indices with uncertainty bars for RFM simulated MIPAS data in clear and cloudy atmospheric conditions.

Occurrence of low H_2O vmr 1.44% (173/12041)	
day/night	42.8% (74/173) daytime
	57.2% (99/173) nighttime
altitude	78% (135/173) $10-20$ km
	5.8% (10/173) $20-30$ km
latitude	68.8% (119/173) polar
	31.2% (54/173) mid-latitudinal
flagging	17.9% (31/173) D flagged/A unflagged
	82.1% (142/173) otherwise

Table 5.2: Statistics of Occurrence for low H_2O vmr.

Occurrence of flagging anomaly 2.93% (353/12041)	
day/night	44.8% (158/353) daytime
	55.2% (195/353) nighttime
altitude	45.8% (162/353) $5-10$ km
	47.5% (168/353) $10-20$ km
	6.8% (23/353) $20-30$ km
latitude	37.4% (131/353) polar
	62.6% (222/353) mid-latitudinal
H_2O vmr	8.2% (29/353) low
	91.8% (324/353) normal

Table 5.3: Statistics of Occurrence for the flagging anomaly.

ratio having a 20 % occurrence rate of the flagging anomaly. The minimal associability of low water vapour volume mixing ratio with the flagging anomaly implies that detection of such anomalies should not be used as a detection mechanism for bad water vapour retrievals.

The D band might well be showing an increased sensitivity to clouds, but if it is indeed, it does not do so reliably. The D band flags cloud where climatologically there is simply none expected (ie. $20-30$ km altitude in the mid-latitudes, see section 5.4). At higher altitude ranges, when the D band detects cloud but the A band does not, there generally exists a strange negative spectral feature at approximately 2350 cm^{-1}, a telltale sign of possible data issues (see section 2.4). In the lower altitude range where cloud presence is expected, the cases where the D band flags cloud while the A band does not are mostly quite marginal, having both indices quite close to the threshold and the A band spectra appearing cloudy in any case (see section 2.3) and there generally exists a large non-LTE feature in the cloudy D band spectra (mid-latitude cases only – polar cases have smaller features in the same spectral location).

Most compellingly, even the limiting case of an optically thick cloud in the field-of-view (as modelled as a Planck blackbody and using the Reference Forward Model) is not consistently detected using the colour index method in the D band, while it is resoundingly detected as a thick cloud in the A band (see section 5.4).

In conclusion, the analysis indicates that the D band is not reliable for detecting cloud using the colour index method, particularly during the daytime. The anomalous cases for which cloud is detected in the D band but not in the A band appear to result from the unreliability of the D band cloud flag CI-D and possibly from contaminated data.

Chapter 6

Cloud Top Height Retrieval

At low tangent heights, clouds are frequently detected in the field-of-view and, when retrieving profiles of atmospheric composition, cloud-contaminated spectra are usually excluded. However, clouds themselves are of great interest scientifically, playing an active role in the radiative budget of the Earth in varying manners dependent partially on the micro- and macro-physical properties of the cloud, such as cloud top height, cloud depth, particle number density and effective radius. It is therefore worthwhile to analyze cloud-contaminated spectra, in the interest of learning about clouds. (Albrecht, 1992)

Probably the most intuitive cloud parameter of interest is the cloud top height (C_{top}). It is most convenient to detect cloud and to retrieve the parameter of interest, such as C_{top}, from the measured MIPAS spectra (level 1B/C data), before many resources have been consumed in processing of the data. The existing method for retrieving C_{top} is Colour Index (CI) (Spang, 2004), which basically works on the principle of a ratio of mean radiance in two carefully selected spectral microwindows. The CI method reliably detects cloud within ± 3 km. However, with the high vertical resolution provided by the MIPAS instrument's field-of-view (FOV), we should be able to retrieve C_{top} at a higher vertical resolution than taken advantage of in the CI method.

In this preliminary study, we have used simple models of clouds in the infrared to effectively model thick, flat clouds, such as those found frequently in the mid-latitudes, with a high degree of vertical resolution of ± 0.25 km. The methods presented all rely upon the absolute pointing accuracy of the MIPAS instrument (1-1.5 km) which not only drifts with time but increases at high northern latitudes.

6.1 Models, Assumptions and Detection Methods

6.1.1 Colour Index (CI) Method

Colour Indices are the conventionally used method to identify a given spectrum as having cloud present, as described in detail in section 4.1. For example, applying the CI method to a given MIPAS scan pattern will result in a number of high sweeps for which no cloud is detected in the measured radiance spectra; which are interrupted by the detection of a

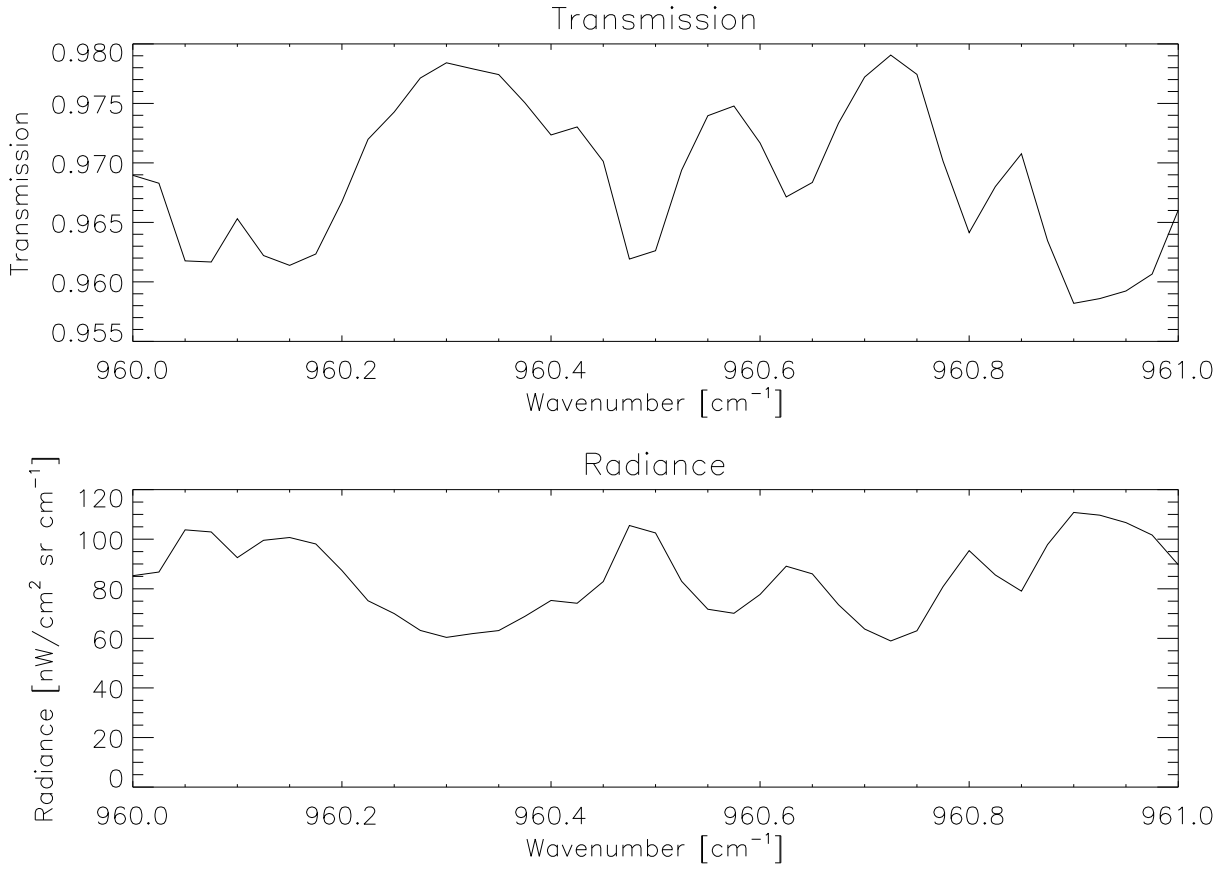

Figure 6.1: Transmission and radiance in the chosen $960 - 961$ cm^{-1} A band microwindow at a tangent height of 9 km.

cloud at a sweep at given tangent height. For typical retrieval purposes, all sweeps below this cloud-contaminated sweep contain no useful information.

6.1.2 Microwindow Selection

For the next three methods presented, the modelling and retrieval is done in a microwindow in the most optically thin part of the A band, such as used in the Simple Threshold Radiance Test. To this end, the microwindow $960 - 961$ cm^{-1} was selected because it is the most transparent part of the spectrum with transmission ≈ 0.95 and has no major absorption/emission lines. Fig. 6.1 shows the transmission and radiance in the microwindow at a tangent height of 9 km.

6.1.3 PACT Method

The **P**lanck **A**pproximation of **C**loud **T**op Height (*PACT*) Method is a very preliminary but very quick way to estimate the C_{top}. In this method, we assume that the cloud can

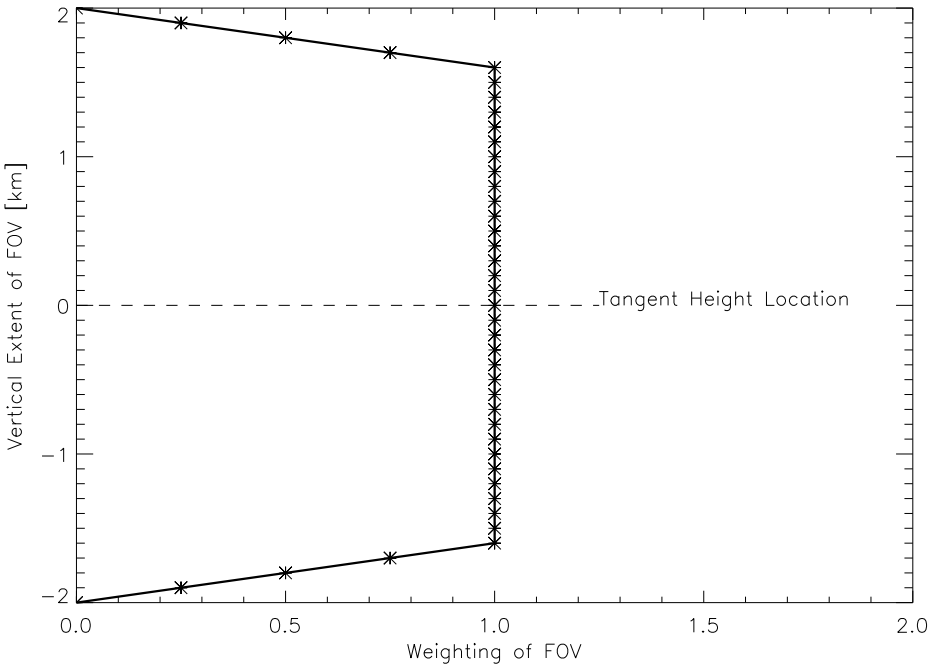

Figure 6.2: The trapezoidal field-of-view (FOV) of the MIPAS instrument. Here the asterisks show the vertical partitioning at every 0.1 km used in the $PACT$ Method.

be modelled as a blackbody. Realistically, clouds are grey or coloured bodies which limit to blackbodies when they are thick, flat and horizontally homogeneous. Furthermore, we assume the radiance contributed by the clear atmosphere is negligible when compared with that emitted by the cloud, and thus forego modelling the clear atmospheric contribution to the radiance spectrum. This assumption is valid because for altitudes at which cloud usually occurs, the atmospheric radiance contribution is typically less than ten percent of the total measured radiance.

A straightforward procedure is followed in the retrieval of the C_{top} by the $PACT$ Method:

1. Identify a cloudy spectrum which has a thick cloud present ($CI < 1.8$) and which also has a very clear sweep directly above ($CI > 4$) by the CI Method.

2. At the tangent height that the CI Method has flagged as thickly cloudy, consider the FOV of MIPAS which has been defined as trapezoidal and the specifics of which are described in Fig. 6.2. Since here we take the FOV to be centred on the tangent height of focus and extending 2 km vertically above and below the tangent height, we partition the FOV vertically (z_i) into 40 height divisions

$$\delta z_i = z_i - z_{i-1}, \tag{6.1}$$

at a resolution of 0.1 km, as shown in Fig. 6.2.

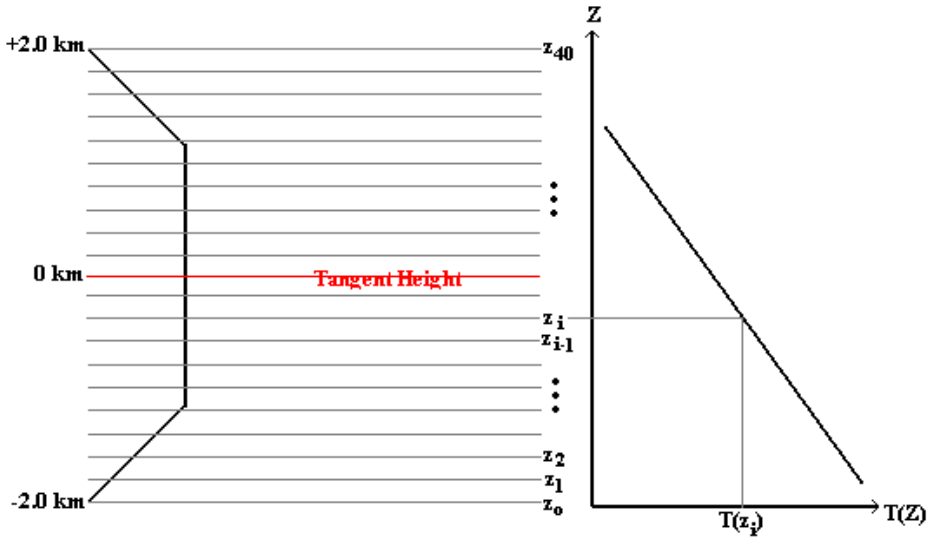

Figure 6.3: Schematic representation of vertical partitioning of the trapezoidal FOV of the MIPAS instrument and of estimation of brightness temperature, where $T(z)$ is the temperature profile.

3. Use the retrieved atmospheric temperature profiles obtained from the corresponding level 2 data to interpolate the temperature at each of these height partitions z_i. Assume that the brightness temperature associated with a cloud top at that height partition equals the atmospheric temperature at the height partition; that is, that

$$T_{Bi} = T(z_i). \tag{6.2}$$

   There is some uncertainty in the retrieved temperature at and below the CI-flagged C_{top} since profiles below this point are smoothly fitted by climatologically gathered profiles. Fig. 6.3 schematically represents the partitioning and estimation of brightness temperature.

4. Calculate the radiance emitted by a blackbody at each vertical partition z_i by evaluating the Planck function B at T_{Bi} in a microwindow in the A band ($960 - 961$ cm^{-1}).

5. Each vertical partition in the FOV z_i is a possible C_{top}. To model the radiance emitted by a cloud in the FOV with a C_{top} located at the vertical partition z_i, integrate the radiance emitted at all z_i below the C_{top} and normalise this within the FOV using the appropriate weighting w_j from the trapezoidal FOV convolution. For a mean radiance $\bar{B}(T_{Bi}, z_i)$ at partition z_i, the total radiance emitted by a cloud having a cloud top height at z_i is thus defined as

$$\bar{L}_{mod}(z_i) = \frac{\sum_{j=0}^{i} \bar{B}(T_{Bi}, z_j) w_j}{\sum_{j=0}^{40} w_j} \tag{6.3}$$

6. Calculate the mean radiance of the measurements in the chosen microwindow, $\bar{L}_{meas}$. Match this value to the mean radiances at each possible C_{top}, $\bar{L}_{mod}(z_i)$. When

$$\bar{L}_{mod}(z_i) \approx \bar{L}_{meas}, \tag{6.4}$$

the C_{top} has been obtained.

6.1.4 RIACT Method

The **R**FM **I**terative **A**pproximation of **C**loud **T**op Height Method is a more trustworthy but slightly more time-consuming way to estimate the C_{top}. In this method, we assume that a thick cloud can be modelled numerically by essentially a bank of aerosol (extinction coefficient $\beta_{ext} = 1.0$ km^{-1}, horizontally homogeneous) starting at the Earth's surface and extending homogeneously upwards to the C_{top} where it stops immediately (in a step-function fashion), as highlighted in Fig. 6.4. While, physically, clouds usually do not start at the surface of the Earth, this approximation is justified since a high extinction coefficient β_{ext} implies that only a short distance into the cloud is seen, and the radiance emitted below the cloud is very much overwhelmed in magnitude by that emitted by the cloud (by a factor of 10). As well, Fig. 6.5 shows that indeed the mean radiance changes very little once the extinction coefficient increases above 0.01 km^{-1}, so choosing $\beta_{ext} = 1$ should enable us to confidently model clouds with a range of extinction coefficients greater than 0.01 km^{-1}.

A straightforward procedure is followed in the retrieval of the C_{top} by the *RIACT* Method:

1. Identify a cloudy spectrum which has a thick cloud present ($CI < 1.8$) and which also has a very clear sweep directly above ($CI > 4$) by the CI Method.

2. At the tangent height that the CI Method has flagged as thickly cloudy, vertically divide the FOV up into 0.25 km-wide sections. Each of these heights represents a possible cloud top height C_{top}.

3. Simulate the radiance emitted in the FOV in the previously used microwindow (960 − 961 cm^{-1}) by modelling cloud as decribed above and running the Reference Forward Model (RFM) at each possible C_{top} iteratively. In the RFM simulations, use a finely sampled height grid with vertical grid spacings of 0.05 km in the range of the tangent height ±3.0 km (important because of the manner in which the RFM interpolates over height) and a highly-sampled FOV convolution of 41 pencil beams (location of sampling within FOV becomes important when one has transient C_{top}s).

4. Compare the root mean square error (RMSE) of each of the iterative RFM runs at each possible C_{top}: the height for which RMSE is minimised is the C_{top}.

6.1.5 JOINT Method

The *JOINT* Method is a hybrid of the *PACT* and *RIACT* Methods. The combination of the two methods gives accurate results whilst doing so in a time-efficient manner. We make the same assumptions as before when modelling the thick cloud.

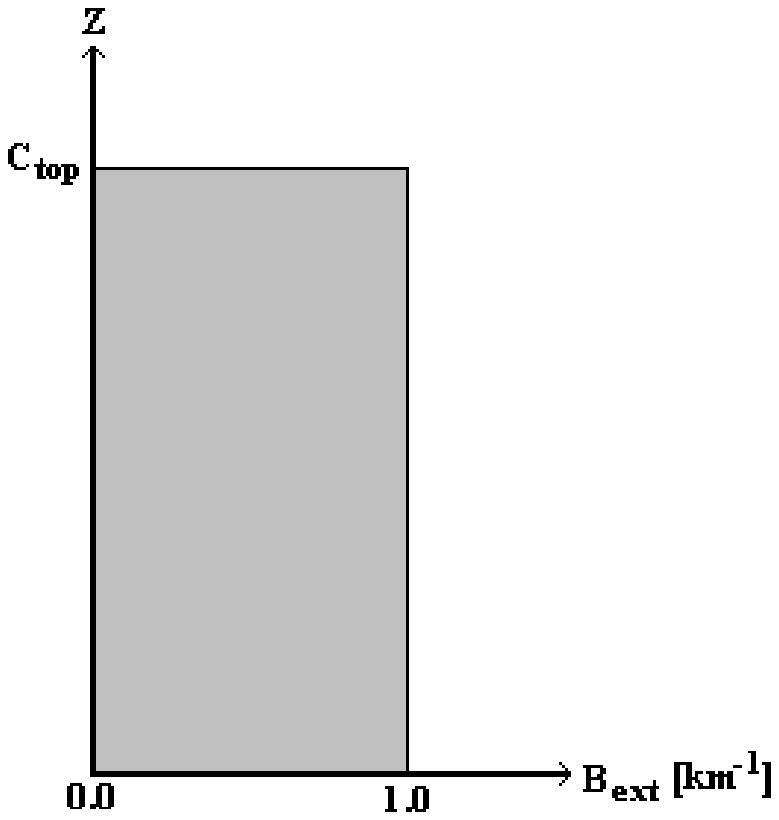

Figure 6.4: Schematic representation of a thick cloud used in the *RIACT* Method.

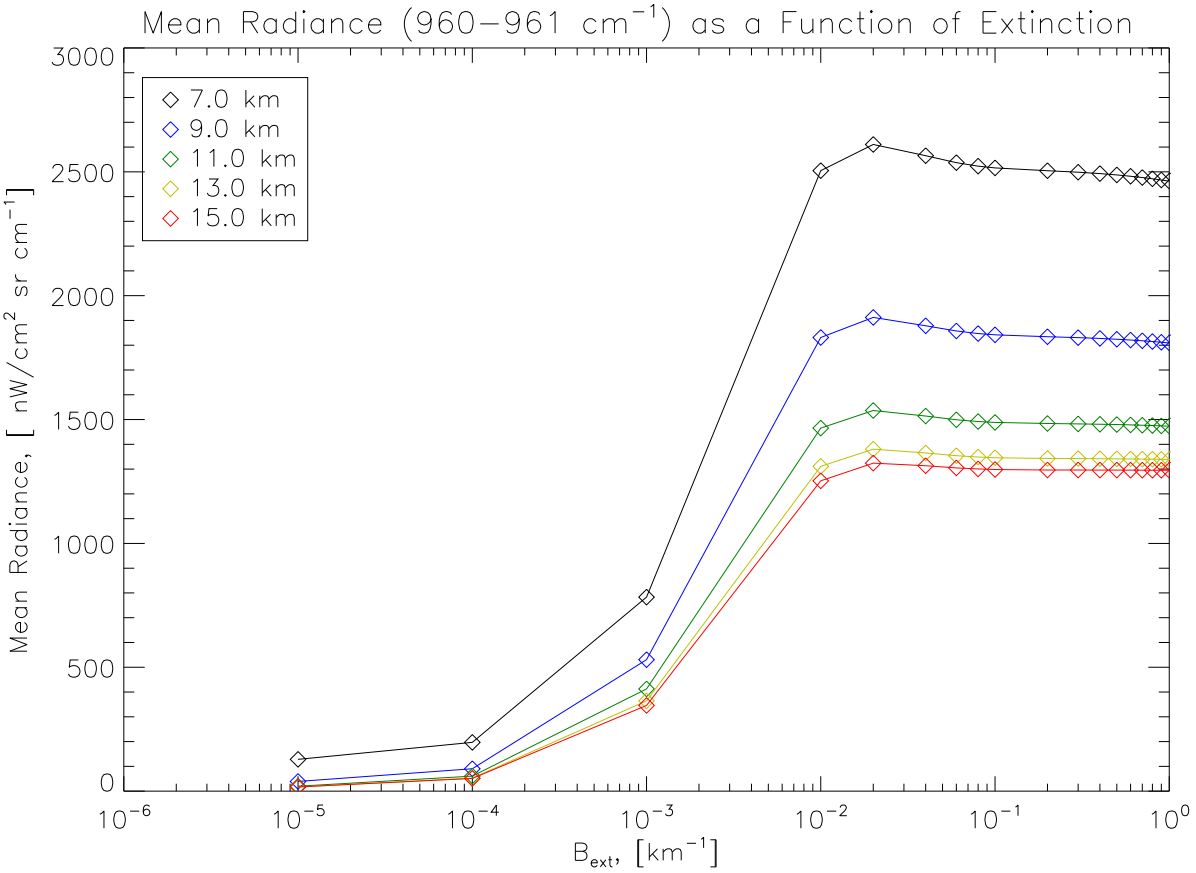

Figure 6.5: Dependence of mean radiance upon extinction coefficient for several different altitudes, as predicted by the RFM. Note that the mean radiance changes very little for $\beta_{ext} > 1$.

The hybridized method:

1. Identify a cloudy spectrum which has a thick cloud present ($CI < 1.8$) and which also has a very clear sweep directly above ($CI > 4$) by the CI Method.
2. Use $PACT$ Method to get a preliminary $C_{top_{PACT}}$.
3. Use $RIACT$ Method in limited altitude range of $C_{top_{PACT}} \pm 0.75$ km to determine the C_{top}.

This hybridization of the two previously discussed methods conserves the reliability of the $RIACT$ Method with the speediness of the $PACT$ Method, since we need now only iterate over approximately one-third of the possible C_{top}s previously considered.

6.2 Case Study

Consider a test case of a sweep identified as thickly cloudy, having a purely clear sweep above it in the scan sequence. Such a case occurs at 17 : 22 : 03 on 4 August 2003 (scan 03), with a clear sweep at 16.09 km and a thickly cloudy sweep directly below at 13.17 km, located at 11.77^o S, 77.26^o E.

6.2.1 PACT Method Results

The temperature profile used to estimate the brightness temperature of the cloud is given in Fig. 6.6. This temperature profile is the corresponding retrieved temperature profile from MIPAS for the spectra used.

Having partitioned the FOV in the manner described in the methodology section, and estimated the approximate brightness temperature for each of the partition heights, the Planck function was evaluated for the $960 - 961$ cm^{-1} microwindow at the appropriate brightness temperature and averaged. The radiance emitted within the FOV was then estimated by discretely integrating over the cloud-filled portion of the FOV. Finally, using the mean measured radiance of ≈ 650 nW/cm^2 sr cm^{-1} in this microwindow, we identified the possible C_{top} that resulted in the same mean emitted radiance. Fig. 6.7 shows the relation between the possible C_{top} as it moves upwards through the FOV and the mean radiance emitted within the FOV, as well as the resulting C_{top} of 12.19 km.

It should be noted that the relation between possible cloud top height and mean black-body radiance as shown in Fig. 6.7 is not one-to-one. This implies that it is most-likely possible to match a given mean radiance with two cloud top heights, because increased height decreases temperature but allows more cloud to be captured in the field-of-view, two processes which counteract each other in a not entirely obvious way. However, since the sweep above which the cloud is first detected is chosen to be completely clear, there should

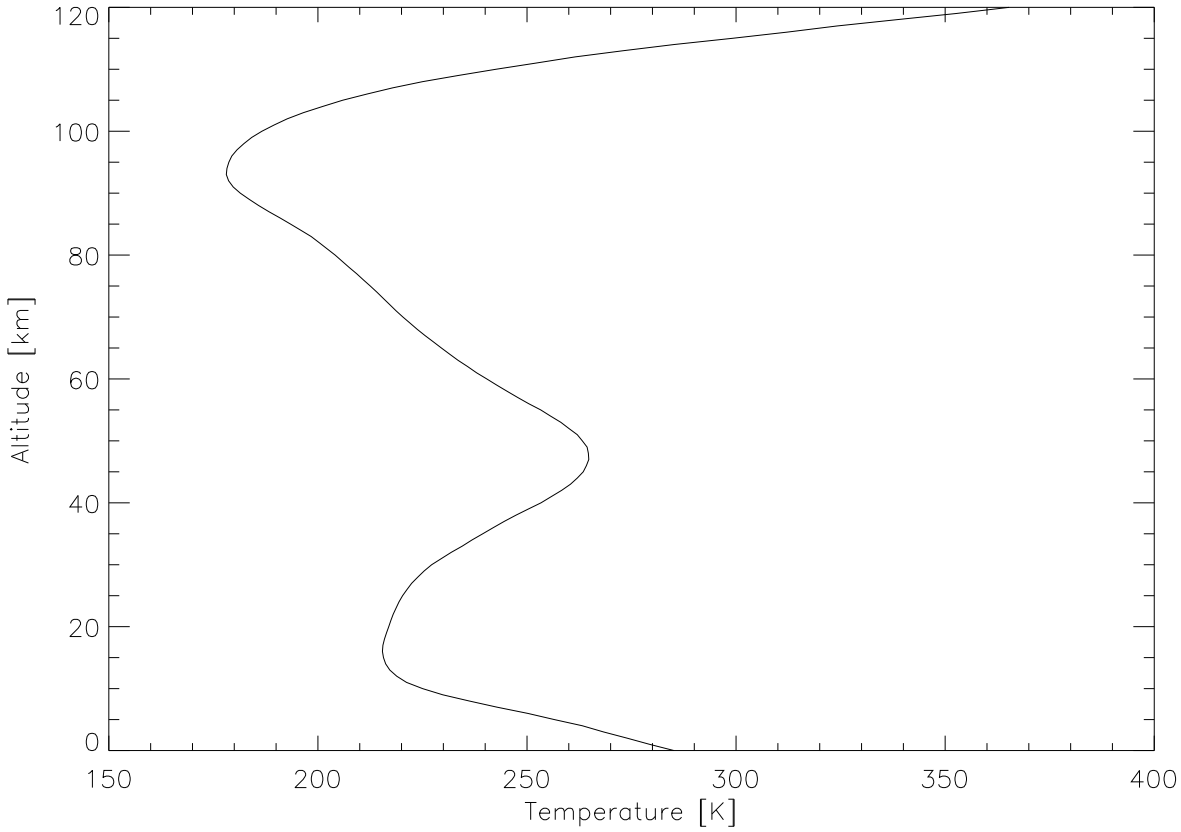

Figure 6.6: Corresponding retrieved temperature profile from MIPAS for case study.

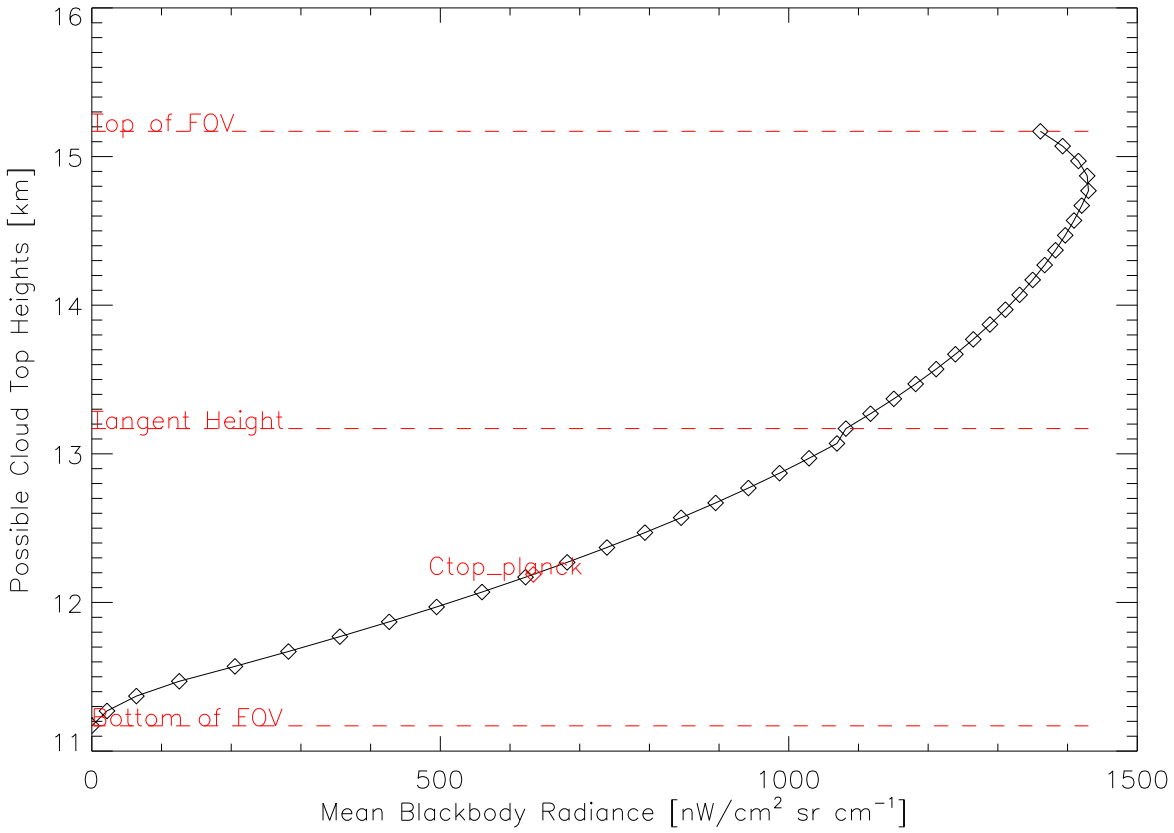

Figure 6.7: Relation between the possible C_{top} as it moves upwards through the FOV and the mean radiance emitted within the FOV for case study. Here, the final C_{top} is overplotted in red.

be no "leakage" of the cloud top beyond the limits of the field-of-view and hence only one cloud top height is retrieved.

6.2.2 RIACT Method Results

Using the *RIACT* Method described previously, a cloud top height was retrieved for the same case study. Iterating over the FOV centred upon the *CI*-flagged cloudy tangent height at 15 possible C_{top}s, the RMSE neatly indicates a fairly sharp minimum, as shown in Fig. 6.8.

Thus, the retrieved C_{top} is 12.42 km, has a RMSE of 146 nW/cm^2 sr cm^{-1} which represents the summation of the error at all 40 measured spectral points in the chosen microwindow, and a mean difference of -18.1 nW/cm^2 sr cm^{-1} with the measured spectrum, which is well within the 50 nW/cm^2 sr cm^{-1} range of noise at the given altitude. Fig. 6.9 shows the measured and modelled radiance spectra of the thick cloud in the chosen microwindow, as well as the difference between the two.

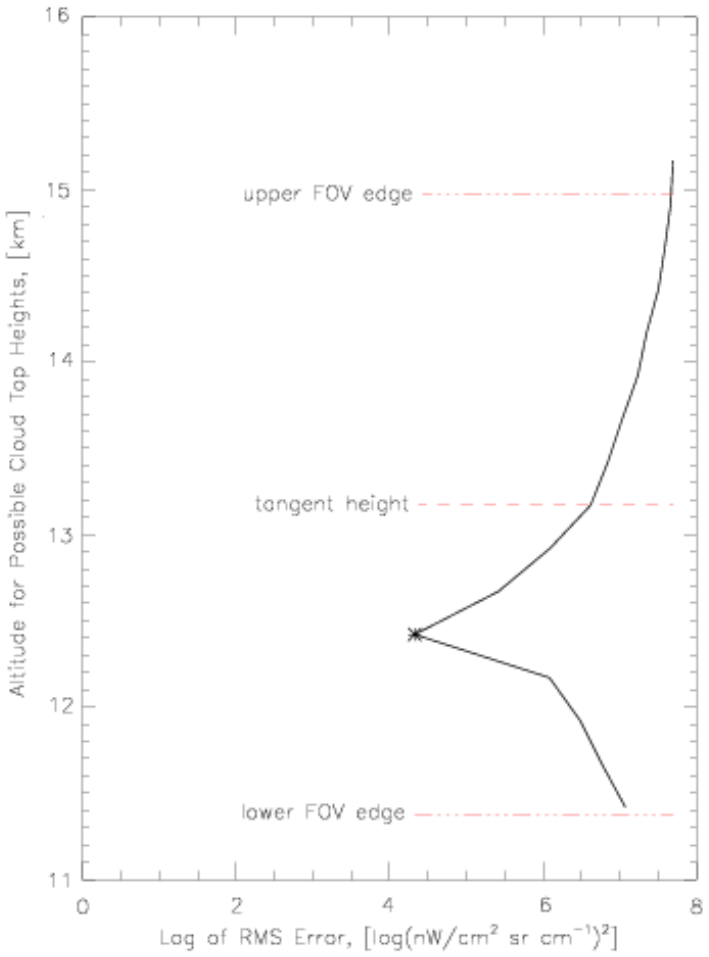

Figure 6.8: Evolution of RMSE in *RIACT* Method. Note the clearly defined minimum in RMSE – the height at which this minimum occurs is said to be the C_{top} and is marked with an asterix.

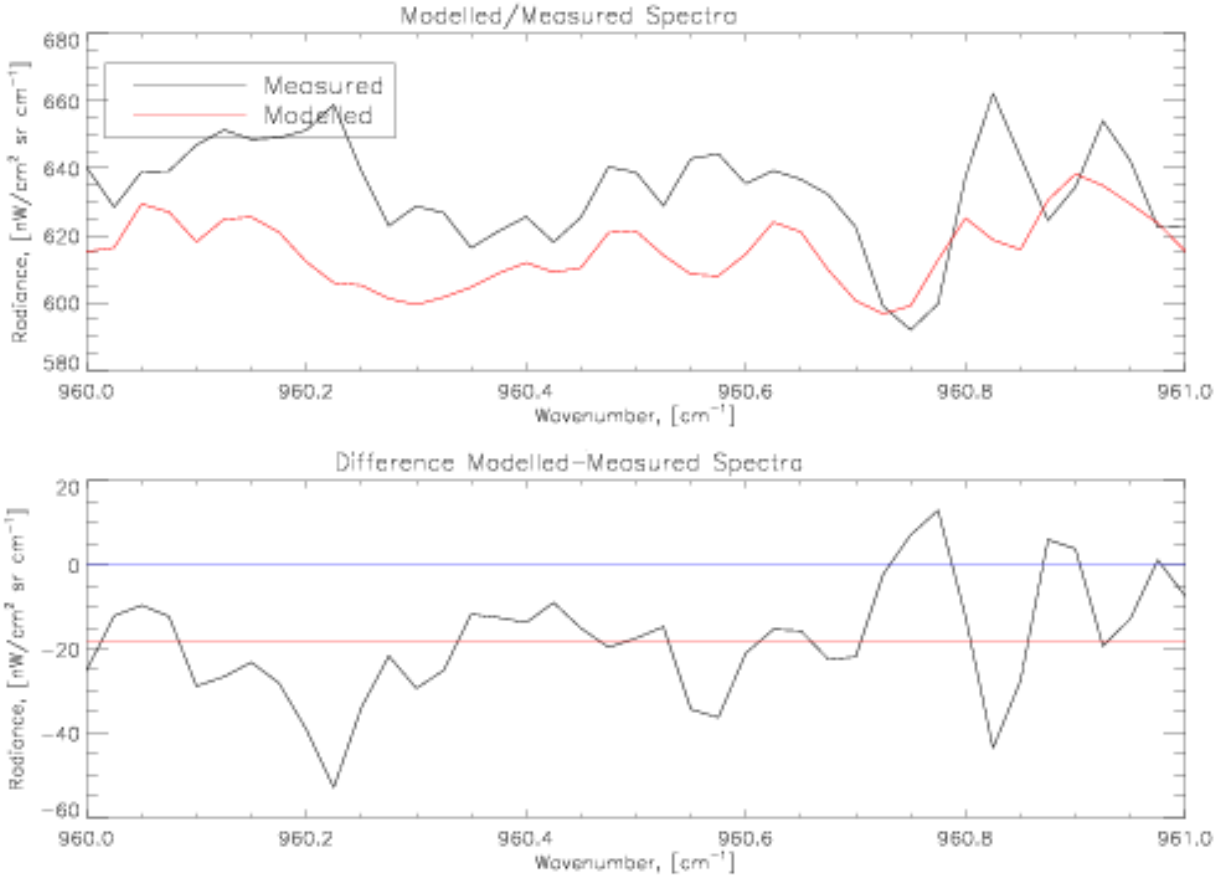

Figure 6.9: The measured and modelled radiance spectra of the thick cloud in the chosen microwindow using RIACT Method, as well as the difference between the two. Here, C_{top} is 12.42 km, and the red line in the bottom plot represents the mean difference between the measured and modelled spectra, having a value of -18.1 nW/cm^2 sr cm^{-1} (cf. noise equivalent radiance is 50 nW/cm^2 sr cm^{-1}).

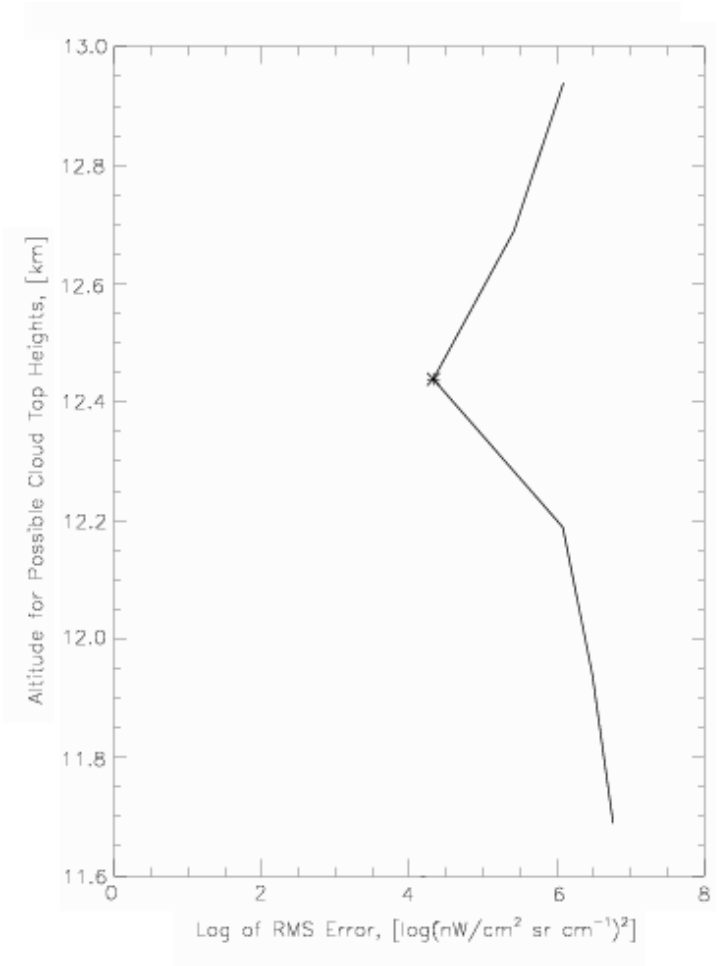

Figure 6.10: Evolution of RMSE in *JOINT* Method. Note the clearly defined minimum in RMSE – the height at which this minimum occurs is said to be the C_{top} and is marked with an asterisk.

6.2.3 JOINT Method

Starting with the C_{top} resulting from the *PACT* Method computations, a limited number of possible C_{top}s were iterated over, resulting in a well-formed minimum in RMSE of 21191 $(\text{nW/cm}^2\ \text{sr}\ \text{cm}^{-1})^2$, and a mean difference of $-18.1\ \text{nW/cm}^2\ \text{sr}\ \text{cm}^{-1}$ at a C_{top} of 12.44 km. The evolution of RMSE is shown in Fig. 6.10 and the measured and thus modelled spectra in Fig. 6.11.

6.2.4 Summary of Methods

When all of the methods are taken together, a validation of sorts is possible. All three methods (PACT, RIACT and JOINT) agree within about 250 m, which indicates that indeed retrieval of C_{top} at a much higher resolution than the existing ± 3.0 km is both scientifically possible and computationally plausible. The results for this test case are summarized in

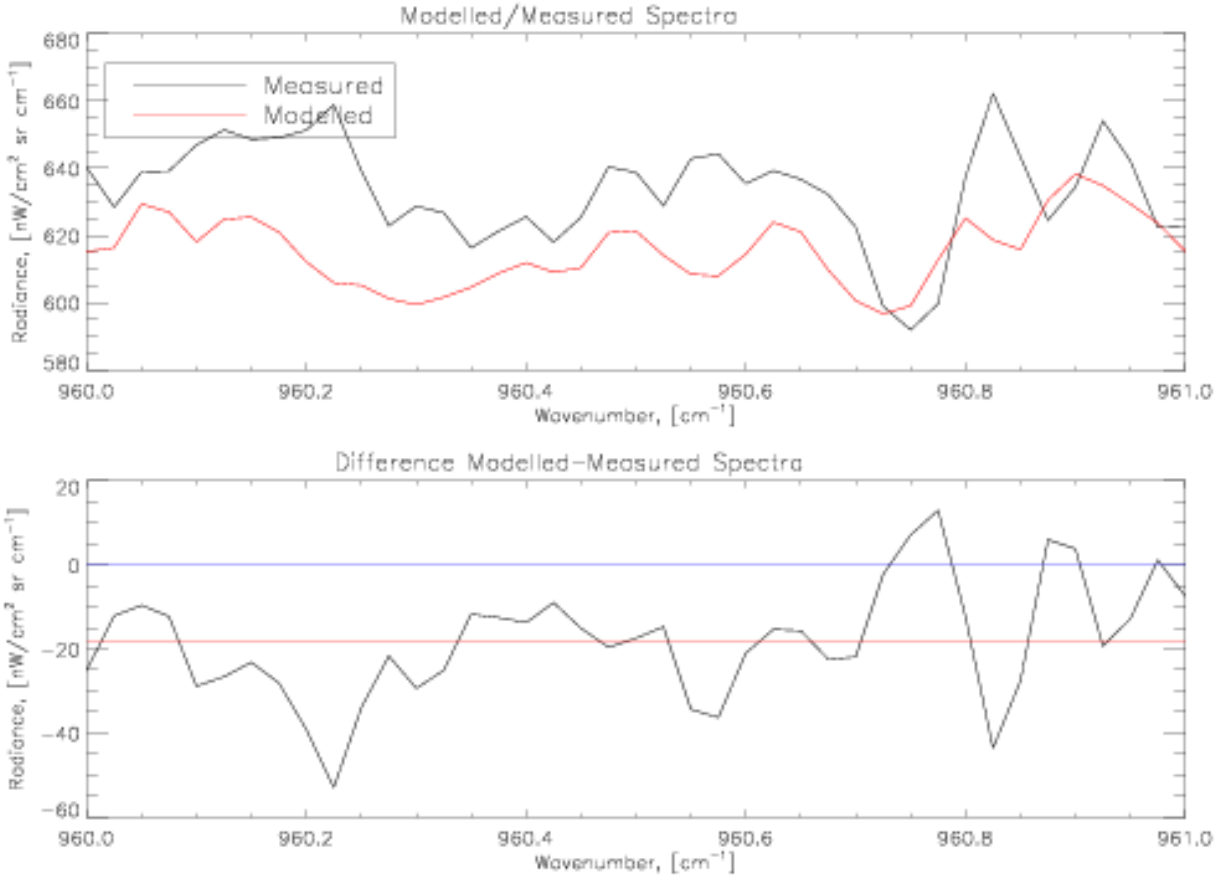

Figure 6.11: The measured and modelled radiance spectra of the thick cloud in the chosen microwindow using JOINT Method, as well as the difference between the two. Here, C_{top} is 12.44 km, and the red line in the bottom plot represents the mean difference between the measured and modelled spectra, having a value of -18.1 nW/cm^2 sr cm^{-1}.

Method	C_{top} *[km]*	*RMSE* $[nW/cm^2\ sr\ cm^{-1}]$	*Mean Difference* $[nW/cm^2\ sr\ cm^{-1}]$
CI	13.17	na	na
$PACT$	12.18	na	na
$RIACT$	12.42	146	-18.1
$JOINT$	12.44	146	-18.1

Table 6.1: Comparison of C_{top} resulting from different methods presented.

Table 6.1.

Furthermore, comparing with EUMetSat's SEVIRI historical images (EUMetSat, 2005), it is clear that there indeed exists thick cloud at the location where the case study has been carried out. Fig. 6.12 shows the EUMetSat SEVIRI infrared image over the Indian Ocean (the secondary, 63^o view of SEVIRI) taken at 18:00 on 4 August 2003.

6.3 Results

These methods for retrieval of C_{top} were then used to analyse the apodised spectra (MIPAS level 1C data) for a period of eight days: from 1 August 2003 to 8 August 2003. The data were first filtered so that only mid-latitude datapoints at sensible altitudes (less than 20 km) were candidates for cloud top height retrieval. This filtering was primarily carried out to minimize the chance of the presence of cloud types other than the thick, flat ones modelled and to take into account that the CI Method used to first detect cloud breaks down at higher altitudes due to increased noise.

The CI Method retrieved many C_{top}s, as shown in Fig. 6.13. For all of these C_{top}s plotted, the sweep has been flagged as thick cloud ($CI < 1.8$) and the sweep directly above has been determined to be totally clear ($CI > 4$).

The $PACT$ Method was applied to this dataset as well and retrieved C_{top}s which were quite similar in magnitude to those computed by the CI Method, as shown in Fig. 6.14.

Finally, the $JOINT$ Method was applied to the week-long dataset, reporting similar C_{top}s as the other two methods, as shown in Fig. 6.15. It is expected that the $JOINT$ Method will give the same result as the $RIACT$ Method, as it did for several cases studied – however the $RIACT$ Method is not applied to this rather large dataset because of computational time constraints.

General comparisons of the methods are presented in Table 6.2 and Fig. 6.16. Fig. 6.16 indicates that, apart from some scatter due probably to noise and clouds which simply are not thick enough to be estimated as a blackbody, the $PACT$ and $JOINT$ Methods give cloud top heights that are quite similar to those indicated by the CI Method, since the slope

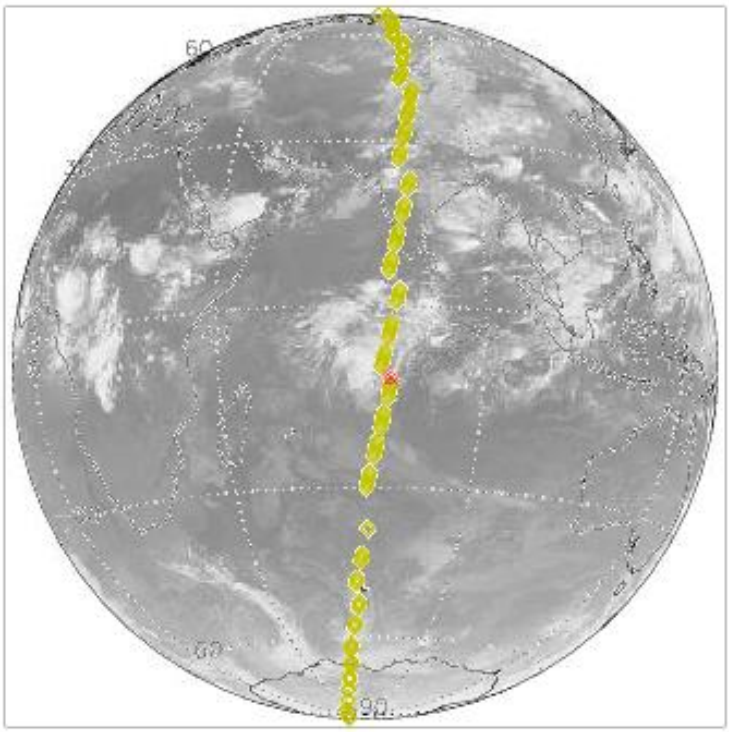

Figure 6.12: EUMetSat SEVIRI infrared image over the Indian Ocean taken at 18:00 on 4 August 2003, with the ENVISAT orbit clearly outlined with the locations of the taken MIPAS spectra shown in yellow and the location of the test case spectrum indicated in red. Clearly there is a thick cloud present in this area. Copyright @ 2005 EUMetSat.(EUMetSat, 2005)

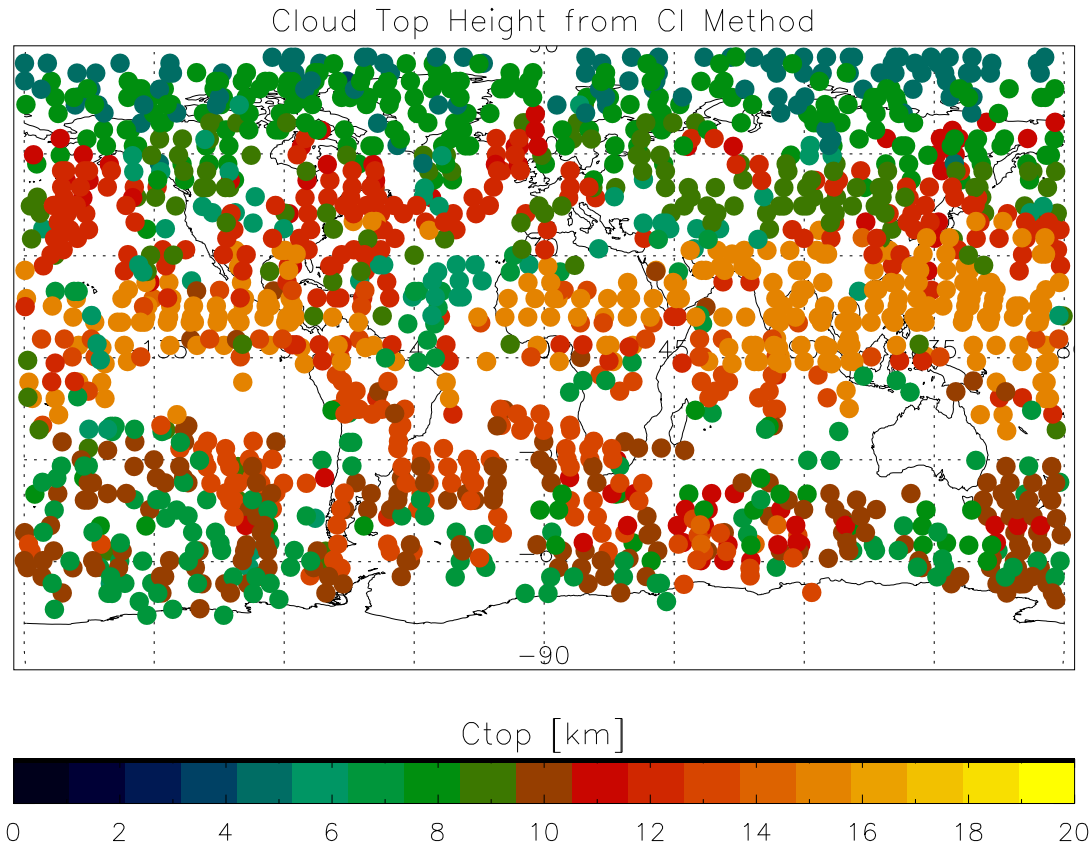

Figure 6.13: C_{top}s reported from 1 August 2003 to 8 August 2003 by the *CI* Method.

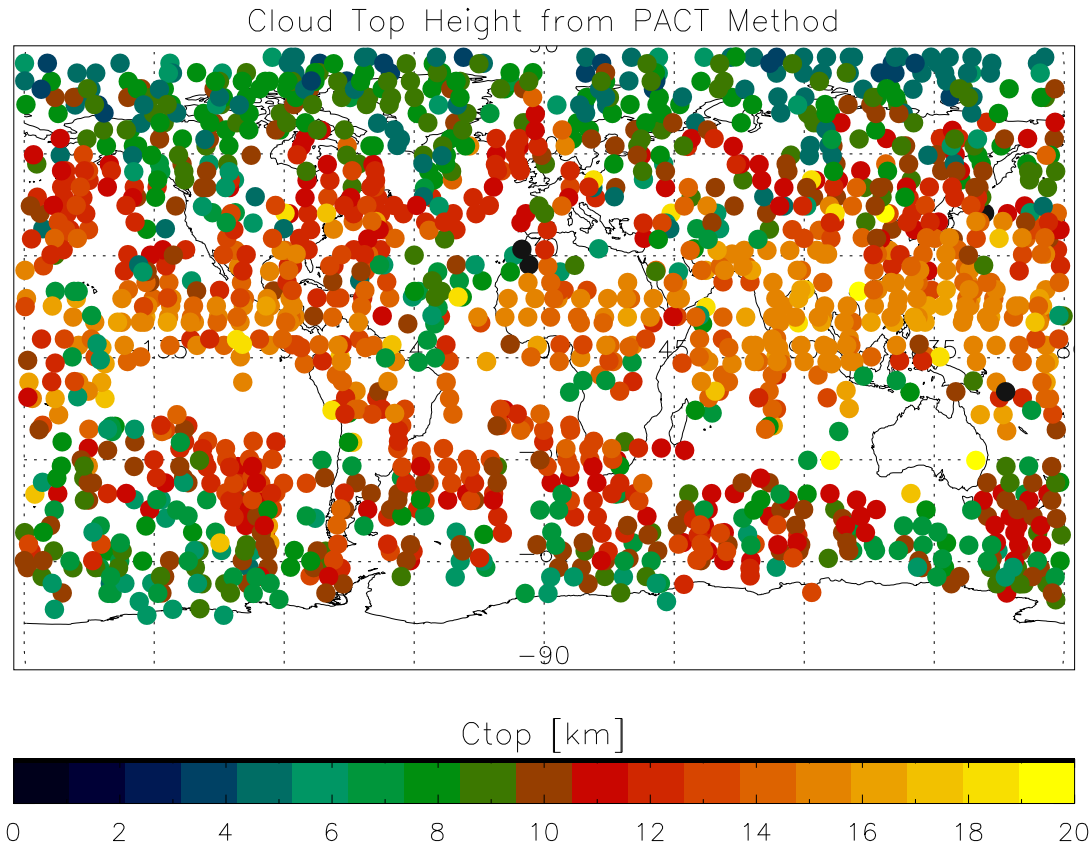

Figure 6.14: C_{top}s reported from 1 August 2003 to 8 August 2003 by the PACT Method.

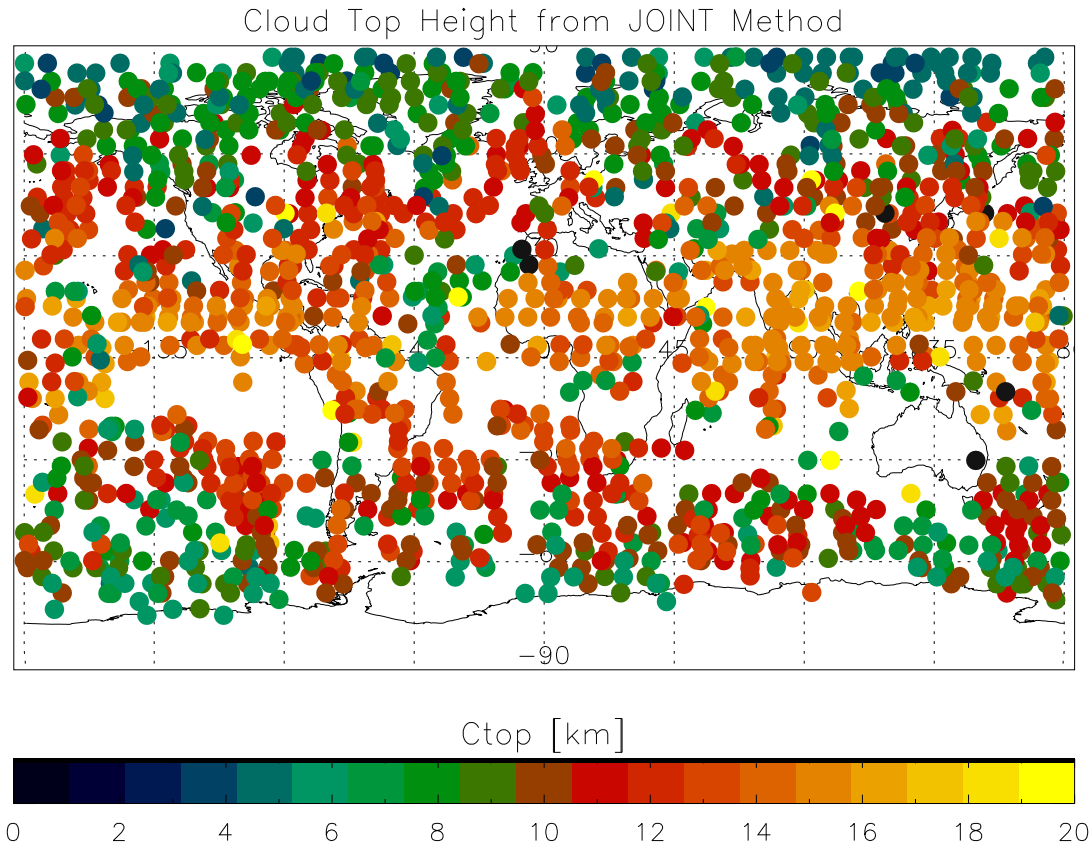

Figure 6.15: C_{top}s reported from 1 August 2003 to 8 August 2003 by the Joint Method.

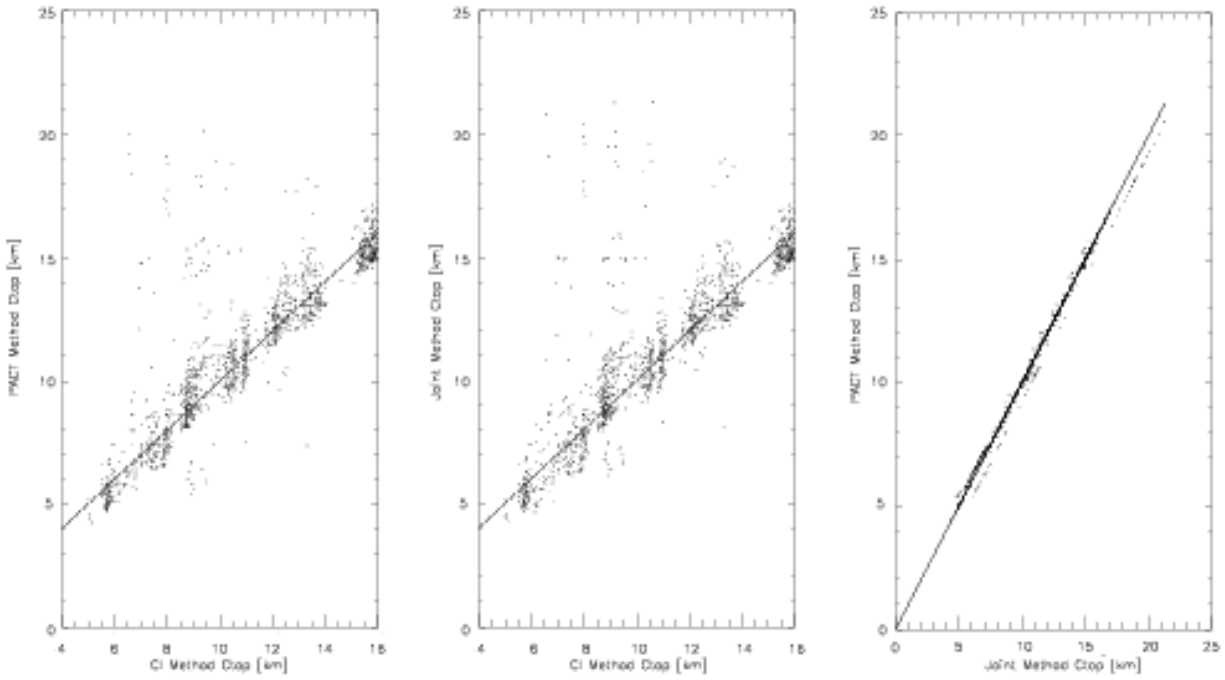

Figure 6.16: Comparison of C_{top}s reported from 1 August 2003 to 8 August 2003 by the CI, $PACT$ and $JOINT$ Methods. All result in cloud top heights which are quite close to each other in magnitude, as confirmed by a slope of nearly unity in the above scatterplots.

of the scatterplot is roughly unity. However, there are some relatively significant differences in the retrieved cloud top height between these methods and the CI Method, while the proposed $PACT$ and $JOINT$ Methods result in cloud top heights that are nearly the same, with nearly negligible scatter. This indicates that the $PACT$ and $JOINT$ Methods give a much improved retrieval of cloud top height, with vertical resolution increased from 3 km to 0.25 km.

6.4 B Band Quality Check

The assumption made with both the PACT and RIACT Methods has been that a cloud in the field-of-view of MIPAS can be treated as a blackbody if it is uniformly filling a certain region of the field-of-view, with a uniform cloud top height extending the whole way through the field-of-view. While this is a fair approximation, obviously it is not the case for many clouds measured. Hence, using a second microwindow in the affected spectrum enables the user to determine whether or not the cloud top height is uniform across the field-of-view (and thus geometrically) or if there are multiple cloud top heights present in the field-of-view.

Latitude Band	*Method*	*Mean C_{top} [km]*	*C_{top} Resolution [km]*
$60 - 90\ N$	CI	7.90	± 3.0
	$PACT$	8.02	± 0.1
	$JOINT$	8.03	± 0.25
$20 - 60\ N$	CI	11.18	± 3.0
	$PACT$	11.82	± 0.1
	$JOINT$	11.85	± 0.25
$20\ S - 20\ N$	CI	13.94	± 3.0
	$PACT$	14.27	± 0.1
	$JOINT$	14.30	± 0.25
$60 - 20\ S$	CI	10.41	± 3.0
	$PACT$	10.80	± 0.1
	$JOINT$	10.81	± 0.25
$90 - 60\ S$	CI	9.59	± 3.0
	$PACT$	8.97	± 0.1
	$JOINT$	8.90	± 0.25

Table 6.2: Comparison of C_{top} resulting from different methods presented in different latitude bands.

6.4.1 B Band Microwindow Selection

In the same manner as the A band microwindow was chosen, a one wavenumber-wide microwindow was chosen (from 1231.0 cm^{-1} to 1232.0 cm^{-1}) in the B band such that the transmission is maximized. However, even the maximized microwindow in the B band has a couple of rather prominent lines, as shown in Fig. 6.17, which will not be able to be modelled by a Planck function. Thus, a filter was fitted over the microwindow which masked out the absorption lines, leaving only the underlying Planck-esque relation.

When the masking procedure has been carried out, the B band microwindow and the A band microwindow both have similar, relatively high transmission over the range of altitudes in which it is expected that clouds will occur, as shown in Fig. 6.18.

For each spectral point measured in the A band, the noise equivalent radiance is 50 nW/cm^2 sr cm^{-1} and this translates into a noise equivalent temperature of 13.8 K for typical cloud top temperatures. In the B band, the noise equivalent radiance is 20 nW/cm^2 sr cm^{-1} per spectral point, which corresponds to a noise equivalent temperature of 25.9 K for typical cloud top temperatures. Since the B band microwindow is nearly twice as noisy as that of the A band, it is not as reliable as the A band microwindow for cloud top height retrieval; however it does provide a reasonable comparison for a validation of sorts, or to provide a quality control monitor.

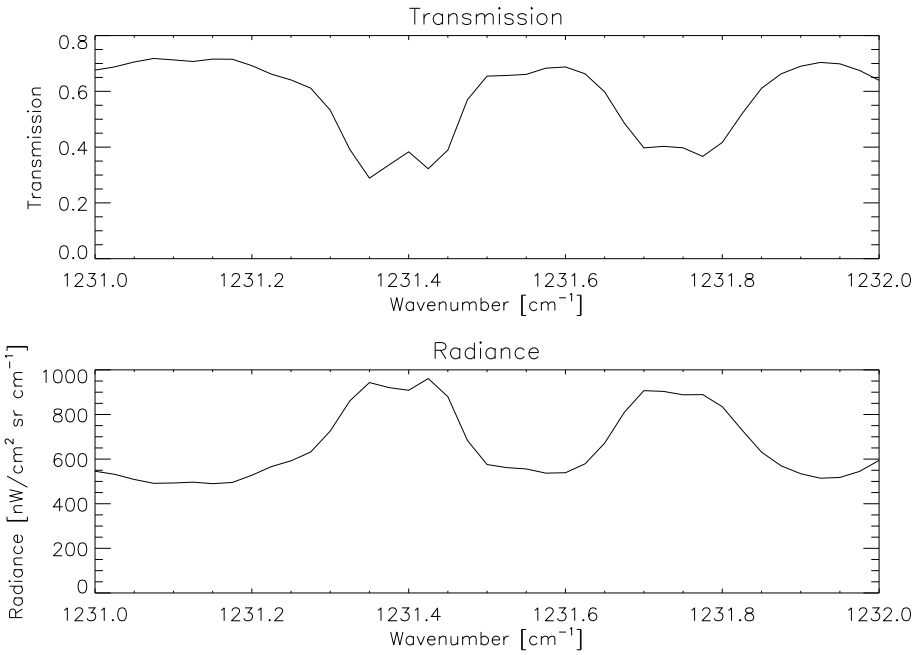

Figure 6.17: Transmission and radiance of the microwindow chosen in the B band at a tangent height of 9 km, from 1231.0 cm^{-1} to 1232.0 cm^{-1}.

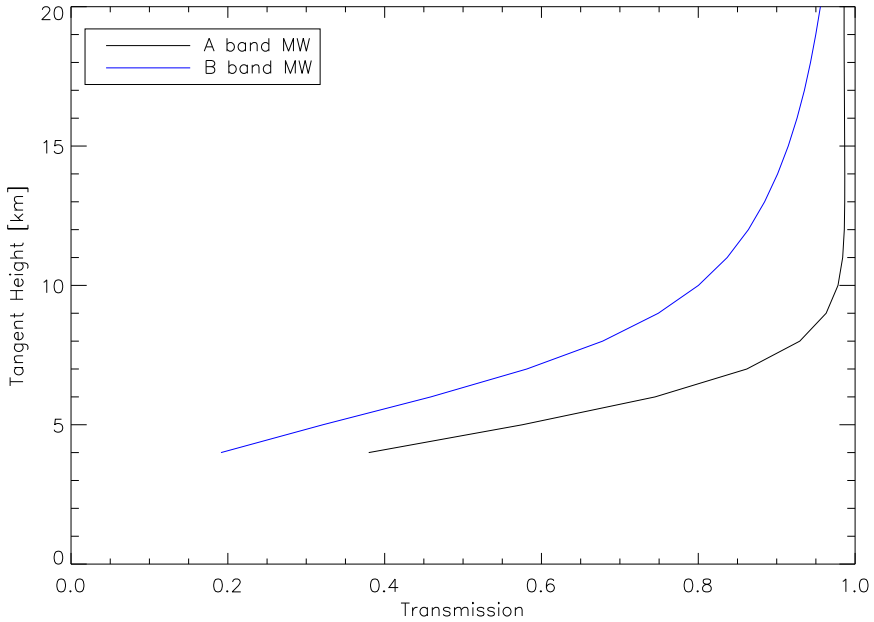

Figure 6.18: Transmission of the microwindows chosen in the A and B bands as a function of tangent height.

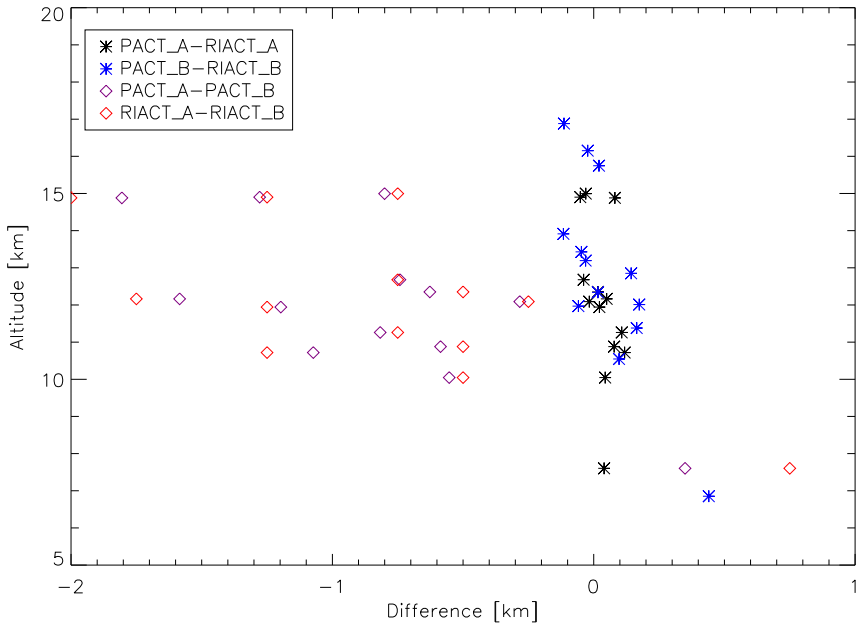

Figure 6.19: Cloud top heights retrieved by PACT and RIACT Methods in the A and B band microwindows.

6.4.2 Comparison of A and B Band Retrievals

An orbit of MIPAS Level 1B data on 1 August 2003 was used to provide statistics for the comparison of the A band and B band microwindows' cloud top height retrievals. As shown in Fig. 6.19, while the cloud tops retrieved by the PACT and RIACT Methods within a band agree with each other (A band PACT with A band RIACT and B band PACT with B) band RIACT, the cloud tops determined by either method do not match closely between bands (A band PACT/RIACT with B band PACT/RIACT), having a mean difference of 0.84 km and a standard deviation of 0.66 km. It was hoped that the two band microwindows would yield cloud top heights within the noise level (which indeed they do, with the noise equivalent height of 1.5 km in the A band and 2.8 km in the B band); however there is quite obviously a systematic trend in cloud top height retrieved, as the B band retrieved cloud top is always higher than that of the A band.

The above test was re-run choosing only fully cloud-filled field-of-views and this time the brightness temperatures were compared directly, as shown in Fig. 6.20. A fully filled field-of-view of an optically thick, homogeneous cloud should have the same brightness temperature calculated for both the A band microwindow and that of the B band. Clearly, there is a proportion ($\approx 20\%$) of points whereby both the A band and the B band register the same brightness temperature; however, there exists a great deal of scatter above the one-to-one line between the two, indicating that the B band brightness temperature is systematically higher.

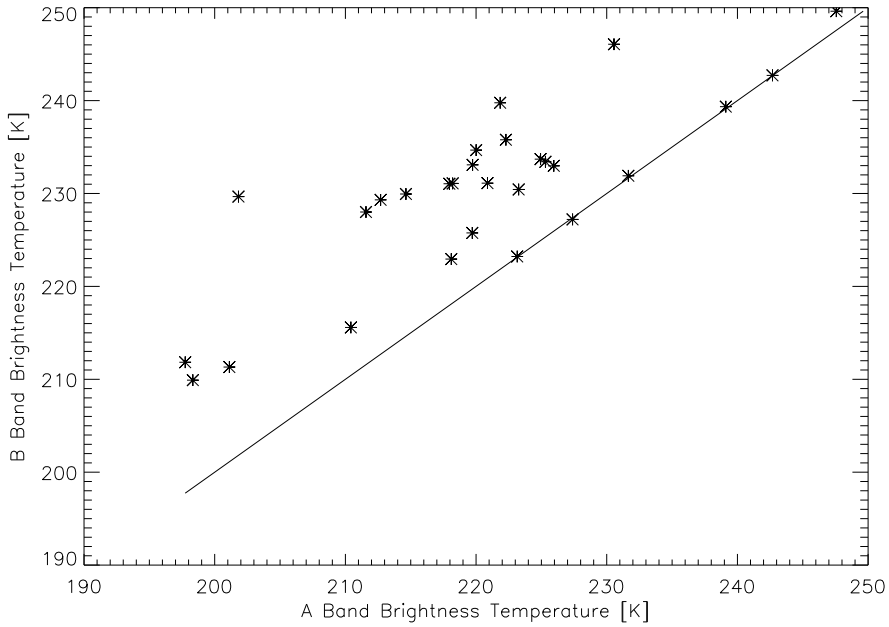

Figure 6.20: Cloud brightness temperatures in the A and B band microwindows for an orbit of MIPAS Level1B data taken on 1 August 2003.

As a test, in both microwindows, the effect of having a non-homogeneous cloud top was investigated. Taking the field-of-view to be completely filled by a cloud which is half at a brightness temperature T_1 and half at a brightness temperature T_2, the Planck function was evaluated at each of these two temperatures and then the results of the two temperatures averaged to get the net radiance in the field-of-view. A corresponding brightness temperature for this net radiance was then estimated (not simply the average of the two constituent brightness temperatures because the Planck function is not linear in temperature). This test was carried out for both the A band microwindow and the B band microwindow and it was found that the brightness temperatures in the B band were systematically higher than those in the A band, as shown in Fig. 6.21. This implies that the scatter in cloud temperature as shown previously in Fig.6.20 is a result of there being a non-homogeneous cloud top through the field-of-view of the instrument and hence there are at least two different brightness temperatures contributing to the overall emerging cloud radiance.

Thus the brightness temperature of the radiance emitted in the B band microwindow can be used as a quality flag of the validity of the cloud top height retrieved in the A band. If the B band brightness temperature equals that of the A band, then there exists a single homogeneous cloud top height and the retrieval is of high quality. However, if the B band brightness temperature is significantly higher than the A band brightness temperature, there exists a non-homogeneous cloud top height within the field-of-view and the retrieval for cloud top height is less precise.

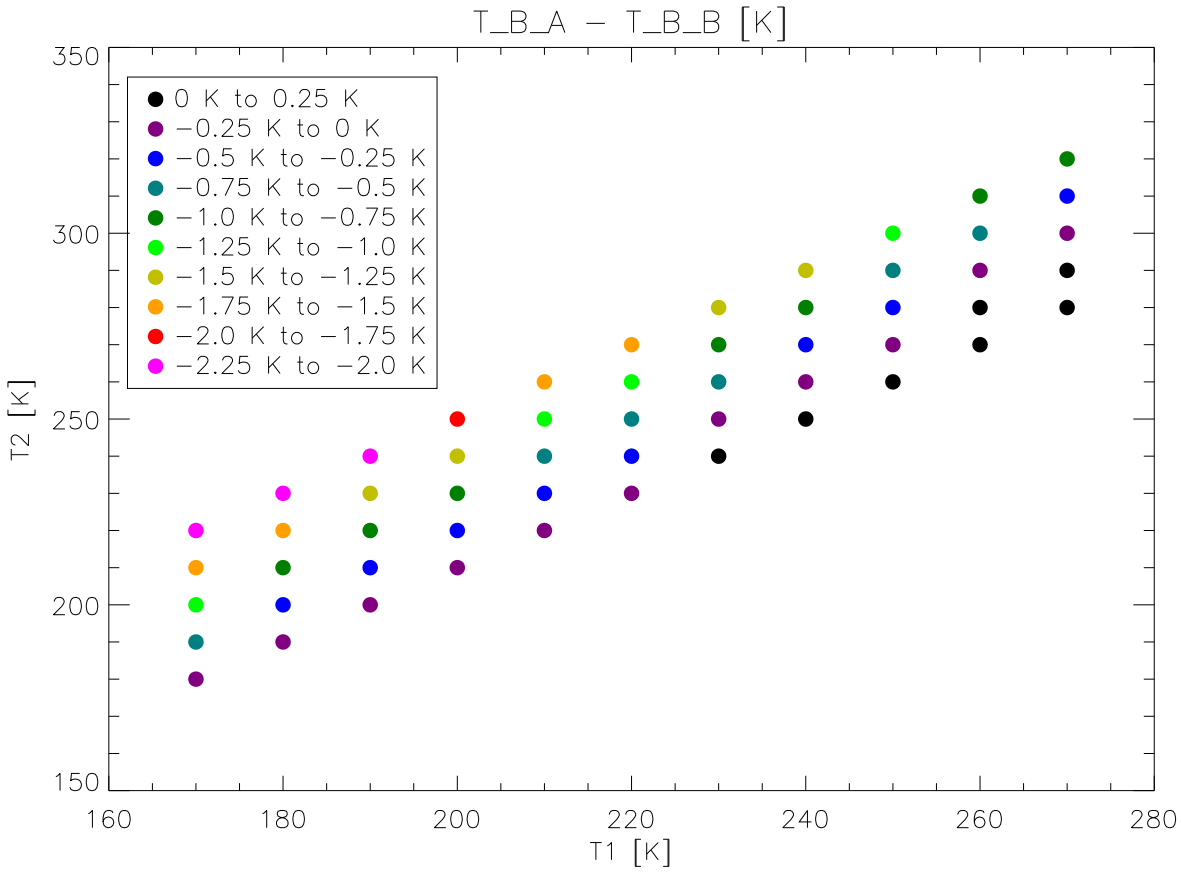

Figure 6.21: The difference between the A band brightness temperature and the B band brightness temperature when a non-homogeneous cloud is simulated. Here the colour of the plotted dot represents the difference between the two. Note that the B band brightness temperature is higher than the A band brightness temperature for the vast majority of the cases considered.

6.5 Conclusions and Further Work

This preliminary study confirms that C_{top} can be successfully retrieved by modelling clouds quite simply in the infrared as thick clouds which can be estimated by blackbodies. By placing either a blackbody in the field-of-view of the MIPAS instrument to represent the cloud (as done in the $PACT$ Method) or by implying that the cloud has the extinction of a blackbody and modelling the gaseous spectra (as done in the $RIACT$ Method) or by doing a hybrid of both methods (as done in the $JOINT$ Method), the C_{top}s reported vary very little, yielding similar results for the dataset studied. Furthemore, a microwindow in the B band can be used as a quality check on the cloud top height retrieval by simple comparison of brightness temperature.

The success of this simple model to retrieve C_{top} suggests that other parameters of interest such as cloud top temperature, extinction coefficient, cloud particle effective radius or cloud particle number density could be retrieved if more degrees of freedom were introduced in the simple retrieval. Further work includes looking at the retrieval of other parameters, namely cloud top temperature to start, and validation with another instrument of equally good or better vertical resolution such as the Atmospheric Chemistry Experiment (ACE) satellite, SEVIRI or AATSR.

Chapter 7

High Cloud Climatology

Climatology studies the frequency of meteorological events instead of precise instances of atmospheric phenomena. It tracks average occurrences over years to millennia as well as changes in long-term weather patterns. In much the same way, a cloud climatology is a database which contains a time series of the geographic distribution of cloud types, their properties and statistics. It thus contains the average properties of clouds that are typically found within specific geographic regions, and the manner in which these properties change with time.

The earliest cloud climatologies were compliled in the early to mid-1900s using subjective observations of ground-based weather observers and were used to help aviators plan safe routes. More recently, there has been a move to using satellite measurements instead of ground-based observations, following the motivation of improving weather and climate prediction by accessing how clouds influence the atmosphere.

Since the exact effect of clouds on the Earth's radiation budget depends upon the microphysical and macrophysical distribution of clouds and their frequency, time-variation and evolution, it is important to have accurate reference climatologies (as described briefly in Section 4.1) to determine their relative effect on the Earth. High accuracy and a high degree of global coverage are important, since "significant cloud feedbacks can result from changes in global mean cloudiness as small as 1% per decade, or regional change of 1% per year". (Ewen, 2005)

To this end, the Colour Index cloud detection method combined with the cloud top height retrieval method PACT have been used to analyse a year's worth of data (January through December 2003) to determine the mean cloud top height of high level clouds and to estimate their relative frequency of occurrence. Relative frequency of occurrence is defined to be the percentage of all measurements taken which are said to be contaminated by high level clouds. A large, but unknown, proportion of the high level clouds measured are cirrus. Previous results imply that cirrus clouds permanently cover about 30% of the Earth.

7.1 Methods Used and Products Sought

Although of the four cloud top height retrieval methods discussed in Section 6.1 the RIACT method is the most trustworthy, it is also by far the most expensive in terms of computational time. However, the comparison of the methods carried out in Section 6.3 indicates that, for the most part, the PACT method chooses the same cloud top height as does the RIACT method, and when these two values are not identical, the two are within 250 m of each other. With expediency in mind, then, the PACT method has been applied to a year's worth of MIPAS level 1B data, sampled one day in every ten.

Once a cloud has been detected and its cloud top height determined by the PACT method, the interpolated temperature at the calculated cloud top height is used as a threshold for cloud type filtering. If the cloud top temperature is less than $-15°C$, the cloud is said to be an ice cloud. Since the MIPAS profile effectively scans downwards, it is the highest cloud layer which is detected. Over most of the Earth (exceptions occur for polar stratospheric clouds and cirronimbus towers which can extend into the stratosphere), the highest cloud type possible in the troposphere is cirrus – and so if this highest cloud layer is ice, one can confidently be assured that it is cirrus (in fact, 98% of the clouds detected (ie. $\frac{8342}{8486}$) were indeed ice clouds and taken to be cirrus because of the altitude range). In such a manner, the mean cloud top height and frequency of occurrence of high level cloud (and hence as rough estimate, of cirrus) can be determined.

7.2 Mean High Cloud Top Height

A plot of global mean cloud top height is shown in Fig. 7.1, giving both the seasonal distributions of the mean cloud top height and the annual average. As expected, the average cloud top height increases towards the equator, with increasing tropopause height in the tropics. There is a "hot spot" of high clouds over Indonesia, due to the Intertropical Convergence Zone (Hahn, 2006). Minnus and Harrison (1984) indicate that high clouds occur most frequently over the southern Andes during the afternoon and are most common in the adjacent lowlands during the night, indicating a diurnally-varying mountain-plain circulation; and indeed a peak in cloud top height is noted over the southern Andes in this analysis. These clouds are formed due to orthographic lift over the southern Andes which face prevailing westerly winds off the Pacific Ocean. The North American cloud cover shows little seasonal change, agreeing with GOES/UAS analysis (Menzel et al., 1992), and while there does appear to be heightened cloud cover over the Rocky Mountains relative to the rest of the surrounding region, it is not a region which is characterised as having globally high cloud top heights. In much the same manner, the Himalayan area does not show much high cloud on the global scale; however the highest cloud in the Asian continental region does occur over the Himalayas (Wylie, 1994). The Congo and the Amazon Basin are also reported to have high cloud present (Wylie, 1994), as observed in this analysis.

For comparative purposes, Fig. 7.2 shows the cloud top pressure fields from ISCCP analysis. The dark blue areas represent high clouds and agree qualitatively with our analysis.

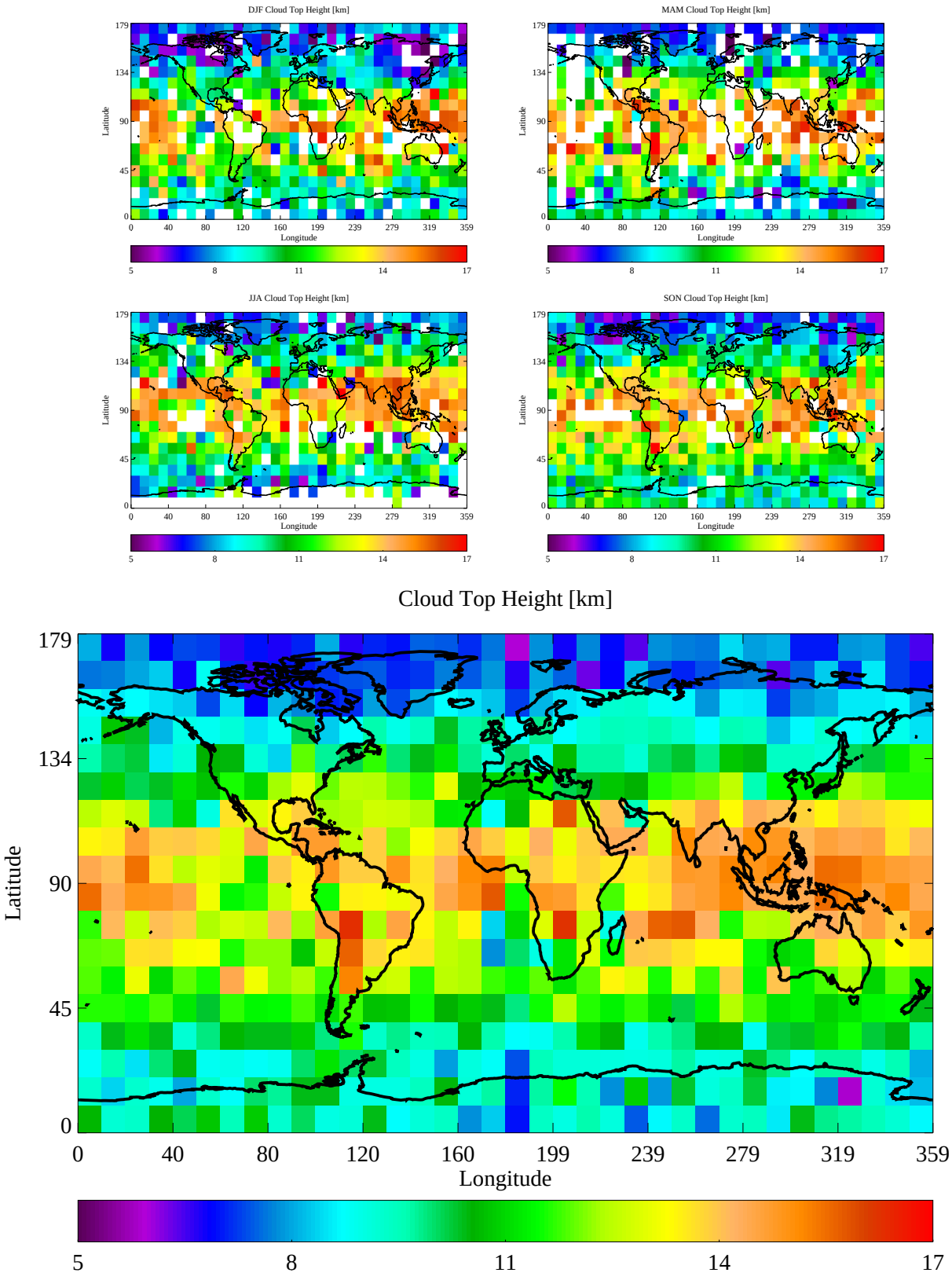

Figure 7.1: Mean cloud top height for each of the four seasons, given by DJF (December, January, February), MAM (March, April, May), JJA (June, July, August) and SON (September, October, November) as well as the annual average.

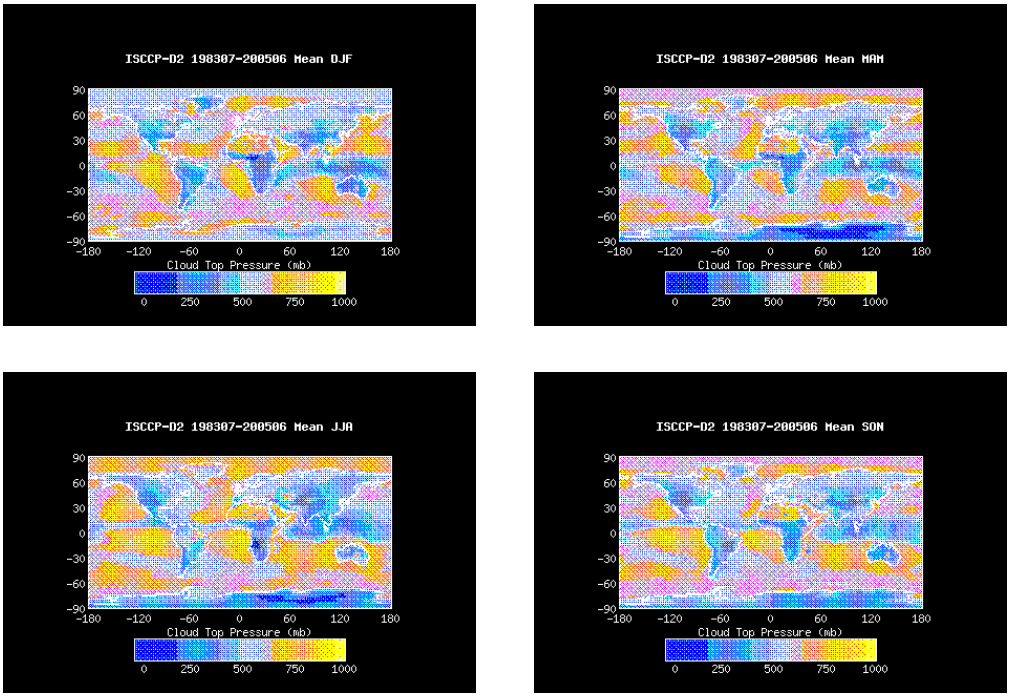

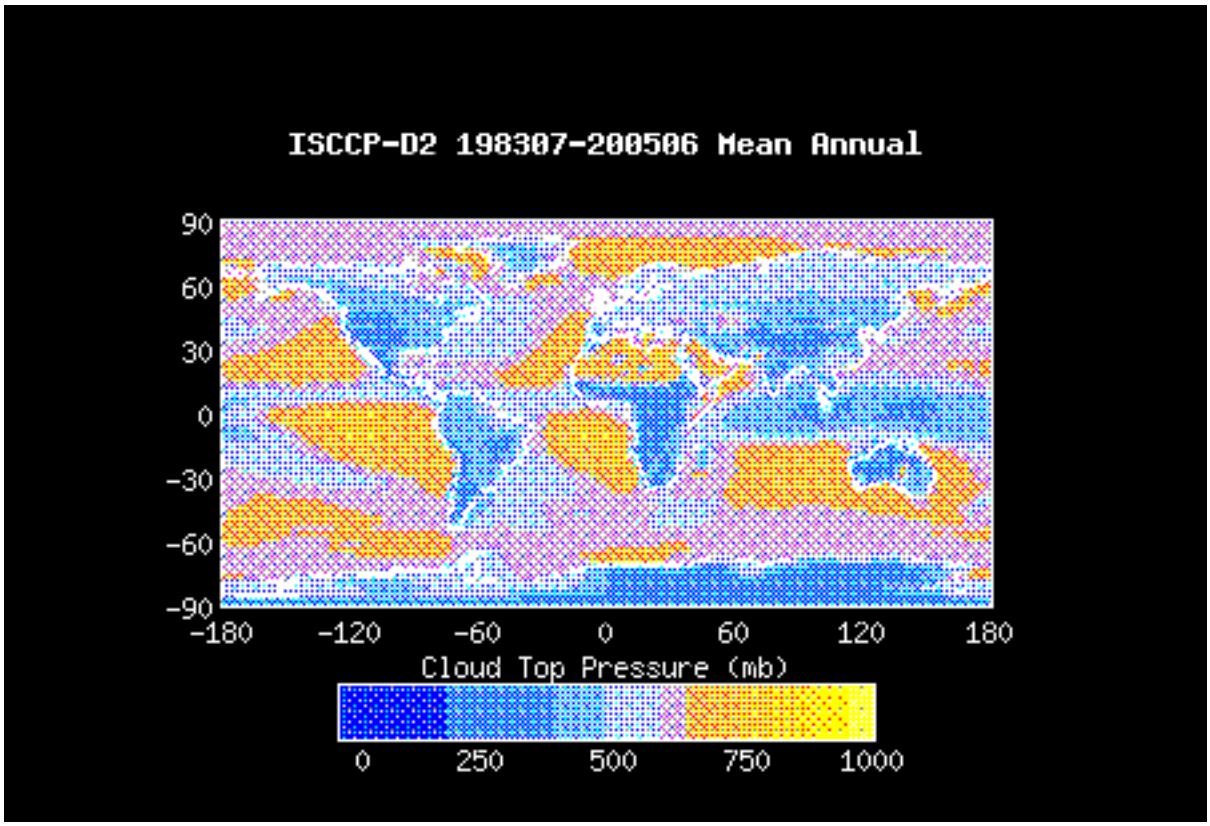

Figure 7.2: Mean ISCCP cloud top pressure for each of the four seasons, given by DJF (December, January, February), MAM (March, April, May), JJA (June, July, August) and SON (September, October, November) as well as the annual average.

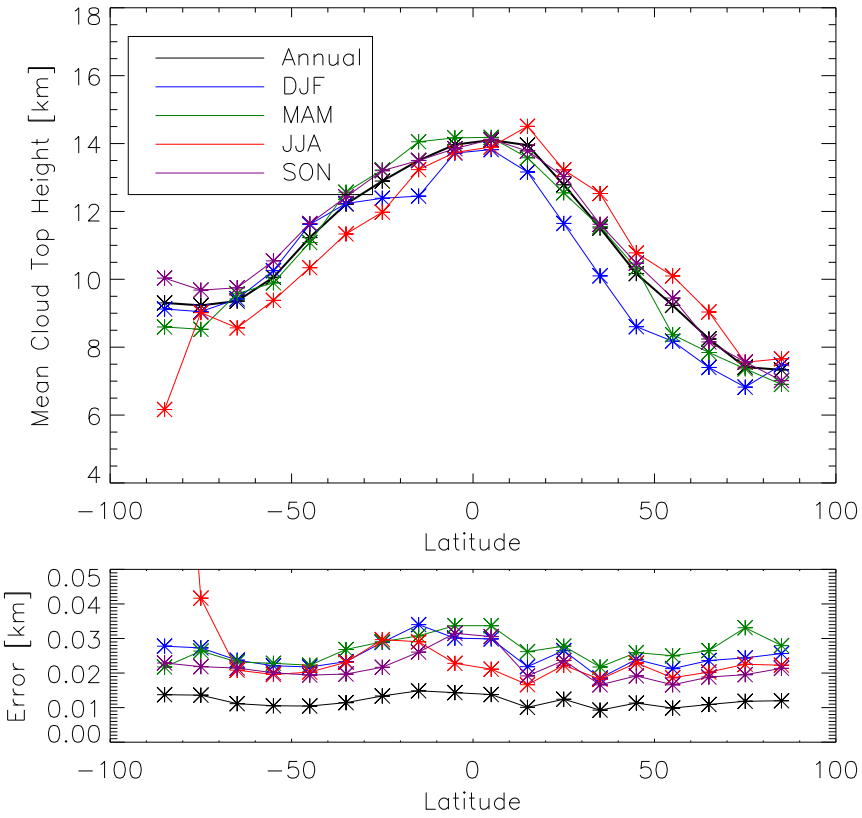

Figure 7.3: Mean cloud top height averaged zonally for each of the four seasons, given by DJF (December, January, February), MAM (March, April, May), JJA (June, July, August) and SON (September, October, November) as well as the annual average. The corresponding error in mean cloud top height is plotted for each in the lower plot.

Viewing these mean cloud top heights as zonally averaged values as shown in Fig. 7.3, the effect of season becomes more explicit, as shown in the shift in the Intertropical Convergence Zone in correspondence to the sun. The summer hemisphere appears to have higher clouds than does the winter hemisphere (Hahn, 2006). Again, as expected, the maximum in cloud top height occurs at the equator.

Finally, Fig. 7.4 shows the time series of the mean cloud top height for the year-long study period. Over the study period, the global mean cloud top height varies in altitude between 10 km and 12 km, values well in keeping with the accepted range of cirrus altitudes. Tropical cirrus has an average cloud top height of 13.75 km, while mid-latitudinal cirrus is found between 9 km and 12.5 km. Polar cirrus is reported as having the lowest cloud top height, occuring between 7 km and 10 km. Again, the seasonal variation due to the sun-shifting Intertropical Convergence Zone is easily seen, since the highest mid-latitudinal cloud top heights occur during the respective summers for the two hemispheres (ie. northern

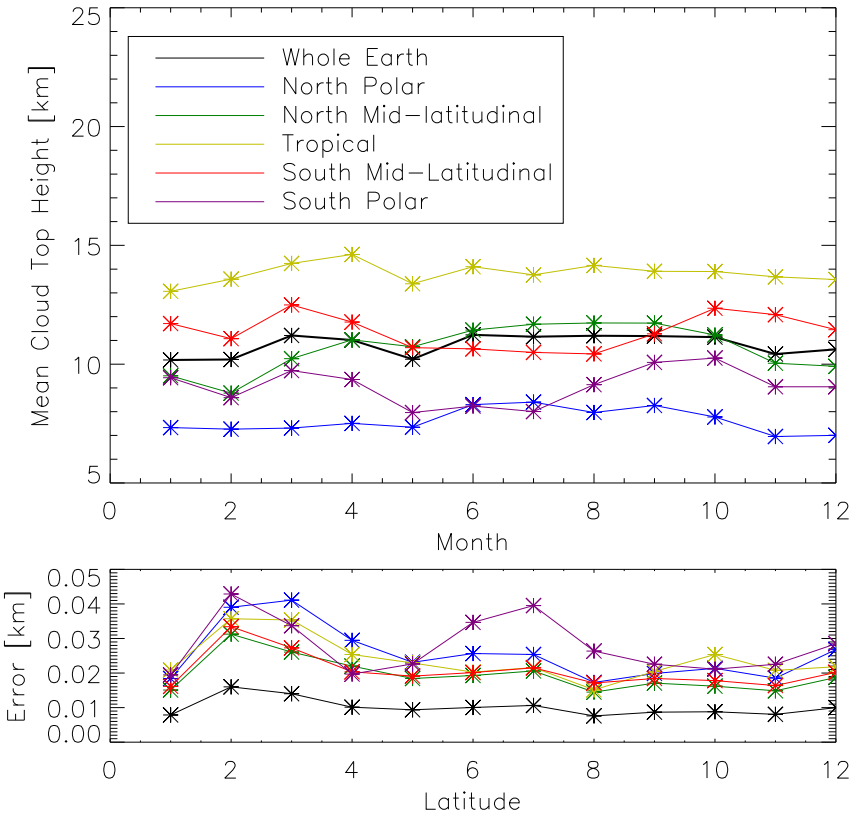

Figure 7.4: Time series of mean cloud top height, given by latitude bins (north polar, north mid-latitudinal, tropics, south mid-latitudinal, south polar) and as a global average. The corresponding error in mean cloud top height is plotted for each in the lower plot.

mid-latitudes have highest cirrus cloud top heights during June, July and August while the southern mid-latitudes do during December, January, February and March).

7.2.1 Day-Night Differences

Because of the some of the mechanisms responsible for cirrus formation (namely convection), it is expected that there should be a day/night difference in the formation and occurrence of the cloud. Generally, it would be expected that there would be more high cloud in regions characterized by considerable convection, such as over the Indonesian Toga core, as discussed previously. Fig. 7.5 shows the mean cloud top height for each of the four seasons, as well as the annual average, filtered into day and night cases.

Clearly, there are three regions of interest where there are significant differences between the day- and night- time observations: over the Southern Andes, over Indonesia and over South-Eastern Africa. In general, there appears to be a higher occurrence of high cloud in the daytime as opposed to the nighttime.

- **Southern Andes**: There appears to be an predominance of high cloud in the daytime but little of this high cloud presence at night. This is well in keeping with the results of Minnus and Harrison (1984), who noted a diurnal variation in circulation ove rthe Southern Andes.

- **Indonesia**: In the daytime, there is a large and well-defined region of high cloud, however this region subsides at night, having much less high cloud present. This behaviour is well-represented and discussed in Hahn (2006).

- **South-Eastern Africa**: There is high cloud which seems to form preferentially at night in this region. Cold, upwelling seawater just off the coast cools the maritime air, limiting its ability to hold moisture and the prevailing easterly winds sweep this cooling effect inwards on the continent, forming clouds. Coastal fogs are created but little rain. The predominance of high cloud, then, at night makes sense as the continent cools more rapidly at nightfall than the neighbouring ocean, these prevailing winds will cause even more cloud formation in the region.

7.3 High Level Cloud Frequency of Occurrence

Frequency of occurrence is probably the most fundamental statistical measure in cloud climatologies. It quite simply reflects the fraction of the time that cloud is present in a given region.

A plot of global high level cloud frequency of occurrence is shown in Fig. 7.6, highlighting both the seasonal distributions of the frequency of occurrence and the annual average. As expected, there is quite a latitudinal dependence upon the frequency of occurrence of high level clouds. As well, comparing with results from Wylie (1994), one can clearly see the relatively cloud-free regions in the eastern Pacific off South America and in the eastern Atlantic off Africa. It is also interesting to note that there is some seasonal variation observable, for instance, around the south pole. There are practically no clouds reported to occur in the south polar region in the south polar winter (June, July, August) but with the return of sunlight in the south polar spring (September, October, November), there are many clouds detected. Given the geographic location and time frame involved, these clouds are undoubtedly Polar Stratospheric Clouds (PSCs) and not cirrus.

Looking at these frequencies as zonally-averaged values, as shown in Fig. 7.7, there is a clear latitudinal dependence. As noted in Woodbury and McCormick (1983), cirrus are most prevalent in the mid-latitudes and tropics, and the frequency of occurrence shows distinct minima located at 20°-30° on each side of the equator, giving the latitudinal distribution a lower-case cursive "m" shape. These maxima reach as high as 60% while the minima as low as 15%, as confirmed by Woodbury and McCormick (1983). At the interface of the tropical and mid-latitudinal tropopause, Reiter (1975) shows the existence of stratospheric-tropospheric exchange processes which result in a downward mass flow of air in those regions throughout the course of the year. Descending air parcels warm throughout their descent,

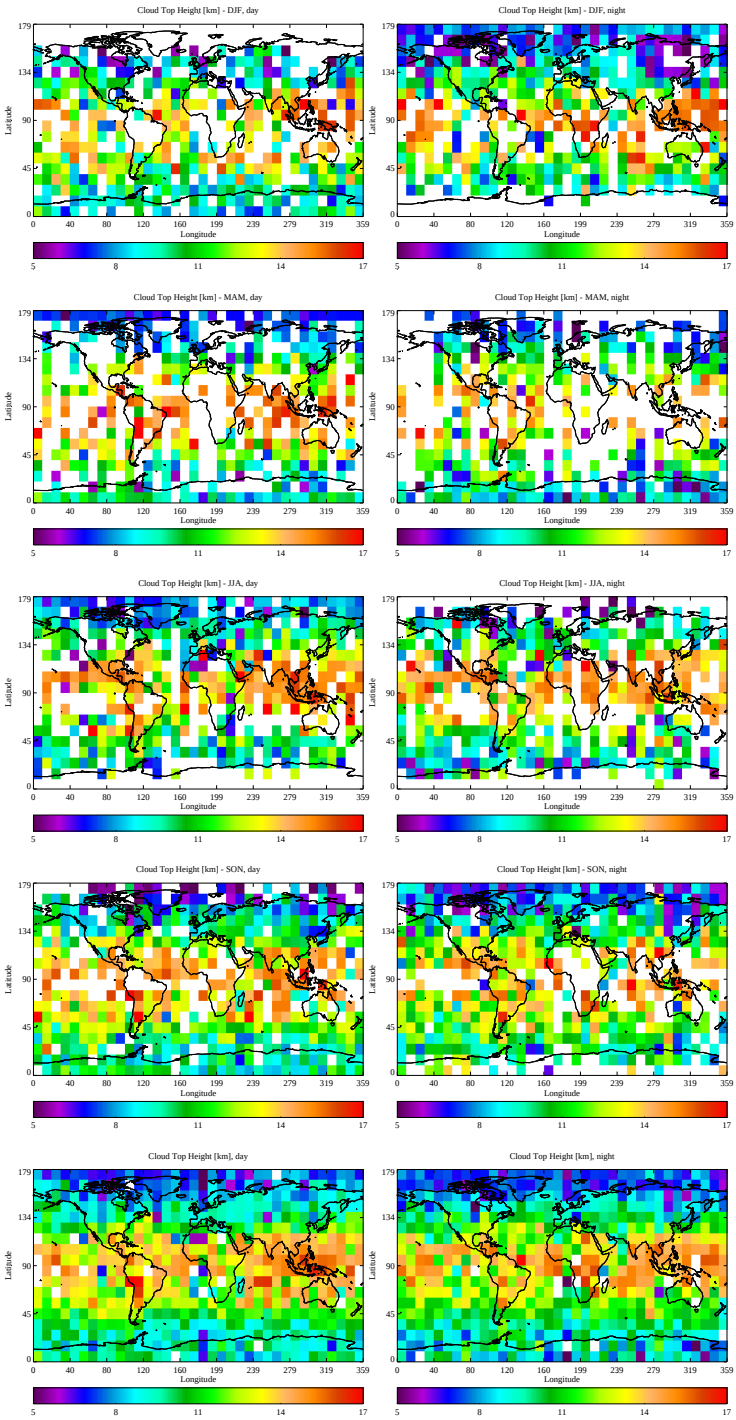

Figure 7.5: Mean cloud top height for each of the four seasons, given by DJF (December, January, February), MAM (March, April, May), JJA (June, July, August) and SON (September, October, November) as well as the annual average filtered into day and night cases.

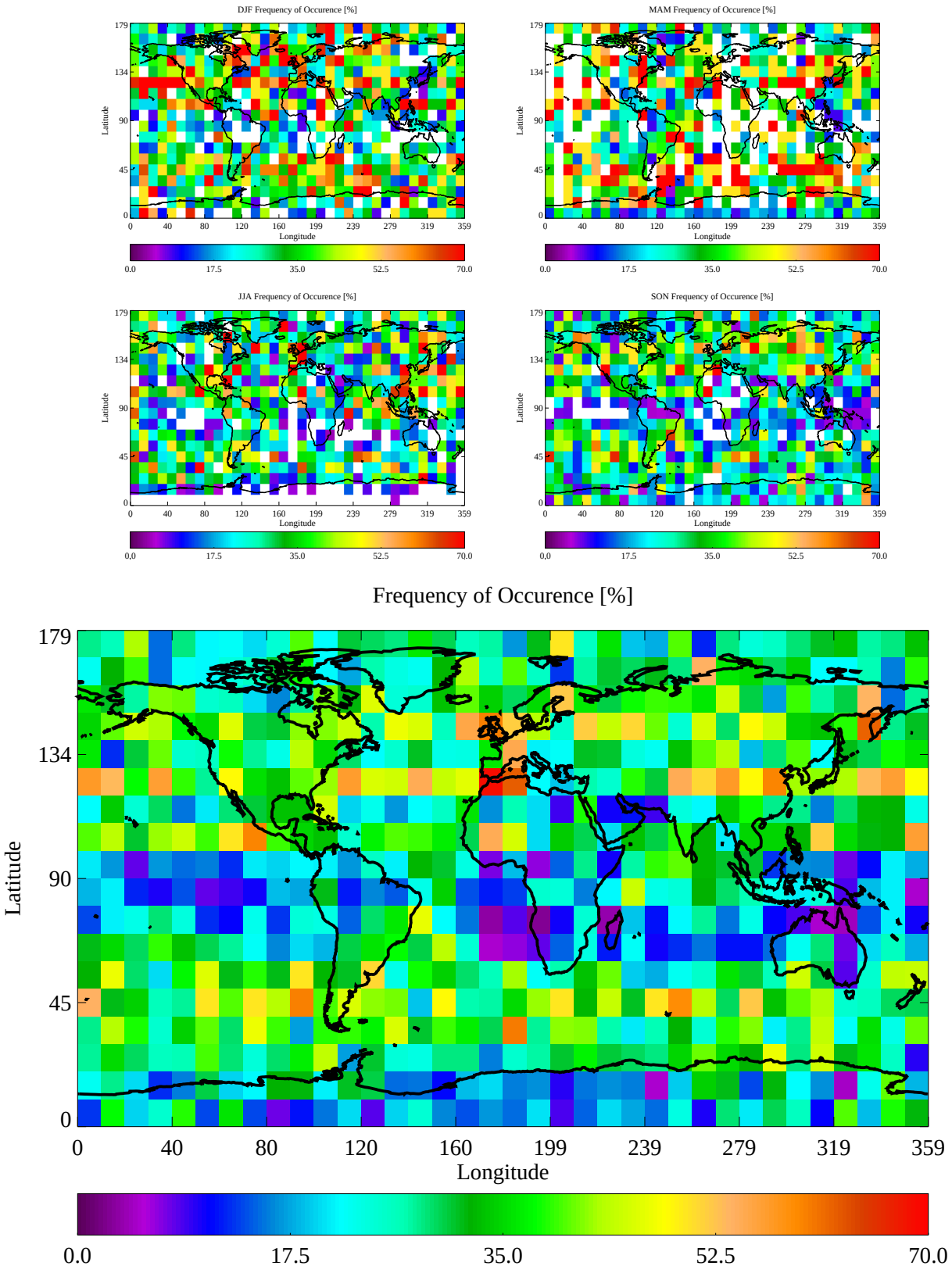

Figure 7.6: Mean cloud frequency of occurrence for each of the four seasons, given by DJF (December, January, February), MAM (March, April, May), JJA (June, July, August) and SON (September, October, November) as well as the annual average.

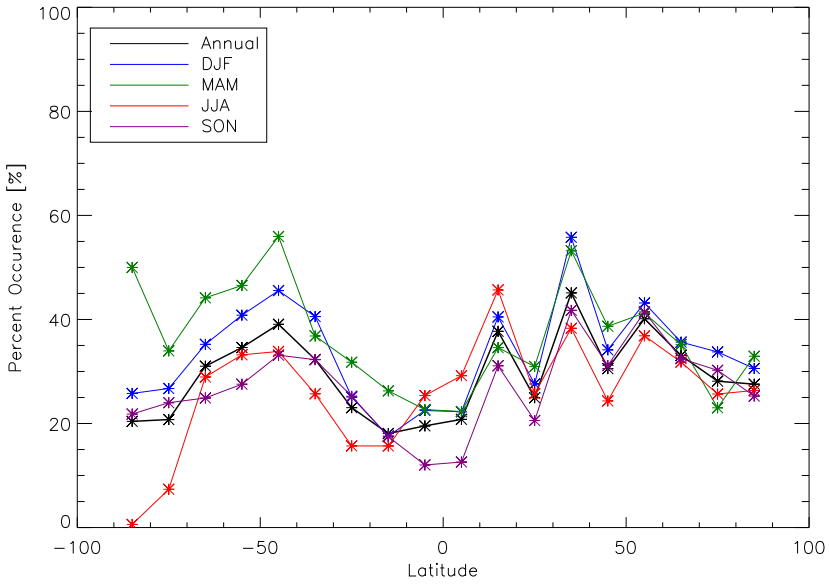

Figure 7.7: Mean cloud frequency of occurrence averaged zonally for each of the four seasons, given by DJF (December, January, February), MAM (March, April, May), JJA (June, July, August) and SON (September, October, November) as well as the annual average.

which act to increase their ability to hold water vapour and decreases the probability that clouds form – so these locations of frequency minima are to be expected in these regions of subsidence.

Finally, Fig. 7.8 shows the time series of the high level cloud frequency of occurrence for the year-long study period. Since cirrus has such a constant presence, from a first standpoint, it is expected that the mean cirrus cloud frequency of occurrence should be more or less constant over time at about 30%. While the frequency of occurrence found here does average around 30%, it is not truly constant over the year-long time frame. However, comparison with other studies of the same time period, the same relative shape in variation of frequency of occurrence with time is easily noted, as shown in Fig. 7.9

7.4 Relating Cloud Top Height and Frequency of Occurrence

It is interesting to consider how the mean high cloud top height and frequency of occurrence are related. Fig. 7.10 shows the relation between frequency of occurrence and cloud top height over the range of latitudes. It is clear that at each latitude, a certain cloud top height and frequency is dominant and this coupling of parameters varies from latitude to latitude.

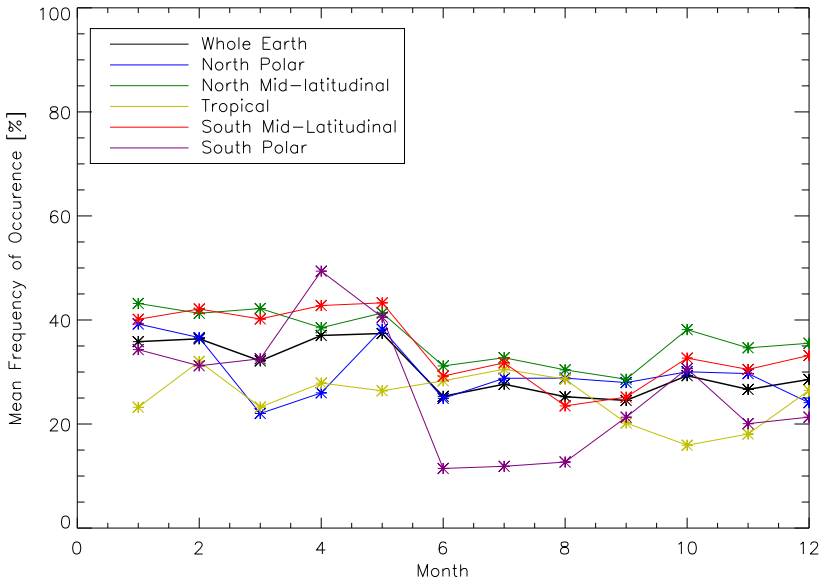

Figure 7.8: Time series of mean high cloud frequency of occurrence, given by latitude bins (north polar, north mid-latitudinal, tropics, south mid-latitudinal, south polar) and as a global average.

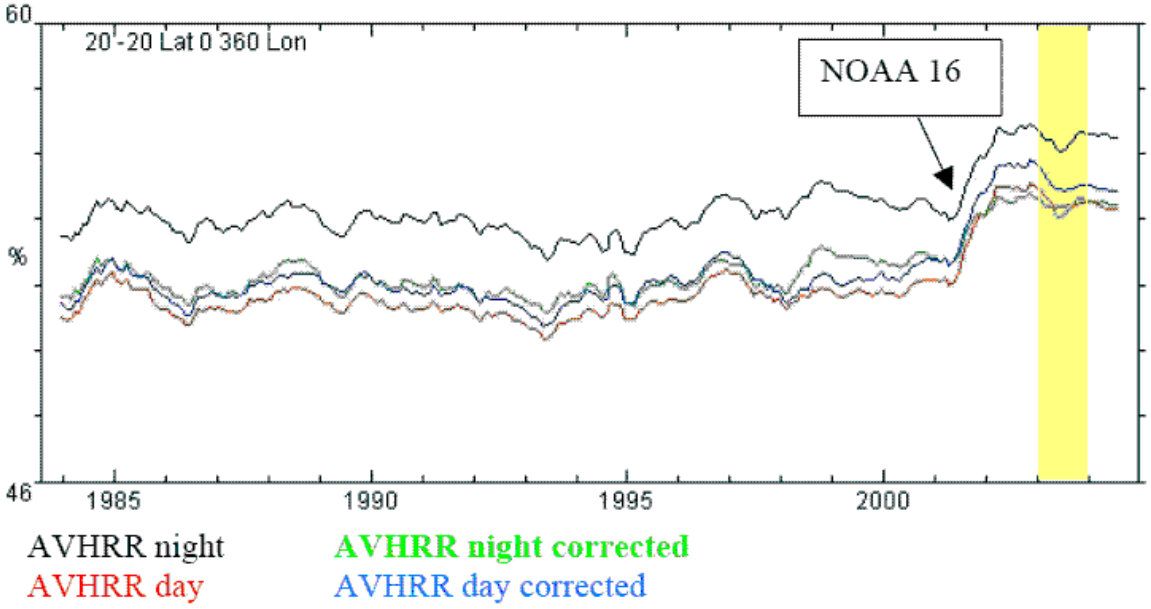

Figure 7.9: Time series of mean cloud frequency of occurrence from Campbell. The time period studied in this work is highlighted in yellow.

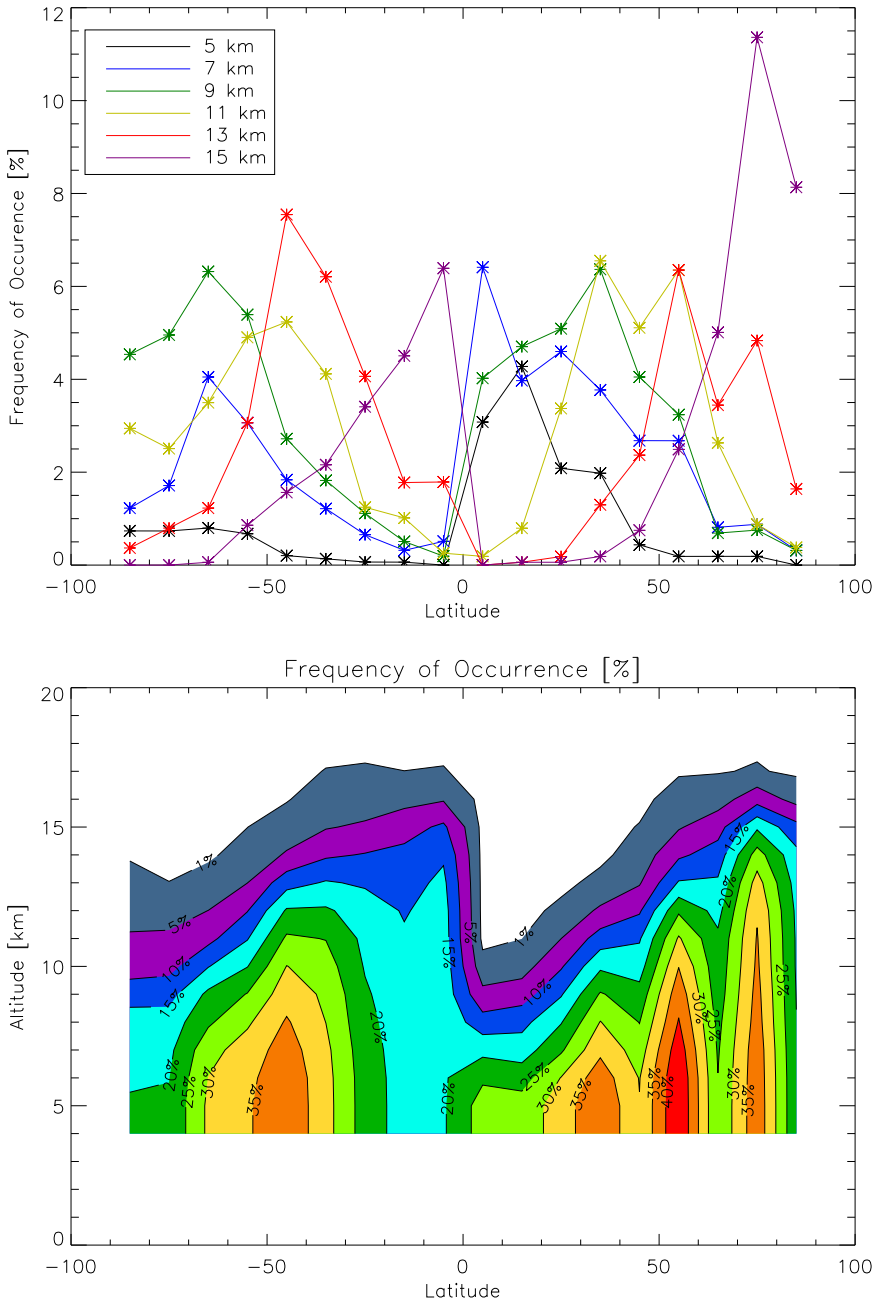

Figure 7.10: Frequency of Occurrence as a function of latitude and altitude. The top plot shows the latitudinal dependence of cloud tops at certain sample altitudes. The bottom plot shows the integrated frequency of occurrence at a given latitude and altitude, given that all points below the first cloud contaminated spectra are assumed cloudy.

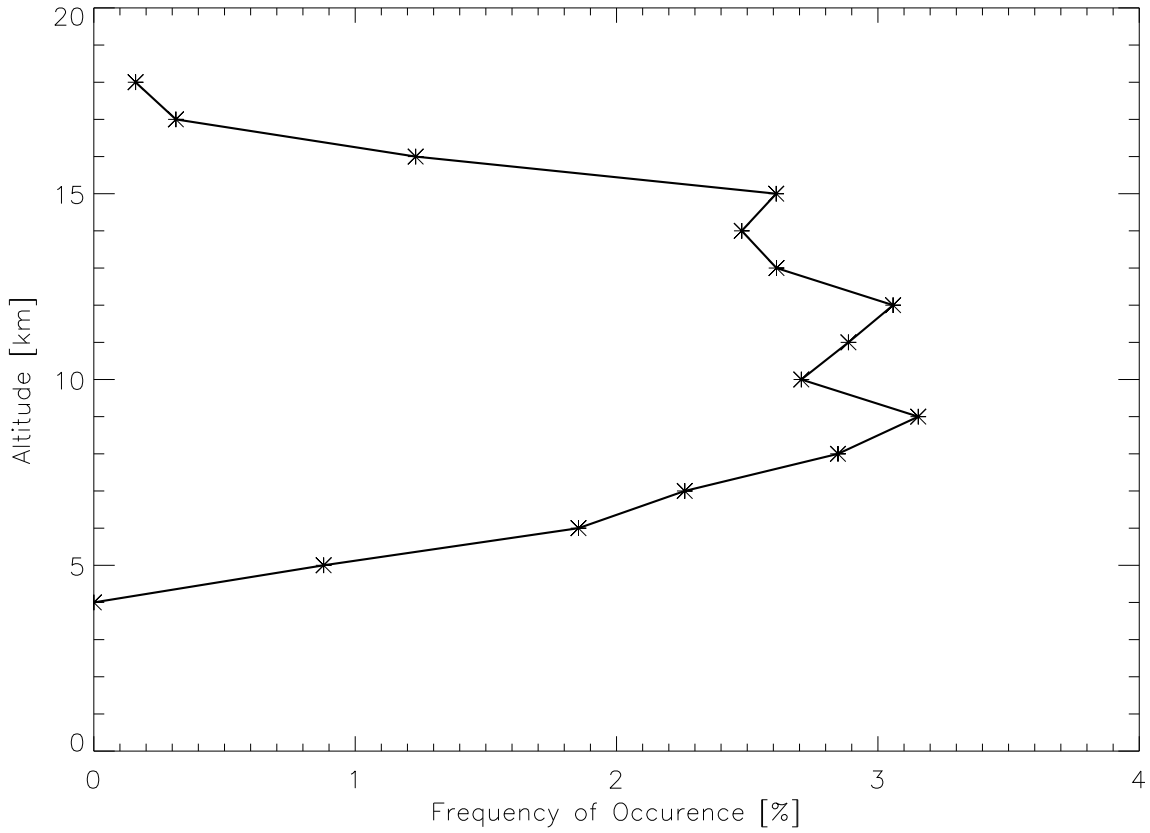

Figure 7.11: Frequency of Occurrence as a function of altitude.

Fig. 7.11 shows the relation between the globally-averaged cloud top height and the globally averaged frequency of occurrence for high clouds. It is comforting that the only clouds having cloud top heights within the range of about 5 km - 18 km have non-zero frequencies of occurrence. Furthermore, the tri-peaked structure of the relation can be attributed to dominant cloud top heights in certain latitudes, in consultation with Fig. 7.10. The lowest peak at 9 km can be attributed to high clouds occurring around $\pm 60°$ of latitude; the middle peak at approximately 12 km to those occurring around $\pm 40°$ of latitude; and finally the highest peak at about 15 km to high clouds at the equator.

7.5 Conclusions and Recommendations

The PACT Method has been successfully used to formulate a high level cloud climatology based on measurements from MIPAS over the time period of January through December 2003. The results compare qualitatively well with other such studies, in terms of estimated cloud top height and frequency of occurrence, such as ISCCP and HIRS. Several key features in retrieved cloud top height (Indonesian cloud peak, Andian cloud peak, equatorial cloud

peak) and in frequency of occurrence (Intertropical Convergence Zone shifting) have been identified and confirmed. As well, a detailed breakdown of latitudinal, altitudinal, and temporal dependence of the sought parameters (cloud top height and frequency of occurrence) has been presented.

Further work includes looking at several cases studies, nominally those highlighting the various formation mechanisms of cirrus, and comparison with other climatologies.

Chapter 8

Future Work and Time Plan

8.1 Timeline of Tasks Completed

During my first year at Oxford, I have completed several tasks, as outlined.

- **October 2005**: Background reading.
- **October 2005**: Review of spectroscopic database (produced technical note, cf. "Radiance Calculations Comparing version 3.1 and version 3.2 of the MIPAS Spectral Databases").
- **November 2005**: Attended Aura Science Meeting in Den Haag.
- **November 2005 – February 2006**: Analysis of D band as a candidate for cloud detection and of a cloud flagging anomaly (produced technical note, cf. "D Band Cloud Flagging Anomaly"). See Chapter 5 for further details.
- **February 2006**: Attended MIPAS Quality Working Group Meeting # 9 in Florence and presented "Analysis of D Band Cloud Flag".
- **February – May 2006**: Cloud top height retrieval, using some new methods. See Chapter 6 for details.
- **May 2006**: Attended ESA Atmospheric Science Conference in Frascati and presented a poster, "Cloud Top Height Retrieval from MIPAS".
- **May 2006**: Learned how to run Graham Ewen's McClouds Retrieval for cloud parameters.
- **June 2006**: Completion of Physics of Atmospheres and Oceans course.
- **May 2006 – present**: Producing a high level cloud climatology. See Chapter 7 for details.

8.2 Timeline of Projected Tasks

Over the next two years, there are three main areas that I would like to develop: my simple retrieval for cloud parameters (as of now, it retrieves only cloud top height), Ewen's McCloudsRT, and cirrus climatology studies. I foresee first comparing the results from both retrievals, improving both and then using these improved versions to do climatological work on cirrus clouds. Specifically:

- **Michaelmas Term 2006**:
  - Use McCloudsRT to retrieve properties (namely optical depth and cloud top height) to compare with high cloud climatology (see Chapter 7). Determine if the high clouds registered are cirrus.
  - Improve McCloudsRT calculations by re-running scattering property calculations so that the cost surfaces are smoother (because number density and effective radius surfaces will be smoother) - this may get rid of the local minima in which the McCloudsRT retrieval gets stuck. Use Bryan Baum's size distributions and log-normal distribution for number density.
- **Hilary Term 2007**:
  - Look at Kasprzyk's (2002) result that transmission is related to Colour Index such that, for constant a_i,
$$\tau = \frac{a_0 - a_1 CI}{a_2 - a_3 CI}. \tag{8.1}$$
  - Since the optical depth $\chi = \ln\tau$, this may be a good first guess of the cloud optical thickness. Add optical depth determined by CI Method into my simple retrieval of cloud top height to see if it gives an improved cloud top height result.
  - Do comparative study of several test cases to see if both McCloudsRT and my simple retrieval indicate that cirrus is present (using typical effective radius, number density and cloud top height values for McCloudsRT and optical depth, and typical cloud top height values for the simple retrieval. Use this to filter present high cloud climatology by ISCCP optical thickness criterion so that a cirrus climatology is produced.
- **Trinity Term 2007**:
  - Use the simple retrieval to estimate the brightness temperature from the cloud top height. Look at MIPAS level 1 spectra and difference the spectra with the Planck function evaluated at the cloud brightness temperature to see if the cloud (since the spectra will be dominated by the cloud signature) is net absorbing or emitting in the infrared, as represented schematically in Fig. 8.1.
  - Do this for a lot of cases. Do statistics to see how certain parameters and certain combinations of parameters (cloud top height, optical depth and geographic location) effect the net radiative state of the cirrus cloud.

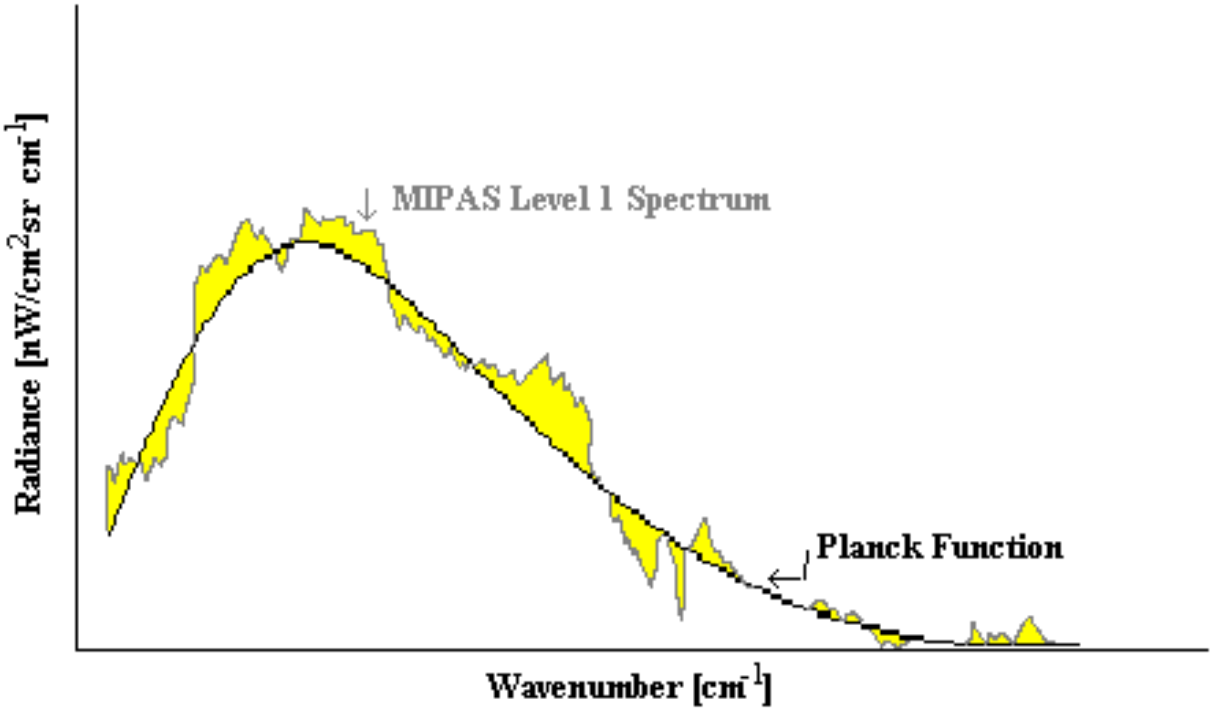

Figure 8.1: A simple differencing method to determine the net radiative state of cloud of interest.

- **Michaelmas Term 2007**:
  - Do grouping of parameter combinations that lead to a certain radiative state and run McCloudsRT on these to get a feel for more specific microphysical properties (namely effective radius and number density) that correspond to these characteristic states.
  - Start a more comprehensive cirrus climatology including cirrus cloud parameters (cloud top height, cloud depth, effective radius, number density, optical thickness) and the net radiative state of the cirrus cloud. Do this for two years of data (2003 and 2004) to reduce specific time-dependent synoptic conditions.
- **Hilary Term 2008**:
  - Finish cirrus climatology as discussed above.
  - Tie up loose ends ...
  - Start thesis write-up ...
- **Trinity Term 2008**:
  - Thesis write-up.

Bibliography

[1] Albrecht, B. A., "Clouds and Their Effect on Climate", *Enclyclopedia of Earth System Science*, **Vol.**(1), Academic Press Inc., 1992.

[2] Baran, A. J. and Francis, P. N.,"On the radiative properties of cirrus cloud at solar and thermal wavelengths: A test of model consistency using high-resolution airborne radiance measurements, *Quarterly Journal of the Royal Meterological Society*,**130**, pp.763-778, 2004.

[3] Campbell, G. Garrett, "Diurnal and Angular Variability of Cloud Detection: Consistency Between Polar and Geosynchronous ISCCP Products".

[4] DelGenio, A. D., "GCM simulations of cirrus for climate studies", pp.310-326, 2003.

[5] Dowling, D. R. and Radke, L. F., "A summary of the physical properties of cirrus clouds", *Journal of Applied Meteorology*, **29**, pp.970-978, 1990.

[6] Ewen, Graham B. L., "Infrared Limb Observations of Cloud", thesis submitted in partial fulfillment of DPhil Atmospheric, Oceanic and Planetary Physics, University of Oxford, Oxford, UK, 2005.

[7] Ewen, Graham B. L. et al., "Infrared radiative transfer modelling in a 3D scattering cloudy atmosphere: Application to limb sounding measurements of cirrus", *Journal of Quantitative Spectroscopic Radiative Transfer*, **96**, pp.45-74, 2005.

[8] Gordeau, J., "Clouds and particles: Characteristics of the different cloud types", Environmental Science Published for Everybody Round the Earth website: www.espere.net, (2004).

[9] Heymsfield, A. J. and McFarquhar, G. M.,"Mid-latitude and tropical cirrus: Microphysical properties", in D. K. Lynch, K. Sassen, D. O. Starr and G. Stephens (eds), *Cirrus*, Oxford University Press, New York, pp.78-101, 2002.

[10] Heymsfield, A. J. and Miloshevich, L. M.,"Homogeneous ice nucleation and supercooled liquid water in orographic wave clouds", *Journal of Atmospheric Science*, **50**: pp.2235-2353, 1993.

[11] Kasprzyk, Dominik, "Cloud Detection in MIPAS Spectra", thesis submitted in partial fulfillment of MPhys, University of Oxford, Oxford, UK, 2002.

[12] Lynch, D. K., "Cirrus clouds: Their role in climate and global change",*Acta Astronautica*, **38**, pp. 859-863, 1996.

[13] Menzel, W.P. and Prins, E.M., "Geostationary Satellite detection of biomass burning in South America", *Int. J. of Remote Sensing*, **13**, pp. 2783-2799, 1992.

[14] Minnus, Patrick and Harrison, Edwin F., "Diurnal Variability of Regional Cloud and Clear Sky Radiative Parameters Derived from GOES Data. Part II: November 1978 Cloud Distributions", *Journal of Applied Meteorology*,**Vol.**(23), **No.**(7), pp.1012-1031, 1984.

[15] Murtagh, F. and Heck, A., *Multivariate Data Analysis*, D. Reidel Publishing Company, Dordrecht, Holland, 1987.

[16] Reiter, E. R., "Stratospheric-Tropospheric exchange processes", *Review of Geophsics and Space Physics*, **13**, pp.459-474, 1975.

[17] Remedios, J.J. et al., "Reference Atmospheres and Cloud Indices", *presentation QWG#6,* (January 2005).

[18] Remedios, J.J. et al., "Reference Atmospheres and Cloud Indices", *presentation QWG#7,* (April 2005).

[19] Remedios, J.J. et al.,"Reference Atmospheres and Cloud Indices", *presentation QWG#8,* (September 2005).

[20] Rodgers, R. R. and Yau, M. K., *A Short Course in Cloud Physics*, **3**, Pergamon Press, Oxford UK, 1989.

[21] SAGE III ATBD Team,"SAGE III Algorithm Theoretical Basis Document (ATBD) Cloud Data Products", LaRC 475-00-106, Version 1.2, 26 March 2002.

[22] Spang, R. et al., "Colour Indices for the Detection and Differentiation of Cloud Types in Infra-red Limb Emission Spectra",*Advances in Space Research,* **33**, (2004).

[23] Woodbury, G. E. and McCormick, M. P., "Global Distributions of Cirrus Clouds Determined from SAGE Data", *Geophysical Research Letters*, **Vol.**(10), **No.**(12), pp.1180-1183, December 1983.

[24] World Meteorological Organization,*International Cloud Atlas, Manual on the Observations of Clouds and Other Meteors* **Vol.** (1), (1975).

[25] Wylie, Donald P. et al, "Four Years of Global Cirrus Cloud Statistics Using HIRS",*Journal of Climate*, **Vol.**(7), **No.**(12), pp. 1972-1986, 1994.

[26] Wylie, D.P., W. P. Menzel, H. M. Woolf, K. I. Strabala, "Four Years of Global Cirrus Cloud Statistics Using HIRS.", J. of Climate, 7, 1994.

[27] American Meteorological Society's Glossary of Meteorology: http://amsglossary.allenpress.com.

[28] Anu Dudhia, The Reference Forward Model (RFM): Software User's Manual (SUM): http://www-atm.physics.ox.ac.uk/RFM/sum.html.

[29] ESA ENVISAT website:
http://envisat.esa.int/instruments/images/MIPAS_Interferometer.gif

[30] EUMetSat website:
http://www.eumetsat.int.

[31] Carole J. Hahn website:
http://www.atmos.washington.edu/CloudMap/

[32] Hyperphysics website:
http://hyperphysics.phy-astr.gsu.edu/hbase/phyopt/michel.html#c2

[33] ISCCP website:
http://isccp.giss.nasa.gov/index.html

[34] S. Krueger website:
http://www.met.utah.edu/skrueger/6150/cloud_systems_lecture.pdf

[35] Leicester website:
http://www.leos.le.ac.uk/mipas/instrument/instrument.html#3

[36] MetEd website:
http://meted.ucar.edu/norlat/snow/micro_ice/1.1.crystal_growth.htm

[37] NASA HALOE website:
http://haloedata.larc.nasa.gov/about/images/occ.gif

[38] World Weather and Meteorological Data website:
http://xjubier.free.fr/en/site_pages/SolarEclipseWeather.html.